

This article is licensed under CC-BY 4.0 (cc) (†)



pubs.acs.org/CR

The Chemistry of Tetragonal FeS

David Rickard*



Cite This: https://doi.org/10.1021/acs.chemrev.5c00763

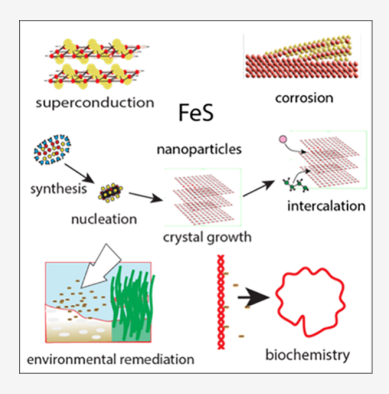


ACCESS I

Metrics & More

Article Recommendations

ABSTRACT: Research into tetragonal FeS_m, the synthetic equivalent of the mineral mackinawite, is currently at the frontiers of theoretical and applied chemistry. FeS_m is stoichiometric and crystallizes with a structure dominated by Fe-Fe layers. The familiar black, nanoparticulate precipitate develops from aqueous FeS clusters and displays varying initial compositions. Particle growth and crystallization are through oriented attachment of FeS nanoplates. Conflicting magnetic properties of FeS_m result from itinerant Fe d-electrons in the ground state displaying some localization experimentally. It is highly sensitive to the method of synthesis and this has led to widespread irreproducible, and often conflicting, results. At the same time this sensitivity offers the opportunity to synthesize FeS_m varieties with technologically valuable properties. FeS_m displays unconventional superconductivity $(T_c \sim 5 \text{K})$ derived from spatial anisotropy of electron pairs. Exotic compounds can be inserted in the vdW gap between the FeS layers giving rise to a spectrum of interlayered compounds. FeS_m can be highly efficient in sequestering a large array of environmentally deleterious inorganic and organic compounds including halogenated hydrocarbons.



However, FeS_m nanoparticles are genotoxic and this needs to be further investigated before they are widely distributed in the environment or used for medical purposes.

CONTENTS

I. Introduction	В
1.1. Historical Overview	В
2. Crystallographic Structure	C
3. Magnetic and Electrical Structure	D
3.1. Magnetic Ordering	D
3.2. Superconductivity	Е
4. Composition	F
4.1. Intercalation Compounds of FeS _m	G
4.2. Interlayered Sulfide-Hydroxide Materials	Н
4.2.1. Tochilinite-Group Compounds	Н
4.2.2. The Valleriites	- 1
4.3. Partially Oxidized Forms of FeS _m	I
5. Synthesis	J
5. Stability	L
6.1. Solubility of FeS _m	L
6.2. Surface Energy of FeS _m	М
6.3. Thermal Stability	0
6.4. Pressure Stability	Р
7. Kinetics and Mechanism of Formation of FeS _m	Р
7.1. Rate of Nucleation of FeS _m	Р
7.2. Mechanism of Formation of FeS _m from	
Aqueous Solution	Р
7.3. Mechanism of Formation of FeS _m from α -Iron	R
B. Particle Growth of FeS _m	R
8.1. Critical Radius of FeS _m Nuclei	R
8.2. Particle Size	S
8.3. Particle Growth	T
o.s. i article diowth	

9. Crystallization of FeS _m	U
9.1. Crystal Shape	Ü
9.2. Stacking Architectures	II.
9.2.1. Simple Stacking	Ü
9.2.2. Translational Stacking	V
9.2.3. Rotational Processes: Twistronics	V
10. Oxidation	W
	W
10.1. Oxidation by O ₂	
10.2. Mackinawite → Greigite	Х
10.3. Oxidation by Sulfur Compounds	Y
11. Surface Chemistry	Υ
11.1. Adsorption	Y Z Z
11.2. Element Sequestration	Z
11.3. Surface Reactions	AA
11.4. Reduction	AA
12. Organic Chemistry	AB
12.1. Reductive Dehalogenation	AB
12.2. Nonreductive Dehalogenation	AD
12.3. CO ₂ Reduction	AD
12.4. Free Radical Reactions	AD
12.5. Biological Chemistry	AE

Received: September 4, 2025 Revised: November 3, 2025 Accepted: November 5, 2025



13. Summary and Perspectives	AF
Author Information	AG
Corresponding Author	AG
Notes	AG
Biography	AG
Acknowledgments	AG
References	AG

1. INTRODUCTION

The iron sulfides are characterized by a number of polytypes and polymorphs (Table 1). Most of these occur naturally as

Table 1. End-Member Iron Sulfides, Their Abbreviations (abb), Structure and Mineral Equivalents

abb	structure	mineral
FeS_t	hexagonal	troilite
FeS_m	tetragonal	mackinawite
FeS_c	cubic	
$Fe_{(1-x)}S_{po}$	hexagonal	pyrrhotite
$Fe_{(1-x)}S_{po}$	monoclinic	pyrrhotite
$\mathrm{Fe_{0.82}S_{sm}}$	rhombohedral	smythite
Fe_3S_{4g}	cubic	greigite
FeS_{2p}	cubic	pyrite
FeS_{2ma}	orthorhombic	marcasite
$\begin{aligned} &\text{Fe}_{0.82} S_{\text{sm}} \\ &\text{Fe}_{3} S_{4g} \\ &\text{Fe} S_{2p} \end{aligned}$	rhombohedral cubic cubic	smythite greigite pyrite

minerals. Unfortunately, there is often little distinction made in the literature between minerals and their synthetic equivalents although these phases have different properties. Jon Jacob Berzelius wrote in 1815¹ that kemistens och den egentliga mineralogens åsikter av samma föremål ej endast KUNNA utan MÅSTE vara olika (the chemists' and true mineralogists' views of the same object not only CAN but MUST be different). In particular, the natural materials contain significant quantities of trace and minor elements other than Fe and S. This review is strictly limited to the chemistry of synthetic tetragonal ferrous monosulfide, which is referred to as FeS_m and sometimes, misleadingly, as synthetic mackinawite or even mackinawite. The chemistry of the mineral mackinawite has not been extensively reviewed although some aspects have been discussed in the mineralogical literature.²

There are three polymorphs of ferrous monosulfide: (1) tetragonal FeS_m occurring naturally as the mineral mackinawite, (2) hexagonal FeS_t which occurs naturally as the mineral troilite and (3) cubic FeS_c , the end-member of the (Zn,Fe)S sphalerite solid solution, which has not been identified naturally. In addition, there are a large number of variously nonstoichiometric forms which are classified naturally as the pyrrhotites, monoclinic and hexagonal iron sulfides with the general formula $Fe_{(1-x)}S$ (0.931 < x > 0.866). Confusingly, two other iron sulfide minerals have been referred to in the geochemical and soil science literature as "iron monosulfides". These include the iron thiospinel greigite (Fe_3S_{4g}) and smythite (rhombohedral $Fe_{0.82}S_{sm}$). The spectrum of pure phases in the FeS system is completed with the stable isometric disulfide, FeS_{2p} , pyrite, and its metastable orthorhombic polymorph FeS_{2ma} , known as the mineral marcasite.

In addition to these relatively well-defined phases, there exists a variety of nanoparticulate forms which grade into FeS clusters. These are generally transient and may be variously important as phases occurring during the formation of FeS_m . FeS clusters

form the active sites of important electron transfer proteins. However, this review focuses on the chemistry of solid FeS_m .

 ${\rm FeS_m}$ occurs naturally as the mineral mackinawite. Most recorded occurrences of mackinawite occur from late-stage reactions of the high temperature monosulfide solid solution and the mineral itself occurs as microscopic intergrowths in iron, copper, and nickel sulfides such as pyrrhotite, chalcopyrite (CuFeS₂), and pentlandite ((Fe,Ni)₀S₈).

Tetragonal FeS was identified as a corrosion product of steel oilwell pipes³ but the International Mineralogical Association (IMA) did not accept this as a mineral species. Likewise, Berner's original discovery⁴ of the material developing on iron trash in the Mystic River was not accepted as a natural occurrence by the IMA.

1.1. Historical Overview

Tetragonal FeS_m is familiar to chemists since it is major constituent of the black iron sulfide that precipitates at ambient temperatures through the reaction between dissolved iron and sulfide. The early 20th century history of iron sulfide chemistry has been summarized in comprehensive inorganic textbooks such as Mellor. This reveals that the state of the science was extremely confused in its early years. It is interesting to speculate whether future readers of this review will find the situation similarly confused and confusing. The problem at that time was the definition of the material and the uncertainty about which iron sulfide the researchers were describing. In the 1960s Cotton and Wilkinson⁶ revolutionized the approach to inorganic chemistry and iron sulfides had been relegated to just a few lines in their otherwise comprehensive text, possibly reflecting a waning chemical interest in these simple, binary covalent compounds.

Tetragonal FeS_m is a primary constituent of the group test protocol which was the basis of wet chemical inorganic analyses before the introduction of machine-based methods. Hydrogen sulfide had first been introduced into the classical scheme of cation groups for chemical analyses by Rose in 18297 and systematized by Fresenius in 1841.8 This remained the basis of most standard analytical chemistry courses through to the 1950s, whenVogel's classical textbook became the standard work. The analytical protocol separated elements which would precipitate as sulfides at an early stage in the process. The black iron sulfide that rapidly formed if the unknown compound contained Fe, was well-known to students taking qualitative analytic laboratories in chemistry since iron salts were relatively cheap materials. However, since the FeS_m precipitate is usually nanoparticulate, with limited long-distance crystal ordering, it was undefined crystallographically. In the absence of any techniques for further probing the nature of this material, there was little interest in the chemical literature. It was simply ferrous monosulfide with no defined structure.

Buchanan (1890)¹⁰ clearly distinguished between ferrous sulfide and pyrite and found FeS widely distributed in, especially, freshwater and estuarine sediments. Interestingly, it did not appear to occur to Buchanan that this was a discrete mineral phase. Siderenko (1901)¹¹ found ferrous sulfide in clays and called it *hydrotroilite*. The term *hydrotroilite* still finds its way into the literature. However, it has no validity since it is now known that FeS_m is anhydrous.¹² This material was shown to have a tetragonal structure by Berner (1962).⁴ Berner described the phase as *a component of hydrotroilite*. Berner used this delicate phrase to underline the fact that *hydrotroilite* is not a discrete mineral but a mixture of Fe sulfides, oxides and oxyhydroxides.

Indeed, Doss (1912)¹³ suggested that Sidorenko's *hydrotroilite* was a complex hydroxide.

The discovery of the mineral mackinawite was one of the early triumphs of the application of electron probe microanalysis (EPMA) to mineralogy. The problem with the identification of mackinawite microscopically was that its optical properties are similar to the mineral valleriite, (Fe²⁺,Cu)₄(Mg,Al)₃S₄(OH,O)₆. Indeed Ramdohr (1980),14 in his definitive work on ore microscopy, stated that mackinawite and valleriite were barely distinguishable. Birks et al. (1959)¹⁵ used an early EPMA instrument to show that apparent valleriite grains from the Mackinaw Mine, WA had a composition approaching FeS. Milton and Milton (1958)¹⁶ reported that this valleriite-like mineral was probably an undescribed iron sulfide. Mackinawite was discovered by Kuovo et al. (1963)¹⁷ in Outokumpo, Finland. Finally, it was named by Evans et al. (1964)¹⁸ from the type locality at the Mackinaw Mine, WA using EPMA to determine its composition and to establish that it was chemically distinct from valleriite.

The original contributions defining mackinawite and many of the other early reports of mackinawite were much concerned with the distinction of this mineral from the older, and apparently abundant, valleriite. These layered minerals are characterized optically by extreme pleochroism under reflected light depending on how the layers are aligned to the polarized light from the Nicol prism. Their color in their brightest orientation varies in shades of pale whiteish blue, pink and cream gray often dependent on the color of the enclosing phase.

The upshot was that in 1963, Kuovo, Vuorelainen, and Long were able to write the definitive paper 17 establishing mackinawite as a distinct mineral species. In fact, as they intimated, it has turned out that mackinawite is far more common than valleriite and most of the identifications of valleriite in the older literature turned out to be mackinawite. Indeed it has been argued that mackinawite was the last widely distributed simple mineral to be discovered on Earth.² Mackinawite was finally established as the mineral equivalent of a major constituent of the black FeS precipitate, long known to chemists, in 1964. 18

Much of the progress in understanding the chemistry of FeS_m has been related to advances in analytical methodology, particularly during the last 50 years. This has also led to some uncertainty in the reported properties of FeS_m since progress in instrument design has meant that older reports are often in conflict. For example, the development of the understanding of the composition of the mineral has been described as the EPMA instrument has been successively refined since it was first used to distinguish the mineral in 1964. Many instrument-based analytical methods have been used in the study of FeS_m (Table 2) since the material was originally shown to be nanoparticulate rather than amorphous. Advances in wet chemical methods of analyses of FeS_m are discussed in section 4.

2. CRYSTALLOGRAPHIC STRUCTURE

The ${\rm FeS_m}$ precipitate from aqueous solutions was originally described as amorphous since no well-defined XRD pattern could be obtained. ²⁰ It became apparent that this material was nanoparticulate and the small particle size was a major cause of the apparently amorphous XRPD patterns. ^{19–21} Even though truly amorphous FeS has not been defined, the phrase amorphous mackinawite, sometimes designated ${\rm FeS_{am}}$, continues to appear in the literature. ²²

Table 2. Instrument-Based Analytical Methods Used for Investigating the Properties of FeS_m

TEM	transmission electron microscopy
EDX	energy dispersive X-ray spectroscopy
XRPD	X-ray powder diffraction
XPS	X-ray photoelectron spectroscopy
XAS	X-ray absorption spectrocospy
XANES	X-ray absorption near edge structure
HRTEM	high resolution electron microscopy
Raman	Raman spectroscopy
LAXRPD	low angle X-ray powder diffraction
PDF	pair distribution function analysis
SAED	small area electron diffraction

The crystal structure of FeS_m is similar to that of the natural mineral mackinawite and the FeS corrosion product which was originally termed *kansite*. 3,4,18 The structure was refined by Lennie et al. in 1995²³ and this has remained the definitive structural designation. The FeS_m structure is tetragonal with the P4/nmm space group. The unit cell parameters are robust (Table 3). The widely accepted standard dimensions are $a = \frac{1}{2}$

Table 3. Experimental Unit Cell Dimensions (Å) for Standard FeS_m (Mackinawite) and 1σ Errors $(\pm (Å))^a$

a (Å)	c (Å)	ref
3.676 ± 0.002	5.032 ± 0.002	17
3.68	5.04	25
3.679 ± 0.002	5.047 ± 0.002	4
3.6795 ± 0.0008	5.030 ± 0.002	26
3.6735 ± 0.0001	5.0328 ± 0.0001	23
3.6647 ± 0.0013	4.9971 ± 0.0019	27
3.67	5.05	28
3.67	5.20	29
3.6574 ± 0.0007	5.2717 ± 0.011	30
3.6826 ± 0.0005	5.03440 ± 0.00009	31
The widely accepted dime	ensions are bold.	

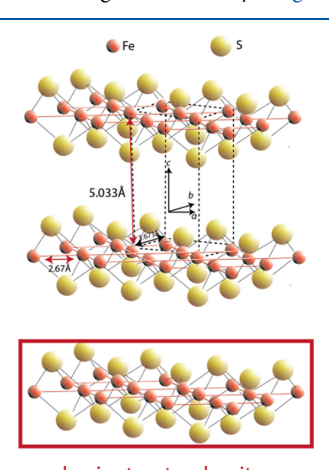
3.673 Å, c = 5.033 Å, with a cell volume of 67.91 Å³. The unit cell dimensions vary with age of the precipitate and the presence of intercalated exotic compounds (see section 9) and these variations have potential significance in the synthesis of superconduction in FeS_m. HRTEM measurements of d-spacings from lattice fringes are less precise than XRD measurements and vary with the method used for the computer-profile analysis: averaging the number of fringes within a specific area in multiple locations in the material gives lower d-spacings than line profile computations (e.g., 0.49 nm versus 0.52 nm).²⁴

The measured density of FeS_m is unknown. Most published values are given as the calculated density, ρ_{calc} (equation 1).

$$\rho_{\rm calc} = ZM_{\rm w}/V_{\rm c}N_{\rm A} \tag{1}$$

Here Z is the number of FeS moieties in a unit cell, $M_{\rm w}$ is the molecular weight, $V_{\rm c}$ is the unit cell volume and $N_{\rm A}$ is Avogadro's number. There is some uncertainty in published values of $\rho_{\rm calc}$ because the mackinawite composition has often been wrongly represented (see section 4), which has led to an uncertainty in $M_{\rm w}$ in equation 1. Using the standard formulation for FeS_m^{2,12} the formula weight is 87.91g mol⁻¹. The number of FeS moieties per unit cell, Z, is 2, the unit cell volume $V_{\rm c}$ is 67.91 ų, and Avogadro's number $N_{\rm A}=6.022\times10^{23}~{\rm mol}^{-1}$; therefore, the calculated density $\rho_{\rm calc}=4.3~{\rm g.~cm}^{-3}$.

There have been many representations of the mackinawite structure since its original discovery. Figure 1 shows a



basic structural unit

Figure 1. Ball and stick rendering of the crystal structure of FeS_m. The unit cell is shown by dashed lines. The distance between superjacent Fe layers is approximately 5 Å and the interlayer S–S distance is 3.58 Å. The basic structural unit is outlined. Adapted with permission from ref 32. Copyright 2024 Elsevier.

conventional ball-and-stick rendering from 30° above the (001) plane. The basic structural unit (Figure 1) is a square planar array of Fe atoms (Fe–Fe distance 2.597 Å) with tetrahedrally coordinated S atoms (Fe–S distance 2.256 Å).

FeS_m belongs to a group of materials with layered structures which are commonly (and mistakenly³³) referred to as 2D layered materials. They are characterized by a van de Waals (vdW) gap along their stacking directions.³⁴ The vdW forces between the S atoms hold the FeS layers together. This arrangement means that the crystallographic structure of the material varies during particle growth and the development of long-range ordering in the material with time. Additionally, the structure can be modified synthetically by the intercalation of exotic compounds into the interlayer spaces. This process is of interest in the syntheses of superconducting varieties of the material (section 5).

Deconvolution of low angle XRPD spectra of precipitated FeS revealed a second phase, referred to as MkA, with characteristics distinct from FeS_m. ²¹ This phase was originally reported to have a particle size of 2.2 nm \times 1.7 nm and lattice parameters a=b=4.0 Å, c=6.6 Å. It converted to more conventional FeS_m with a=b=3.7 Å, c=5.5 Å within a few hours at room temperature in aqueous solutions. These observations have been revisited and interlayer spacings $a=b\leq 4.0$ Å and $c\leq 6.6$ Å 19,21,29,30,35,36 have been reported for the initial phase. It was subsequently identified in conventional XRPD spectra 30 (Figure 2). In the charged-layers model 30 FeS_m nanoparticles are divided

In the charged-layers model³⁰ FeS_m nanoparticles are divided into two groups: FeS_m with negatively charged layers and FeS_m without charged layers. The charged FeS_m variety appears to map onto the poorly ordered phase with larger intralayer spacings. It is suggested that the negative charge arises through Fe vacancies in the Fe-Fe layer.³⁰ Alternatively, this phase may be similar to the initial FeS nanoparticles which aggregate to form larger FeS_m crystals, described in section 8. In that interpretation, misalignment of stacked nanoplates causes d_{001} to increase (see section 9.2.2).

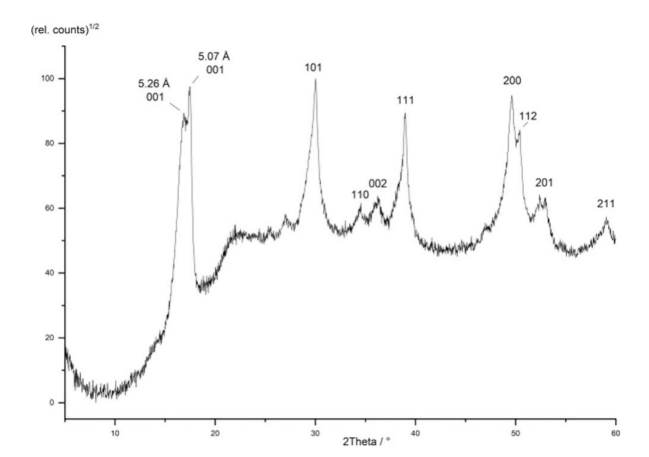


Figure 2. XRPD pattern of FeS_m precipitate showing the split in the 001 peak and an assignment to different FeS phases with different interlayer spaces Reproduced from with permission from ref 30. Copyright 2021 Royal Society of Chemistry.

The variation in ${\rm FeS_m}$ structures with time have potentially important practical consequences. In particular, the product of the reaction between an iron salt and sulfide is commonly identified solely on the basis of XRPD data. The variations of these data have led to the mistaken interpretation of the XRPD spectra as mixtures of tetrahedral ${\rm FeS_m}$ and isometric ${\rm Fe}_3{\rm S}_{4g}^{37}$ It is possible that the reported prevalence of ${\rm Fe}_3{\rm S}_{4g}$ in the reaction products has been overestimated. Certainly, it appears that independent data, such as compositional, magnetic or grain-specific SAED data, are required for more accurate estimations of the prevalence of ${\rm Fe}_3{\rm S}_{4g}$ in FeS reaction products.

3. MAGNETIC AND ELECTRICAL STRUCTURE

3.1. Magnetic Ordering

The crystallographic structure of FeS_m is dominated by layers of Fe atoms arranged in a square lattice (i.e., substructure) with Fe–Fe distances of 2.60Å similar to that of α -Fe (2.485 Å). The adjacent $d_{x^2-y^2}$ orbitals overlap and their energy is lowered compared with nonbonding d_{z^2} orbitals. The material has thus been conventionally considered to be metallic with highly delocalized Fe 3d electrons, ^{38–40} and there is some experimental evidence to support this conclusion in bulk FeS_m .⁴¹ other conductivity measurements revealed semiconductor-like behavior⁴² although the material was shown to be intrinsically metallic. 43 These authors suggested that the reason the metallic character was not seen below 300 K at 0.1 GPa pressure is due to weak localization: this conclusion is supported by the observation that the metallic-nonmetallic transition decreases to 75 K at 3 GPa. The material has long been known to show extreme anisotropy in its electrical and magnetic properties⁴⁴ with the Fe-Fe layer being metallic in character as described in section 2. However, the experimentally derived properties of the material have been controversial because of problems with crystal size, synthesis of pure FeS_m and changes during sample handling.³¹ The synthesis of large FeS_m crystals (see section 5) has enabled many of these problems to be overcome and some consistency between the computed and experimentally derived properties to be obtained.31

It is convenient to distinguish element oxidation numbers from specific ions. Specific ions are designated by a right upper index, such as A^{2+} or A^{2-} . In aqueous solutions, this is often, in

itself, an abbreviated form for hydrated species and coordinated H_2O molecules are conventionally not included in the formulation (e.g., the hexaqua ferrous ion, $\mathrm{Fe}(H_2O)_6^{2+}$). In this representation oxidation numbers are indicated by Roman numerals (e.g., $A(\mathrm{II})$ in text or A^{II} in formulas).

Fe(II) in the mackinawite structure is locally tetrahedrally coordinated to four equidistant sulfur atoms. Conventional ligand field theory would then suggest that the Fe(II) is in a high spin state.²⁰ The first Mössbauer spectrum of FeS_m was published within 10 years⁴⁵ of Rudolph Mössbauer first describing the eponymous effect. The results showed a complex structure which was suggested to be due to a mixture of phases. The problem of phase mixtures in FeS samples has continued to stalk the Mössbauer community. The Mössbauer spectrum varies with different preparation protocols as well as the temperature at which the spectra were collected. 46 The variation in sample preparation protocols results in different admixtures of phases in the sample, particularly varying amounts of γ -FeOOH (synthetic lepidocrocite) and Fe_3S_{4g} (synthetic greigite). Single phase FeS_m shows spectral singlets corresponding to Fe²⁺ ions. The reported isomer shifts for these singlets vary with temperature (Table 4). Reported additional signals in the spectrum correspond to Fe^{III} either due to the development of cryptic Fe₃S_{4g} or as the presence of discrete iron oxyhydroxide phases. ²⁸, ³⁰, ⁴⁶, ⁴⁷

Table 4. Reported Isomer Shift δ (mms⁻¹) Reported for Different Temperatures (T (K)) for FeS_m

T (K)	$\delta~({\rm mm~s^{-1}})$	ref	date collected
1.7	0.44	Bertaut et al. ⁴⁸	1965
4	0.49	Schroeder et al.46	2020
	0.2	Vaughan and Ridout ⁴⁴	1971
80	0.47	Bolney et al. ³⁰	2021
292	0.37	Bolney et al. ³⁰	2021
293	0.37	Schroeder et al.46	2020
295	0.42	Boursiqout et al. ⁴⁷	2001
	0.4	Mullet et al. ²⁸	2002

There is a discordance between the theoretical conventional view of the spin state of Fe(II) in FeS_m and experimental observation. Fe^{II} in FeS_m is a tetrahedrally coordinated d^6 ion with two possible electron configurations (Figure 3). Conven-

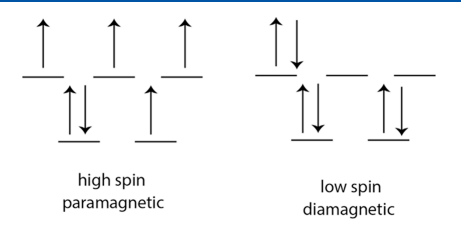


Figure 3. High spin and low spin electron configurations of Fe(II) in tetrahedral coordination in $FeS_{\rm m}$.

tionally, Fe^{II} in FeS_m is regarded as high $spin^{20}$ and thus the material should be paramagnetic. However, the Mössbauer spectrum of FeS_m shows a single line spectrum over the whole temperature range from 1.7 to 295 K.⁴⁸ This persists during the application of an external magnetic field and is reported from the Mössbauer spectra of defined nanoparticles.²⁸ Several DFT optimizations of FeS_m have been published with increasing degrees of sophistication. Earlier results were often conflicting,

concluding that the ground state of the material was non-magnetic ³⁹ or that it displayed a substantial magnetic moment on its Fe^{II} atoms. ⁴⁰ Further DFT computations suggested that the reason for the discordance in the models was that the Fe^{II} displayed strong itinerant spin fluctuations. ⁴⁹ This result has been supported by observations with photoemission spectroscopy which revealed a magnetic moment on the Fe ions. ⁴⁹ X-ray adsorption spectroscopy (XAS) indicates delocalized 3d electrons similar to Fe metal. ⁴⁹ The ground state is magnetic but these spin fluctuations suppress this magnetism and the Mössbauer spectrum shows only the low spin singlet.

This conclusion is consistent with the now classical theory of the dual characteristics of the d-electrons responsible for magnetism in Fe:⁵⁰ they are itinerant electrons described by band theory in the ground state while experimentally they display properties associated with localization.

3.2. Superconductivity

Superconductivity is defined as perfect electrical conductance (i.e., zero resistance) and complete expulsion of magnetic field lines from the interior of a material. This transition occurs when the material is cooled below a critical temperature ($T_{\rm c}$). The report of superconductivity in a cheap material like FeS_m⁵² has led to a flurry of interest in its electromagnetic properties. $^{53,54,31,55-58}$ The holy grail in this area is, of course, high temperature superconductivity which is generally defined as superconductivity above 77 K the boiling point of liquid N₂.

Superconductivity develops where electron pairs move in unison in the material and consequentially experience no resistance: then electricity is conducted with no resistive loss of energy. The original Bardeen-Cooper-Schrieffer (BCS)⁵⁹ explanation was that electron pair formation is mediated by phonons, quasiparticles arising from the mechanical quantization of ionic vibrations in the material: the sonic equivalents of photons. FeS_m, however, belongs to a class of unconventional superconductors where their superconductivity does not derive from electron-phonon coupling. Instead, the electron pairs appear to form as a consequence of spatial anisotropy of their relative motion which generates an attractive coupling. Isostructural FeSe displays a superconducting transition temperature of up to 65 K if prepared as a single layer film on a $SrTiO_3$ substrate.⁶¹ It has been suggested that this high T_c is reached through differential electron-phonon coupling with the oxygen atoms in the SrTiO₃ substrate, 62 which brings us, moreor-less, back to the original BCS theory.

Muon spin rotation (μ SR) studies of FeS_m show that, by contrast with magnetic properties, its superconducting behavior is largely insensitive to the presence of small concentrations of nonsuperconducting magnetic phases, possibly including Fe₃S_{4g} in the material. These results are consistent with further μ SR measurements which showed that low-moment magnetism and bulk superconductivity coexists in FeS_m. In view of the facile development of Fe₃S_{4g} in FeS_m, together with its sensitivity to oxidation, this suggests that manufacturing FeS_m-based superconductors might be easier than earlier expected.

A major problem in understanding superconductivity in FeS_m has been the synthesis of the material. Conflicting reports on the electrical and magnetic properties of FeS_m appear to be at least partly due to variations in the nature of the synthesized material (see section 5).

Table 5. Fe and S Contents (wt %) for FeS Phases (Listed in Terms of Fe:S Atoms Per Formula Unit (apfu) Ratios) and the Differences (Δ Fe and Δ S wt %) between These and Fe_{1.0}S

Fe:S apfu ratios	Fe wt %	ΔFe wt %	S wt %	ΔS wt %	structure	mineral
Fe _{1.1} S	65.707	-2.182	34.293	-2.179	?	?
$Fe_{1.0}S$	63.525		36.475		tetragonal	mackinawite
Fe _{0.931} S	61.857	1.668	38.143	1.672	hexagonal	pyrrhotite
Fe _{0.866} S	60.135	3.390	39.864	3.394	trigonal	pyrrhotite
$Fe_{0.82}S$	58.820	4.705	41.180	4.709	monoclinic	smythite
Fe _{0.75} S	56.64	6.885	43.36	6.886	cubic	greigite
Fe _{0.5} S	46.551	16.977	53.449	16.977	cubic/orthorhombic	pyrite/marcasite

4. COMPOSITION

The composition of tetragonal FeS has been surprisingly difficult to pin down. Major uncertainties surrounded the iron-rich nonstoichiometric formulation, Fe_{1+x}S, which became popular in the last century 4,65,66 because it appeared to distinguish mackinawite from the iron-deficient pyrrhotites, Fe_{1-x}S, and troilite, hexagonal FeS_t. Reports of iron-deficient FeS_m 67 were largely ignored.

The analysis of a simple binary material such as FeS_m should be easily accomplished since it can be synthesized in bulk and multiple samples taken. The primary problem has been the precision of the analyses (Table 5). Stoichiometric $Fe_{1.0}S$ contains 63.525 wt% Fe and 36.475 wt% S. Obviously, because the ratio of the atomic masses of Fe and S is 1.792, the relationship between atoms per formula unit and wt% is nonlinear. Then $Fe_{1.1}S$ contains 65.707 wt% Fe and 34.293 wt% S so that to distinguish between $Fe_{1.0}S$ and $Fe_{1.1}S$, an analytical precision of better than 2.2 wt% Fe and S is required. Likewise, $Fe_{0.9}S$ contains 61.055 wt% Fe and 38.945 wt% S, an analytical difference of better than 2.2 wt% Fe and S from stoichiometric FeS. By comparison, Fe_3S_{4g} , with which it is commonly associated, has 56.64 wt%S Fe and 43.36 wt% S requiring an analytical precision of better than 7 wt%.

The main reason for the analytical imprecision in published reports of ${\rm FeS_m}$ stoichiometry is systematic errors in the S analyses. 12 For example, dissolving ${\rm FeS_m}$ in acid results in the formation of ${\rm S}^{012}$ which is lost to the total, resulting in a Fe excess in the resulting stoichiometry. Of course, this can be checked if analytical totals are reported, but this has not always been the case. For example, only 81 ± 3 wt% of the total ${\rm FeS_m}$ precipitate is recovered in hot 6 M HCl digestions and 104 ± 14 wt% in cold 6 M HCl digestions over 1 h. 68,69 The effect of these systematic errors on the received Fe:S ratios is quite dramatic: a loss of 10 wt% of the S content, for example, would result in ${\rm Fe}_{1.11}{\rm S}$ for FeS and ${\rm Fe}_{1.03}{\rm S}$ for ${\rm Fe}_{0.93}{\rm S}$.

Examples of the reported compositions of synthetic FeS_m are listed in Table 6. The compositions are listed simply in terms of their atomic Fe:S ratios and the date of publication is also noted. The range of reported Fe:S ratios is revealing.

In wet chemical analyses of bulk $\mathrm{FeS_m}$ precipitates, the initial acid dissolution stage in the protocol results in the formation of various amounts of elemental sulfur. The result is that the extracted solution is variously sulfur-deficient, leading to a small but often persistent excess of iron in the analysis. This problem can be overcome by including a reducing agent, such as $\mathrm{Ti}(\mathrm{III})$ citrate, in the digestion. The result is that synthetic $\mathrm{FeS_m}$ has a composition of $\mathrm{Fe_{1.00\pm0.01}S.}^{12}$ This has been confirmed independently using a different analytical method involving the oxidation of sulfide to sulfate.

The second problem in many reported analyses has been the accuracy. The problem here has been the poorly defined nature

Table 6. Examples of the Reported Stoichiometries of FeS_m by Wet Chemical Analyses

formulation	year	source
	,	
Fe _{1.05} S	1964	3,60
Fe _{0.91} S	1968	61
$Fe_{1.04}S$	1997	62
Fe _{0.94} S	1973	55
Fe _{1.00} S	2006	13
Fe _{0.79} S	2010	63
$Fe_{0.72}S$	2018	64
$Fe_{1.01}S$	2021	23

of the precipitate being analyzed. For example, the Fe:S ratio for the thiospinel greigite, Fe₃S_{4g}, is 0.75 which is similar to that of some of the reported ratios of apparent FeS_m listed in Table 6. XRPD is commonly used to define the product, but this is a relatively weak constraint on the nature of the material. FeS_m precipitates often contain cryptic oxidation products such as Fe_3S_{4g} and Fe oxyhydroxides (section 10) which may not show up on conventional XRPD scans. Even well crystalline exotic material in concentrations of less than 10 wt % may be difficult to detect. Washing the precipitates is also necessary since they can contain compounds derived from the solution such as water, sulfate, chloride or sulfide either in discrete phases or as absorbates depending on the reactants used in the synthesis. Splitting the samples into two, one for Fe analysis and one for S analysis also contributes to the inaccuracy of the analyses. Ideally, both Fe and S analyses should be made on the same sample and the totals reported.

There has been an apparent dichotomy between the composition of synthetic FeS $_{\rm m}$, which is often mistakenly assumed to be equivalent to the FeS in sediments, and that of the mineral mackinawite, which is a widespread constituent of sulfide ores and meteorites. This apparent dichotomy has been resolved by correcting systematic errors in the analytical protocols for FeS $_{\rm m}$ and statistical analyses of the compositions of natural mackinawite. The results demonstrate that FeS $_{\rm m}$ and mackinawite are pure phases in the Fe-S system with stoichiometric Fe $_{1.0}$ S compositions. The result confirms the conclusions from the original structural refinement (see section 2). This contrasts with information provided in most mineralogical databases that wrongly describes the mineral mackinawite as an iron nickel sulfide and chemical accounts that refer to the composition of FeS $_{\rm m}$ as Fe $_{1+x}$ S. The results of the composition of FeS $_{\rm m}$ as Fe $_{1+x}$ S.

This review concerns the chemistry of synthetic tetragonal ${\rm FeS_m}$ and not the mineral mackinawite. This caveat is appropriate here because mackinawite composition, like most minerals, is characterized by the inclusion of minor elements in the structure, including Ni, Co, and Cu leading to subspecies such as nickelian $(0.1 > {\rm Ni} < 22.7 {\rm ~wt~} \%, \le 0.4 {\rm ~apfu})$, cobaltian

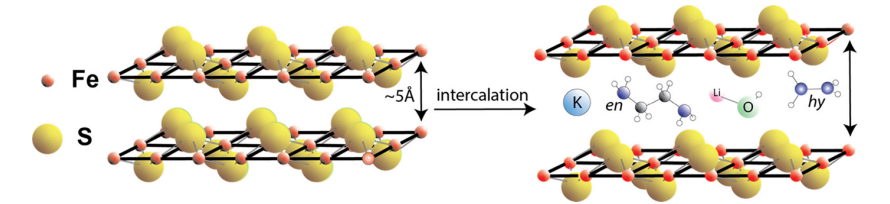


Figure 4. Intercalation of exotic compounds into FeS_m . Illustrated intercalations include potassium (K), ethylenediamine (en), Li hydroxide, and hydrazine (hy).

(0.1> Co < 12.9 wt %, \leq 0.2 apfu), and cupriferous mackinawites (0.1 > Cu < 4.7 wt %, \leq 0.1 apfu). In addition, less robust accounts of Cr (\leq 9 wt %?) and Ag (\leq 7.1 wt %?) have been reported. Statistical analyses of the data show that Co and Ni substitute for Fe in the mackinawite structure, rather than being trapped between the FeS layers. 2

A number of other elements have been reported as being associated chemically with mackinawite, or at least with the H₂S produced by acid treatment of sediments which may evidence the presence of iron monosulfide. This has led to extensive experimentation with various forms of nanoparticulate FeS which has shown that many elements, including deleterious elements like As, can be removed from solution by a variety of processes involving FeS including surface redox reactions (Cr, Se, U), adsorption (Mn, As, U), and coprecipitation (Mn, Co, Ni, Cu, Zn, As, Tc, Cd, Re, Hg, Pb). These are discussed in some detail in section 11.1. However, there is little evidence that these elements are significant in the structure of mackinawite minerals.

 ${\rm FeS_m}$ does not contain structural ${\rm H_2O}$. The suggestion that the precipitate might be a hydrate $({\rm FeS\cdot nH_2O})^{71}$ echoed earlier ideas about the discredited mineral *hydrotroilite.*⁷² ${\rm H_2O}$ is present in wet ${\rm FeS_m}$ synthesized in aqueous systems both as intraparticle water and as water adsorbed on the ${\rm FeS_m}$ surface, but both forms of water are removed by freeze-drying and structural water does not occur. 12,30 In fact, ${\rm FeS_m}$ formation from aqueous FeS clusters is entropy driven and involves the expulsion of water molecules. 73 The removal of interparticle and surface water from ${\rm FeS_m}$ nanoparticles facilitates nanoparticle aggregation and the formation of larger domains of coherent scattering. 35

Advances in energy dispersive X-ray analysis (EDX) have enabled Fe:S ratios of synthetic nanoparticulate iron sulfides to be probed. Most reports merely list Fe:S ratios and do not include total analyses. The problems here have been discussed with respect to EPMA, 2 but these refer equally (or are even more apparent) with other electron beam methods such as EDX. They mostly refer to problems with the date at which analyses were performed and what was the contemporary instrument. Electron beam methods have improved considerably in the last 50 years and earlier analyses may be less precise than more recent ones. Data treatment has also improved, although this may be a minefield since many of the instruments have in-built programs that automatically correct the analytical total to 100 wt %. There is also a problem with the standards routinely used: pyrite, FeS₂, is a common standard and this has considerable compositional divergences from FeS_{m} as well as potential uncertainties in its composition. The analytical uncertainties are usually around 0.1 apfu on the S/Fe ratio in EDX analyses even with relatively pure synthetic pyrite crystals.

The second source of analytical uncertainty refers to the accuracy of the analyses and this particularly concerns the nature

of the sample being analyzed: how pure is the FeS_m sample? For example, variations in the composition of FeS_m readily arise through (1) cryptic oxidation of Fe^{II} \rightarrow Fe^{III} and S^{-II} \rightarrow S_n^{-II} and the FeS_m surface is often covered with an oxidized layer, ²⁸ and (2) inclusion of minor elements in the structure. These variations in stoichiometry may be important in developing superconductivity in the material and the fine-tuning of the composition of FeS_m is a current research goal.

The charged-layers model described in section 2 describes charged FeS_m phases with the net charge arising through vacancies in the Fe–Fe layer. The implication is that the composition of these early charged phases is nonstoichiometric $Fe_{1-x}S$, although chemical analyses are currently insufficiently precise to define these. The properties authors, the charge balance in the nonstoichiometric particles may be made up by the adsorption of Fe^{2+} or solution cations, such as Na^+ .

4.1. Intercalation Compounds of FeS_m

The possibility of inserting exotic compounds within the vdW gap in FeS_m has long been of interest. Originally water was thought to occur in the $\text{gap}^{21,30,75}$ and cause expansion of the structure of the initial precipitated material. However, drying does not cause any change in the interlayer spacing 30 and FeS_m does not contain structural water. 12

FeSe, the selenium homologue of FeS $_m$, was first discovered to be a promising superconductor. The later finding that FeS $_m$ also had superconducting properties led to an upsurge in interest in the possibilities of intercalated FeS $_m$ compounds. These are defined here as layered compounds in which the integrity of the FeS $_m$ layer, with its square planar Fe—Fe substructure, is maintained (Figure 4).

A variety of exotic compounds can be inserted into the interlayer spaces in FeS_m including potassium, ethylenediamine, iron ethylenediamine complexes, 79,83,84 hydrazine, and lithium hydroxide (Table 7). The compositions listed from the original sources in Table 7 are atomic ratios and total analyses are not reported. The structural effect of the intercalations is to (1) increase the size of the c dimension of the FeS_m unit cell compared with \sim 5Å of the original FeS_m while maintaining the dimension of the a dimension; (2) create supercell architectures through organized Fe vacancies in the Fe–Fe layers.

The potassium-based intercalation compound has the nominal compositions $K_{0.8}Fe_{1.7}S_2$ and $K_{1.1}Fe_{1.6}S_2$ based on measurements of the element ratios. The interlayer spacing of $K_{0.8}Fe_{1.7}S_2$ is 6.72Å. The composition suggests that the Fe layer is nonstoichiometric, $Fe_{1-x}S$, and XRD analyses show an organized vacancy superstructure. Much of this is similar to the properties of the selenium homologue but $K_xFe_{(2-y)}Se_2$ crystals are superconductors whereas $K_{0.8}Fe_{1.7}S_2$ is a semiconductor. R1

Table 7. Examples of the Effect of Intercalated Compounds on the FeS_m Structure^a

intercalation	Fe:S	a (Å)	c (Å)	ref
standard FeS _m		3.76	5.03	23
0.4K	$Fe_{0.86}S$	3.75	13.57	77
$0.2(C_2H_8N_2)$	FeS	3.69	20.427	78
$[Fe(C_2H_8N_2)_3]_{0.06} \cdot (C_2H_8N_2)_{0.9}$	$Fe_{0.94}S^{b}$	3.70	20.51	79
$Li_{(1-x)}Fe_xOH$	FeS	3.70	8.89	80,81
$0.4N_2H_4$	FeS	3.7	17.5	82

 a The a and c dimensions of the tetragonal unit supercell are listed (Å) and compared with those of standard FeS_m. The Fe:S ratio of the FeS_m-type layers is listed, and the interlayer composition has been recalculated as a ratio of the intercalation to effectively one FeS molecule. ^bOrthorhombic, distorted tetragonal structure with b = 3.69

The reason for the change in electrical properties may be related to the changes in the occupancy of the Fe-Fe layer.

Ethylenediamine $(C_2H_4(NH_2)_2 \text{ or } en)$ is a simple chelating agent forming complexes like $[Fe(en)_3]^{2+}$. Intercalation of ethylenediamine with FeS_m leads to the formation of interlayers of mixtures of $[Fe(en)_3]^{2+}$ and en occupying the vdW gap in 2:1 and 2:3 ratios. 83 The intercalation of a charged complex leads to the formation of Fe vacancies in the FeS_m layer and layered compounds with the overall compositions $[Fe_8S_{10}][Fe(en)_3]$. $en_{0.5}$ and $[Fe_{9.4}S_{10}][Fe(en)_3]_{0.6} \cdot en_{0.9}$.

The composition $Li_{(1-x)}Fe_xOH$ represents bulk analyses with Fe:Li ratios of 1.093 to 1.132. Since the FeS_m component is stoichiometric, ⁸⁰ this suggests that $x \sim 0.1$ in $\text{Li}_{(1-x)}\text{Fe}_x\text{OH}$ and the intercalated compound is basically lithium hydroxide.

Hydrazine, N₂H₄, intercalation into FeS_m results in the formation of a layered compound with a composition $(N_2H_4)_{0.75}$ Fe₂S₂. 82 The intercalation causes an increase of the interlayer spacing to 8.7Å. The insertion of the electronically neutral compound, N₂H₄, coincides with a retention of stoichiometry in the FeS layer. There is a slight excess (<5 wt %) of Fe in the material but this, if it is real, may be located in the interlayer space. This suggests that the insertion of charged compounds into the vdW gap of FeS_m is responsible for causing vacancies in the Fe-S layer, which may have consequences for the development of superconductivity in these layered materials. The synthesis used $K_{0.8}Fe_{1.7}S_2$ as the starting material, and it is noteworthy that the ratio of N₂H₄ to FeS in the product is similar to that of K:FeS in the starting reactant (Table 7).

4.2. Interlayered Sulfide-Hydroxide Materials

4.2.1. Tochilinite-Group Compounds. Tochilinite embraces a group of minerals with mackinawite (FeS_m)- and brucite

 $(Mg(OH)_2)$ -like interlayers. The brucite-like layers distinguish the tochilinites from the FeS intercalation compounds described above, although the distinction is a little artificial if we consider the Li(OH) intercalation compounds. They were originally characterized in samples from the Cu-Ni zones of the Noril'sk deposits in Siberia 85 but have since been widely identified as accessory minerals in meteorites, particularly carbonaceous chondrites.86

The generalized composition of tochilinites is $2Fe_{(1-x)}S$. $n(Mg,Al,Fe)(OH)_2 (0.08 \le x \le 0.28 \text{ and } 1.58 \le n \le 1.75)^{.87}$ The reported compositions are commonly poorly constrained since they are based mainly on element ratios, Mössbauer analyses and electronic balancing and the few totals, where listed, may include ≤30 wt% unknown or undetermined components. The listing of compositions in Table 8 is simplified to the first decimal place apfu to take account of these uncertainties.

Tochinilites are characterized by tetragonal mackinawite layers intercalated with noncommensurate hexagonal brucitetype Mg(OH), layers. Brucite consists of sheets of Mg²⁺ sandwiched between two sheets of hydroxide anions. The XRPD spectra of tochinilites have been fitted to monoclinic unit cells with a = 5.2 - 5.5 Å, b = 15.3 - 15.9 Å, c = 10.7 - 10.9 Å, and β $= 93.6 - 95.8^{\circ}.^{92,93}$

The ideal tochilinite composition is 6FeS·5Mg(OH)₂. 88 The International Mineralogical Association lists the composition as 6(Fe_{0.9}S)·5[(Mg,Fe)(OH)₂]⁹⁰ which is mainly based on analyses of natural tochinilites reported by refs 89 and 92. Syntheses of tochinilite-like phases suggest a complete solid solution between Mg (6FeS·5Mg(OH)₂) and Fe (6FeS· 5Fe(OH)₂) end members with the Fe-rich member being equivalent to the mineral ferrotochilinite.⁸⁸ A particular characteristic of the brucite layer is the facile exchange of Mg^{2+} for other cations including Li⁺, Na⁺ Fe²⁺, Fe³⁺, and Al³⁺.

Synthetic ferrotochinilite has a reported composition Fe_{0.71}S·

0.79[Fe^{II}_{0.25}Fe^{III}_{0.73}Mg^{II}_{0.01}Al^{III}_{0.01}(OH)_{1.98}(O)_{0.02}].⁹¹
Mössbauer analyses of the Fe hydroxide layer showed that the iron is dominantly Fe^{III}:³⁰ indeed, the content of Fe^{II} in the ferromagnesium hydroxide layer was reported as 3 ± 3%, suggesting that Fe^{II} was effectively absent from this layer. This implies that the ferromagnesium hydroxide layer in synthetic ferrotochinilite is a charged complex, $\left[\text{Fe}_x\text{Mg}_{1-x}(\text{OH})_2\right]^{x+}\!,$ and the excess charge in the interlayer contributes to the stability of the compound and is balanced by Fe vacancies in the FeS layer. Aluminum can substitute for Mg in synthetic ferrotochinilite producing an Al-rich (5.3 wt % Al) variety with a reported composition $Fe_{0.89}S \cdot 0.85 [Fe^{II}_{0.55}Fe^{III}_{0.11}Al^{III}_{0.33}(OH)_{1.84}]$ $(O)_{0.16}]^{.91}$

Table 8. Examples of Natural and Synthetic Tochilinite Compositions Simplified to 0.1 apfu and Presented as the Ratio between the FeS Component and the Interlayered Brucite-Like Component

	brucite-like layer	FeS layer		ref
tochilinite	0.8Mg(OH) ₂	FeS	ideal	88
tochinilite	$0.8[Mg_{0.7}Fe_{0.3}(OH)_2]$	Fe _{0.9} S	natural	89
tochinilite	$0.8[(Mg,Fe)(OH)_2]^a$	Fe _{0.9} S	natural	90
tochinilite	$0.9 [Fe_{0.6}Mg_{0.4}(OH)_2]$	Fe ₀₈ S	synthetic	91
ferrotochinilite	$0.8 \text{Fe}(\text{OH})_2$	FeS	natural	88
ferrotochinilite	$0.8[FeAl(OH)_2]$	Fe _{0.7} S	synthetic	91
Al-tochinilite	$0.9[Fe_{0.7} Al_{0.3}(OH)_{1.8} (O)_{0.2}]$	Fe _{0.9} S.	synthetic	91
Na-tochilinite	$[(Na_{0.5}Fe_{0.5})(OH)_2]$	FeS	synthetic	80

^aInternational Mineralogical Association formula based on ^{89,92}

Table 9. Examples of Interlayered Sulfide-Hydroxide Materials of the Valleriite Group

sulfide moiety	hydroxide moiety	mineral name	structure	ref
(Fe,Cu)S	$0.75(Mg,Al)(OH)_2$	valleriite	hexagonal	
$(Fe_{0.6}Ni_{0.4})S$	$0.8(Mg_{0.8}Fe_{0.2})(OH)_2$	haapalaite	trigonal	97
FeS	CaAl(OH) ₅	vyalsovite	orthorhombic	98,99
$V_{0.875}S_2$	$[(Mg_{0.6}Al_{0.3}V_{0.1})(OH)_2]$	yushkinite	trigonal	100,101
$(Nb,Mo)S_2$	$(Mg_{1-x}Al_x)(OH)_{2+x}$	ekplexite	trigonal	102
$(Mo,Nb)S_2$	$(Mg_{1-x}Al_x)(OH)_{2+x}$	kaskasite	trigonal	102
$(Mo,Nb)S_2$	$(Mn_{1-x}Al_x)(OH)_{2+x}$	manganokaskasite	trigonal	102

ı

By contrast, Na-tochinilite has a composition FeS- $[(Na_{0.5}Fe_{0.5})(OH)_2]$ with approximately half the cations in the hydroxide layer filled by Fe^{III} which satisfies the electroneutrality of an Mg(OH)₂, brucite-like interlayer, and no vacancies in the FeS_m layers. ⁸⁰ The d_{001} spacing is 10.72 Å, or twice that of normal mackinawite.

4.2.2. The Valleriites. Both the sulfide and hydroxide moieties in layered sulfide-hydroxide materials can vary considerably in composition and the tochinilites form part of a wider group of quasi-two-dimensional layered chalcogenide minerals, the valleriites. The minerals and their synthetic equivalents in the valleriite-group are characterized by variable sulfide moieties with brucite-like interlayers.

Valleriite itself was first identified by Blomstrand in 1870⁹⁴ and named after his Swedish chemical mentor Johan Gottschalk Wallerius (1683–1742), the first Professor of Chemistry at Uppsala University. In valleriite, the tetragonal FeS_m sheets of tochinilite are replaced by (Fe,Cu)S and Al substitutes for part of the Mg in the hydroxide layer. ⁹⁵ The (Fe,Cu)S layer has a rhombohedral structure (*R*3*m*) which has been compared to that of nukundamite, a layered (Cu,Fe)₄S₄ compound that resembles covellite, the common copper sulfide, CuS. ⁹⁶ The hydroxide layer retains the structure (*P*2*m*) of the tochinilites.

In most of the $\mathrm{FeS_m}$ -hydroxide layered materials the Fe is in tetrahedral coordination and the hexagonal hydroxide layers are noncommensurate. However, in the valleriite-group the sulfide moiety can be substituted by compounds with structures which are commensurate with the hexagonal hydroxide moieties (Table 9). In vyalsovite, for example, the FeS and $\mathrm{CaAl}(\mathrm{OH})_{5}$ layers are commensurate: the FeS has the hexagonal troilite structure where the Fe is in octahedral coordination and the $\mathrm{CaAl}(\mathrm{OH})_{5}$ layer has an hexagonal, brucite-like structure.

In haapalaite the FeS moiety is replaced by FeNiS with compositions between Fe $_{0.6}$ Ni $_{0.4}$ S and Fe $_{00.8}$ Ni $_{0.2}$ S in minerals and synthetic equivalents. Its crystalline structure has been suggested to be similar to a variety of FeNiCu sulfides 103 although Huhma et al. 97 originally thought it was simply Ni substituting for Cu in a valleriite-like rhombohedral sulfide layer structure. The Mg(OH) $_2$ -type interlayer material in haapalaite has a brucite-like structure and the ratios of the sulfide to hydroxide moieties in haapalaites are similar and vary between 0.8 and 0.9.

Yushkinite also displays commensurate hydroxide and sulfide layers but, in this case, the FeS_m moiety is replaced by VS₂. VS₂ is a layered material consisting of an hexagonally packed metal V layer sandwiched between two layers of S atoms. There is a rich burgeoning chemistry of vanadium sulfides because of their importance to energy storage and conservation. ¹⁰⁴ In ekplexite, kaskaite and manganokaskaite, the sulfide moiety is a molybdenum – niobium sulfide with a molybdenite (MoS₂)-like trigonal structure and the brucite-type hydroxide layers

include Al^{III} as well as Mg^{II} . In manganokaskaite, the Mg^{II} in the brucite layer is replaced by Mn^{II} .

4.3. Partially Oxidized Forms of FeS_m

A number of reports have described partially oxidized forms of nanoparticulate FeS 35,28,105,106 and, in some cases, these have been interpreted as precursor phases to FeS $_{\rm m}$. The reported compositions of these phases are highly variable, possibly change with time and are poorly constrained. There seems to be a virtually unlimited number of possible FeS_m precursor solids based on (a) the chemistry of nanoparticles (b) the sensitivity of the Fe and S moieties to oxidation and (c) the effects of variable stacking architectures, and exotic intercalations, on the product material. 106 The relative importance of these materials to the formation of FeS_m is moot, since several have been defined in acid media where FeS_m dissolves rapidly. ¹⁰⁶ Likewise, the facile transformation of FeS_m to the thiospinel, Fe₃S_{4g}, produces cryptic admixtures of the more oxidized phase in FeS_m. 107 If probed in midtransformation, iron sulfide phases with variable stoichiometries, compositions and electromagnetic properties can be encountered. However, the possibility of tuning the electromagnetic properties of FeS_m is potentially very pertinent to materials chemists searching for cheap superconducting materials. By analogy with recent advances in pharmaceutical chemistry it may be that search protocols

involving artificial intelligence may be applicable. A general formulation NaFe $^{II}_{\ a}$ Fe $^{III}_{\ b}$ S $^{II-}_{\ c}$ (S $_{n}^{II-}$) $_{d}$ (S $_{2}^{II-}$) $_{e}$ might encompass the composition of all these phases, including FeS $_{m}$. In terms of atoms per formula unit (apfu), z=0.0-0.8, a=0.5-1.0, b=0-0.5, c=0.5-1, d=0.0-0.2 and e=0.0-0.1. The compositions appear to be limited by Fe $_{3}$ S $_{4g}$ (a=0.3, b=0.7, c=1.0, d=0.0, e=0.0) and FeS $_{2p}$ (a=1.0, b=0.0, c=0.0, d=0.0, e=1.0). o=0.00.

These oxidized phases have been synthesized in aqueous solution with NaHS, by slowly diffusing $\rm H_2S$ gas into an acidic (pH < 4.5) aqueous $\rm Fe^{2+}$ solution, electrochemically and by adding excess sodium hydroxide to a ferrous salt. 105,106,108 These materials have been designated as $\rm FeS_{nano}^{106}$ and S-FeS. 108 Neither of these designations is useful and they may be misleading: $\rm FeS_{nano}$ might be assumed to refer to any of the wide varieties of nanoparticulate FeS, and S-FeS does not describe the Na content of this phase and might be confused with the original S-rich FeS_m phases 66,109 which were shown to be due to analytical errors 12,110 Both abbreviations are best avoided. 105 The detailed structures of these phases are unknown although they all seem to possess the conventional layered FeS_m structure. The reported interlayer spaces vary between 12.1 Å 106 and 8.0 Å 108 compared to 20 Å 108 compared to 20 Å 108 for FeS_m. The reported Fe—Fe bond distance ranges from close to the Fe—Fe (FeS_m) of 2.6 Å 108 to

Some of these partially oxidized FeS nanoparticles appear to be similar to the compositionally variable biologic FeS clusters.¹¹¹ The hypothesis that nucleation may proceed via a

Table 10. Examples of Synthetic Products Related to FeS_m^a

product name	Fe reactant	separation method	product identification	citation
abiotic mackinawite	$FeCl_2$	filtered, dried	XRPD, SEM, TEM, EDS	112
amorphous FeS	Fe acetate	liquid N_2 freezing	XAS	113
amorphous iron sulfide	$FeCl_2$	gravity settling	TEM-EDS	114
amorphous Fe(II) monosulfide	Mohr's	filtered, freeze-dried	XRPD	115
biotic mackinawite	$FeCl_2$	filtered, dried	XRPD, SEM, TEM, EDS	112
crystalline FeS	wire	filter dried	XRD	116
disordered mackinawite Mk A	Mohr's	freeze-dried, suspension	LAXRPD, TEM	21
disordered mackinawite Mk B	Mohr's	freeze-dried, suspension	LAXRPD, TEM	21
disordered tetragonal mackinawite	Mohr's	suspension	XRPD	117
Fe(II) sulfides	FeSO ₄	suspension (Raman), filtered (XRD)	Raman, XRPD	118
Fe(III)-containing mackinawite: $Fe^{II}_{1-3x}Fe^{III}_{2x}S$	$FeCl_2$ or $FeSO_4$	filtration (XRD) and decanting suspension (XPS)	XRD, Raman	35
Fe ³⁺ and S_n^{2-} -containing mackinawite: Fe ²⁺ _{1-3x} Fe ³⁺ _{2x} S ²⁻ _{1-y} (S_n^{2-}) _y	FeCl ₂	suspension (voltammetry); hot plate drying (60 °C) XANES; vacuum drying (Raman)	voltammetry, XAS, Raman	105
FeS	$FeCl_2$	freeze-dried	XRPD	119
FeS	$FeCl_2$	centrifugation	XPS, SEM,	120
FeS_{aged}	Mohr's	filtered, N ₂ -dried	synch XRD	116
FeS_{am}	FeSO ₄	freeze-dried	XRD	36
FeS_{fresh}	Mohr's	filter, N ₂ -dried	synch XRD	116
FeS nanoparticles	FeSO ₄	freeze-dried	XRPD	121
FeS nanoparticles	FeSO ₄	suspension	EDX-SEM, FTIR	122
$FeS_m (+ Fe_3S_{4g})$	$FeCl_2$	freeze-dried	XRPD	123
FeS _{nano} , Fe ²⁺ _w Fe ³⁺ _x S ²⁻ _y (S _n ²⁻) _z	Mohr's	vacuum filtration	XRPD, HRTEM, Raman, XPS, XAS	106
iron monosulfide FeS	$FeCl_2$	centrifuge	XRPD, HRTEM, SAED, EDS	24
mackinawite	Mohr's	suspension	XRPD	37
mackinawite	$FeCl_2$	suspension	XRD	124
mackinawite		freeze-dried	XRPD	124
mackinawite	FeSO ₄	freeze-dried	synch XRPD, Raman, TEM-EDX-SAED	125
mackinawite and SiO ₂	$FeCl_2$	suspension, dried	SEM, TEM, EDX	126
mackinawite and greigite	Mohr's	freeze-dried	XRPD	37
nanocrystalline FeS	$FeCl_2$	freeze-dried	XRPD	127
nanocrystalline FeS	Mohr's	filter, dried	XRD	116,128
nanocrystalline mackinawite	Mohr's	filtered	XRPD	129
nanocrystalline mackinawite	FeSO ₄	freeze-dried	XRPD	36
nanosized mackinawite (FeS)	$FeCl_2$	freeze-dried	XRPD	130
poorly crystalline mackinawite	$FeCl_2$	freeze-dried	XRPD	131-137
precipitated FeS	FeSO ₄	filtering, freeze-dried	XRPD, SEM, HRTEM	36
tetragonal FeS	iron powder	filtered, dried	EDS, XRF, XRPD	57
tetragonal FeS _{1-x} mackinawite	iron wire	freeze-dried	XRPD, Mössbauer, XPS	28,138
tetragonal iron (II) monosulfide, $\mathrm{FeS_m}$	Mohr's	freeze-dried	wet chemical analysis, ICP-OES; ion chromatography, solid state NMR; TGA, TGA-MS	12
tetragonal iron sulfide, FeS	$K_x Fe_{2-y} S_2$	washing	single crystal XRD	31,56
biotic FeS	ferrihydrite	freeze-dried	SEM-EDS- XRD, Raman, TEM	139
abiotic FeS	$FeCl_2$	freeze-dried	SEM-EDS-XRD, Raman, TEM	139
biotic mackinawite	Fe(III) citrate	vacuum-dried	XRPD, TEM, EDS	140

"Product name refers to the name of the product given by the cited report authors. The Fe reactant refers to the Fe compound used in the synthesis: $FeCl_2$ is generally the hydrate $FeCl_2 \cdot H_2O$; $FeSO_4$ is generally the heptahydrate $FeSO_4 \cdot 7H_2O$; Mohr's is Mohr's salt, $(NH_4)_2Fe(SO_4)_2 \cdot 6H_2O$; iron wire is of undefined purity. The product identification lists the major methods used to characterize the product and are defined in Table 2. The citations refer to reports which use the material designation.

two-step process involving the initial cluster formation and nucleation of the solid phase within the clusters, is similar to the proposal that variable compositions of the partially oxidized FeS nanoparticles may lead to the nucleation of other iron sulfide phases, such as ${\rm Fe_3}S_{\rm 4g}$ and even ${\rm FeS_{2p}}$. The formation of these phases in poorly defined synthesis protocols might explain some of the variable, irreproducible and empirical results of FeS chemistry reported in the literature.

5. SYNTHESIS

The synthesis of a reproducible, defined ${\rm FeS_m}$ material has been a major hindrance to understanding the properties of ${\rm FeS_m}$. A selection of reported syntheses of ${\rm FeS_m}$ are listed in terms of the authors' reported description of the product, the reactants used, the method of preparation and the analytical methods used, are listed in Table 10.

During the latter decades of the 20th century, the Cardiff lab sent samples of defined FeS_m to laboratories worldwide as a

standard material. Unfortunately, many laboratories continued to synthesize FeS_{m} with their own recipes giving rise to a suite of poorly defined, usually oxidized and often mixtures of several phases, which produced unreproducible results. In many cases compilations merely list undefined FeS as a reactant and this may include pyrrhotite as well as tetragonal FeS. For example, in refs 141 and 142. the FeS reactant was Aldrich, technical grade iron sulfide which is mainly crushed, $\text{Fe}_{1-x}\text{S}_{\text{po}}$, synthetic pyrrhotite.

The preparation protocols for synthetic FeS_m include minor variations which may have substantial effects on the reproducibility of the results. For example, freeze-dried FeS_m does not dechlorinate cis-DCE whereas aqueous suspensions of FeS_m are effective dechlorination agents. ¹²⁴ One multisite investigation reported different reaction products (described as amorphous FeS and nanocrystalline mackinawite) from the same synthetic reaction in anaerobic chambers in the different laboratories. ³⁶

The initial solution reaction between a dissolved Fe(II) salt and aqueous S(-II) would appear straightforward. However, many of the iron salts used as reagents in the reaction are readily oxidized. For example, Fe(II) chloride and sulfate become rapidly discolored in solid form, reflecting oxidation, and the reagents, even in their original jars, are generally unusable for FeS_m syntheses if already opened. Mohr's salt, $(NH_4)_2$ Fe $(SO_4)_2$. $6H_2O$, is a more reliable reactant and less prone to oxidation. This has been widely used in FeS_m syntheses. 21,37,117,129 Experimental protocols using a form of FeS_m synthesized from ferrous chloride as a reactant 114,120,123,127,131,132 may give various results. This is often caused by intrinsic oxidation of the ferrous chloride reactant taken directly off the lab bench. Anhydrous ferrous chloride is white when fresh but rapidly takes on a tan hue due to oxidation. The more common hexahydrate is pale green when pure, but the reagent is often brownish on the lab bench due to the formation of Fe(III) oxyhydroxides. This means that the ferrous chloride reactant may contain various amounts of Fe(III) leading to contamination of the FeS_m product by various amounts of Fe^{III}, usually in the form of Fe₃S_{4g}, and S₂^{II-}, sometimes as FeS_{2p}. Commercial FeCl₂·4H₂O powder can be stored in anoxic chambers directly after delivery to alleviate the incipient oxidation problem. 112

Ferrous sulfate is commonly used in the form of the bluegreen heptahydrate but this rapidly discolors in air. However, no differences were detected in the nature of the precipitates nor in their aging characteristics between FeS_m synthesized with $FeCl_2$ or $FeSO_4$.

There has been much discussion about the effects of freezedrying aqueous FeS suspensions. Early syntheses involved alcohol-ether drying of filtered material 143 under a $\rm N_2\text{-}hood$ and this process was later modified to drying under a stream of N2 gas. 116 Freeze-drying was originally introduced into FeS_m syntheses in order to produce reproducible material with a defined weight, surface area and surface chemistry that could be used as a reactant in further experimental investigations. Freeze-drying was further found to prevent structural evolution of FeS_m precipitates.²¹ Although there is little intrinsic difference between freeze-dried and precipitated FeS_{m} , ^{19,124} aggregation of the FeS_m particles can lead to a reduction in surface area and a consequent reduction in reactivity.³⁷ Freeze-dried FeS_m often includes oxidized compounds such as Fe₃S_{4g} and iron oxyhydroxides 37,144 which are not present in the nonfreeze-dried material. The process involves removing water by freezing the FeS_m under vacuum so that the water–ice sublimates. There is no reason why this process, in itself, should cause oxidation.

However, transporting FeS_m in air to the freeze-drier and taking more time to pump the system down to machine vacuum exposes it to oxidation. One way to overcome this is to site the whole of the operation, including the freeze-drier, in an anoxic chamber. The Cardiff lab used a large MBraun Labmaster 130 anoxic chambers with O2-levels maintained at less than detectable levels (<1ppmv) in which synthesis, separation and freeze-drying were carried out. Indeed, the material could be sealed in glass ampoules within the chamber for dispatch to other laboratories overseas.¹⁹ The precision of the system was demonstrated by analyses of the FeS_m which showed totals of 99.35 ± 0.02 wt%; ¹² that is, even if the missing material in the totals was due to oxidation rather than the more probable intrinsic analytical uncertainty, the amount of O₂ must be less than 0.65 wt% or far too little to account for any significant content of iron oxyhydroxide. Likewise, the analyses showed stoichiometric Fe_{1.00±0.01}S which precludes the presence of Fe₃S_{4g}. This is consistent with the XRD analyses which did not detect any greigite peaks, although this is a relatively insensitive control on sample purity because the technique may not detect <10 wt% of a separate phase. Freeze-drying FeS_m in air can produce inconsistent results¹⁴⁴ but, as pointed out by the Michigan lab, 145 consistent use of the same synthesis method over many years of research can produce consistent results.

In the Cardiff lab, XRPD was carried out in an environmental chamber which was loaded in the anoxic chamber. ¹¹⁵ It is obvious that the material will be oxidized if transported in air to the XRD system and be further exposed to O_2 while the system is pumped down. This means that the results of XRD analyses may not accurately reflect the nature of the original material but merely reflect artifacts of sample handling.

Vacuum filtration of the material in suspension, often in combination with alcohol-ether drying, has been widely used since it was introduced in 1969. 143 This process may take up to 3 h^{118} and thus oxidation cannot be avoided if the filtration is not carried out under strictly anoxic conditions. 118,143 If oxygen is present the process can result in the precipitate igniting in the filter crucible since the material is variously pyrophoric (see section 10.1) , a spectacular, if somewhat risky, test for oxidation of FeS...

Syntheses of larger mackinawite crystals can be achieved by using metallic iron as a reactant rather than a dissolved iron salt, with 32 or without 23 an applied current. The method produces crystals 0.8 μ m in size, ²⁷ more than 100× the size of precipitated FeS_m. ^{19,21} Even though these crystals are small, they are large enough to limit line-broadening effects on XRD patterns and this material was used to provide the definitive structural data for FeS_m.²³ Repetition of the original synthesis revealed greigite in the product. 116 The authors speculated that the greigite developed from Fe^{III} in the iron wire they used as a reactant. A unique set of published analytical results from the hydrothermal syntheses of FeS_m with iron are shown in Figure 5 recalculated from experimentation reported by ref 57. The analyses were made by EDS which does not report total analyses so that the analytical uncertainties are unknown (see section 4). Even so, it is clear from the data that the reactions were incomplete, and unreacted iron was present in the products which is a common problem in heterogeneous reactions.

It is obvious that, in order to more confidently probe the electrical and magnetic properties of $FeS_{m'}$, it is necessary to ensure that the material being investigated is, in fact, FeS_m . The results emphasize the sensitivity of the reaction product to the reagents used in the synthesis, to the method of synthesis, to the

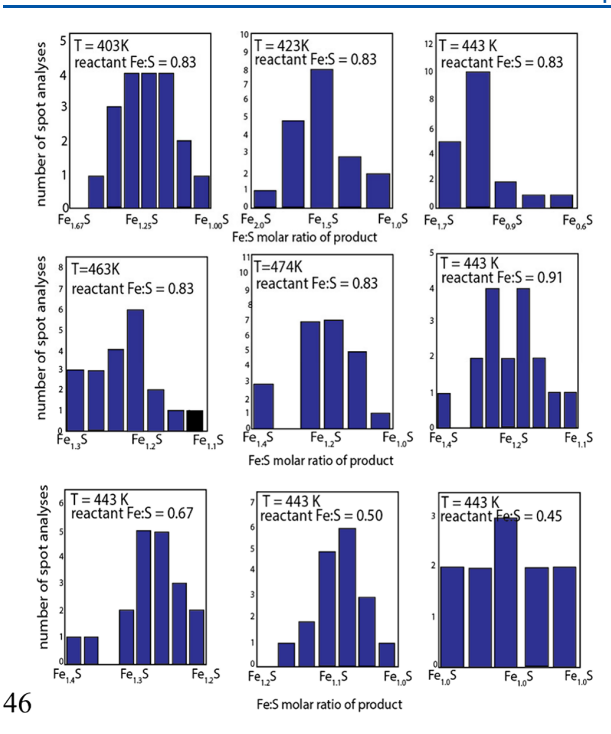


Figure 5. Example of the variation in Fe:S molar composition from the hydrothermal synthesis of FeS_m with metallic Fe: EDS analyses of reaction products T between 403K (130 °C) and 474K (201 °C) for reactions at different molar Fe:S reactant ratios. Recalculated from data in ref 57.

handling of the reaction product and to the analytical method used to define the composition. It may well be that molar Fe:S ratios in the product approaching 1.0 are good tests of the success of the synthesis of FeS_{m} .

The small size of the synthesized FeS_m restricted further investigations into this material until 2016 when Borg et al.³ reported syntheses of FeS_m crystals up to 8 mm in size. The major breakthrough came through the discovery that the intercalated, ternary phase $K_x Fe_{2-y} S_2$ (section 4.1) is thermally stable. FeS_m is metastable and the conventional method for the formation of single crystals through slow cooling of a melt is not possible. However, large platy $K_x Fe_{2-\nu} S_2$ crystals (8 mm × 1 mm thick) can be prepared from a mixture of hexagonal pyrrhotite and metallic K heated to 1000 °C to form an homogeneous melt and slowly cooled.^{31,81} Borg et al.³¹ used these thermally stable K_xFe_{2-v}S₂ single crystals as a starting material and chemically removed the interlayer material. $K_x Fe_{2-y}S_2$ crystals were added to an autoclave at 120 °C for 3-4 days with metallic Fe powder, Na₂S, NaOH, and H₂O. Silver colored FeS_m crystals up to 8 mm in diameter were recovered by washing away excess Fe powder. The crystals had a mackinawite-like structure and the Rietveld refinement showed a = 3.683 Å and c = 5.034 Å which compares with the standard FeS_m dimensions of a = 3.674 Å and c = 5.033 $Å^{23}$ (Table 3). The Fe-Fe distance in the square planar array is 2.604 Å compared with 2.597 Å of the standard synthetic material. The possibility of synthesizing large well-defined FeS_m crystals means that further details of the chemical and physical properties of this material can now be probed. 56,146

The definition of the product is often uncertain because of the dependence on structural identification, usually using a form of X-ray diffraction, and the lack of reported compositions. If the

composition of the material is reported, it is often couched in terms of Fe:S ratios usually obtained by physical methods such as energy dispersive spectroscopy. As discussed in section 4, the problem is the lack of analytical totals which not only provide information on the uncertainty of the stoichiometry but also indicate the presence of elements other than Fe and S in the material.

FeS-coated iron nanoparticles have been proposed for use in environmental remediation. ^{127,130,147–149} However, the amount of sulfur in these particles is limited (e.g., 7.5 at. wt % by XPS¹²⁷) and no FeS compound was detected by XRPD; the dominant solid constituents are metallic Fe and Fe oxyhydroxides. Although these materials may have potential in environmental remediation, they do not feature in this review since, at present, there are insufficient data on the nature of the FeS phase.

6. STABILITY

The standard Gibbs free energies of formation for the species used in thermodynamic computations in this review are listed in Table 11 together with the estimated uncertainties.

Table 11. Standard Gibbs Free Energies of Formation (ΔG°_{fi}) and Estimated Uncertainties for Species Considered Here (Modified from Table 3 in ref 150)

species	mineral equivalent	$\Delta G^{\circ}_{f_{\stackrel{.}{1}}}$ $(kJ \text{ mol}^{-1})$	uncertainty (kJ mol ⁻¹)	source
H_2S_{aq}		-27.8	±0.1	151
HS-		12.1	±0.1	151
SO_4^{2-}		-744.4	±0.4	152
H_2O_1		-237.1	±0.0	152
FeS ⁰ _{aq}		-65.8	±2.4	153
Fe ²⁺		-90.5	±1	154
FeS_m	mackinawite	-97.44	±2.4	155
Fe_3S_{4g}	greigite	-433.5	±0.6	156
FeS_{2ma}	marcasite	-158.3	±2	157
FeS_{2p}	pyrite	-160.2	±2.1	158
FeS_t	troilite	-101.3	±2.0	157
$Fe_{0.9}S_{po}$	5C pyrrhotite	-97.9	±2.2	157
$Fe_{0.875}S_{po}$	4C pyrrhotite	-97.0	±2.0	157
$Fe_{0.82}S_{sm}$	smythite	-95.1	±2.0	150
lpha-FeOOH	goethite	-488.6	±1.7	154

6.1. Solubility of FeS_m

The thermodynamic stability of FeS $_{m}$ has been measured by solubility measurements. The solubility of FeS $_{m}$ in aqueous solutions is different in two pH regimes: at pH \lesssim 6 the solubility is dependent on pH; at pH \gtrsim 6, the solubility is independent of pH. The results mean that the solubility can be described by two equations (2¹⁵⁵) and (3^{153,155}).

$$pH < 7$$
 $S_m + 2H^+ = Fe^{2+} + H_2S_{aq}$ $log K_1 = -3.34$ (2)

$$pH < 7 eS_m = FeS_{aq}^0 log K_0 = -5.7$$
 (3)

In the acidic regime, the solubility is dependent on the square of the H^+ activity; in the alkaline regime, the pH independence of the solubility means that H^+ is not involved in the product and the solubility is described in terms of the intrinsic solubility, where FeS^0_{aq} represents the Fe(II) sulfide cluster monomer. The

transition between the two pH regimes is dependent on the activity of $H_2S_{aq\prime}$ which in turn is a function of the total dissolved sulfide concentration, $\sum[S(-II)]$. For example, the limits of the solubility regimes are pH \sim 7 at $\sum[S(-II)]\sim10~\mu\text{M}$ and pH \sim 6 at $\sum[S(-II)]\sim1$ mM. 153 There is a third solubility regime, which proved important in wet chemical analyses of FeS_m (section 4), in the pH-pe region where elemental sulfur is stable. In this region, which is located in very acidic solutions near the $H_2S/SO_4(-II)$ equal activity boundary, 12 elemental sulfur is a product of the dissolution.

The extreme variation in reported historical values for the Gibbs free energy of formation of $\mathrm{FeS_m}$ has been mainly due to the variable quality of the experimental protocols employed. S3,155 More recent values are listed in Table 12. The

Table 12. Gibbs Free Energy of Formation for FeS_m (ΔG_f° kJ mol⁻¹)

$\Delta G_f^{\circ}(\mathrm{kJ\ mol^{-1}})$	ref
-98.2 ± 2.4	153
-96.68 ± 3.18	157
-97.44 ± 2	155

value of $-97.44~kJ~mol^{-1}$ was derived by application of a Pitzerbased thermodynamic model together with refined optimization treatment of the new and published experimental data. 155 The reported value is the mean of the two earlier substantive values. 153,157 The Gibbs free energy of formation for FeS $_{m}$ is $-97.44\pm1~kJ~mol^{-1}$ (Table 12). 153,155,157

The thermodynamic data listed in Table 13 show that FeS_m is unstable with respect to Fe₃S_{4g}, FeS_{2p}, FeS_{2ma} and FeS_t. The thermodynamic stability of FeS_m with respect to the pyrrhotites, Fe_{1-x}S_{po} and Fe_{0.82}S_{sm}, smythite, is presently poorly constrained because of the relative uncertainties in the thermodynamic data. However, it appears that FeS_m is unstable relative to all these phases 150 and ΔG° , must be > \pm 0 kJ mol $^{-1}$.

The measurement of the change in solubility of FeS_m with temperature is important for understanding and predicting steel corrosion in sulfidic environments, especially sour gas pipeline corrosion. However, it is experimentally challenging since metastable FeS_m is continuously equilibrating at all temperatures to form Fe_3S_{4g} and $Fe_{1-x}S_{po}$ (see section 6.3), and the rate of equilibration is partly temperature dependent.

$$pK^{0}(FeS_{m}) = -94.97 + 4444/T + 14.64(lnT)$$
(4)

Using a Pitzer-based thermodynamic model the temperature dependence of the FeS_m solubility product $(pK^0(FeS_m))$ can be

described by equation 4 where the temperature T is between 296K (23 °C) and 398K (125 °C). LSS

The FeS_m solubility product decreases by about 0.5 log units over this temperature range and the Gibbs free energy of reaction increases by around 10 kJ mol⁻¹ (Table 14). The

Table 14. Temperature-Dependence of the Solubility Product of FeS_m ($log K^0(FeS_m)$) and the Computed Standard Deviation ($\pm 1 \ sd)^{155}$

temperature (°C)	(K)	$\log K^{\circ} (\text{FeS}_{\text{m}})$	±1 sd
25	298	-3.34	0.04
50	323	-3.36	0.06
60	333	-3.40	0.06
70	343	-3.44	0.06
90	363	-3.56	0.08
100	373	-3.63	0.11
125	398	-3.83	0.24

uncertainties in these results are likely to be considerable at temperatures much above 70 °C where anecdotal evidence suggest that the rate of equilibration becomes more rapid. Even so, the data may be useful in contributing to controlling FeS scaling and sulfide corrosion in industrial systems, where changes in the product iron sulfide may reflect changes in the real world.

The effect of pressure on the solubility of FeS_m has been considered. In the absence of experimental measurements, it has been suggested that the pressure dependence could be assumed to be similar to that of troilite, hexagonal FeS_v , since the effect of pressure is mainly due to the molar volume change of the aqueous species and it might be assumed that the two phases have similar aqueous ion compositions. However, the solubility of troilite is pH dependent, and any pH space where the dissolution is independent of H^+ (and where neutral species such as FeS_0^0 may dominate the speciation as is the case with FeS_m), has not been reported. The pressure effect on the solubility of troilite is relatively small up to 50 MPa but the implications for FeS_m solubility remain extremely uncertain.

6.2. Surface Energy of FeS_m

There has been some interest in exploring the interface between equilibrium thermodynamics and kinetics with respect to transformations in the iron sulfide system in aqueous solutions around STP. This classically dangerous terrain appears to be further elucidating the chemistry of $\text{FeS}_{\text{m}}.$ The discussions center on interrogations of the surface energies of FeS_{m} and related iron sulfides.

Table 13. Stability Relationships in the Fe-S System Computed from Thermodynamic Data Listed in Table 11^a

formulation	structure	mineral equivalent	reaction	$\Delta G^{\circ}_{r} (\mathrm{kJ} \; \mathrm{mol}^{-1})$
Fe_3S_{4g}	cubic	greigite	$3FeS_m + S^0 = Fe_3S_{4g}$	-138.9
$Fe_{1-x}S_{po}$	monoclinic/hexagonal	pyrrhotite ^b	$FeS_m + (1 - x)^{-1}S^0 = Fe_{1-x}S_{po}$	>±0
$\mathrm{Fe_{0.82}S_{sm}}$	rhombohedral	smythite	$FeS_{m} + 0.22S^{0} = Fe_{0.82}S_{sm}$	>±0
$\mathrm{FeS}_{\mathrm{2p}}$	cubic	pyrite	$FeS_{m} + S^{0} = FeS_{2p}$	-62.8
$\mathrm{FeS}_{\mathrm{2ma}}$	orthorhombic	marcasite	$FeS_{m} + S^{0} = FeS_{2ma}$	-60.9
FeS_t	hexagonal	troilite	$FeS_m = FeS_t$	-3.9

^aThe total uncertainty in the ΔG° , values for the Fe_{1-x}S_{po} and Fe_{0.82}S_{sm} reactions exceeds ± 4 kJ mol⁻¹¹⁵⁰ and ΔG° , is indicated as > ± 0 kJ mol⁻¹. ^bpyrrhotite includes 4C and 5C pyrrhotites.

All published surface energy estimates for FeS_m are derived from DFT model calculations ^{39,161–165} and vary according to the sophistication of the DFT model employed. Two examples are listed in Table 15. The computed values for the dominant (001) surface vary between 0.05 and 0.07 J m⁻².

Table 15. Variations in Computed Surface Energies for Various FeS_m Crystal Faces

Miller plane	surface energy $(J m^{-2})^{161}$	surface energy $(J m^{-2})^{39}$
(001)	0.05	0.07
(011)		0.60
(100)	0.97	0.71
(111)	1.10	0.75
(110)	1.40	1.16
(010)		0.71
(101)		0.60

The advantage of applying classical nucleation theory (CNT) approximation to surface energy estimates is that it can be used to interpret experimental data.

$$R_{\rm N} = A \exp[-(B\gamma^3 v_{\rm m}^2)/(\mathbf{k}^3 T^3 (\ln \Omega)^2)]$$
 (5)

The CNT rate of homogeneous nucleation of nuclei per unit volume per second, $R_{\rm N}$, is given by equation 5 where A is a preexponential constant, B is a shape factor, γ is the surface energy (J m $^{-2}$), $\nu_{\rm m}$ is the molecular volume (20.45 \times 10^{-6} m 3 molecule $^{-1}$ for FeS $_{\rm m}$), k is Boltzmann's constant (1.38 \times 10^{-23} J K $^{-1}$), T is the temperature in K, and Ω is the supersaturation. The pre-exponential constant, A, is a kinetic quantity which considers the concentration of nucleation sites, the frequency of attachment of monomers to the nucleus and the Zeldovich factor, a measure of the probability that the critical nucleus will go on to form a particle and not dissolve. The pre-exponential factor, A, ranges from 10^{13} to 10^{41} m $^{-3}$ s $^{-1166}$ and is mostly around $10^{33\pm3}$ cm $^{-3}$ s $^{-1}$. 167,168

The experimental data for FeS_m nucleation from aqueous solution at STP is described in section 7.1. The experimentally observed supersaturation is given by the ratio of the ion activity product (Fe(II))(S(-II)) to the solubility product, $K_{sn}(FeS_m) =$ 10^{-5.7}, 153 and is independent of the activity coefficients of the constituents. The experimentally observed rate $R_{\rm N}$ = 5 × 10²¹ FeS_m nuclei $m^{-3}s^{-1}$ for FeS_m nucleation from aqueous solutions at T = 298 K. B is a shape factor varying between $16\pi/3$ (~18) for a spherical nucleus and 32 for a cubic nucleus. The shape of the FeS_m nucleus is unknown but if it is similar to the shape of the smallest observed particle it is $2 \text{ nm} \times 3 \text{ nm}$ in size ¹⁹ and can be approximated as cuboid. The shape factor, B, then approaches 32. The surface energy computed from equation 5 is 0.02 J m⁻². Since the surface energy term is cubed in equation 5, the result is relatively insensitive to uncertainties in the experimental input data and the estimated uncertainty is of the order of ± 0.003 J m⁻³. The result is consistent with the computed surface energies for FeS_m (001) (Table 15).

The relative consistency of the surface energy estimates derived from CNT model of experimental data and nonclassical computed DFT models suggests that there is a low energy barrier of transition from the aqueous FeS cluster to the solid ${\rm FeS_m}$ nucleus. 169 This contrasts with ${\rm Fe_3}{\rm K_{4g}}$, for example, where experimental and computed surface energies diverge by a factor of 10. 161,170

Since the surface energy is closely related to the equilibrium or Wulff shape of the crystal, Wulff-averaged surface energies around 0.15 J m⁻² can be computed. ^{161,165} This value for the surface energy is not consistent with the experimental rate data for FeS_m nucleation. Figure 6 shows that a surface energy of 0.15

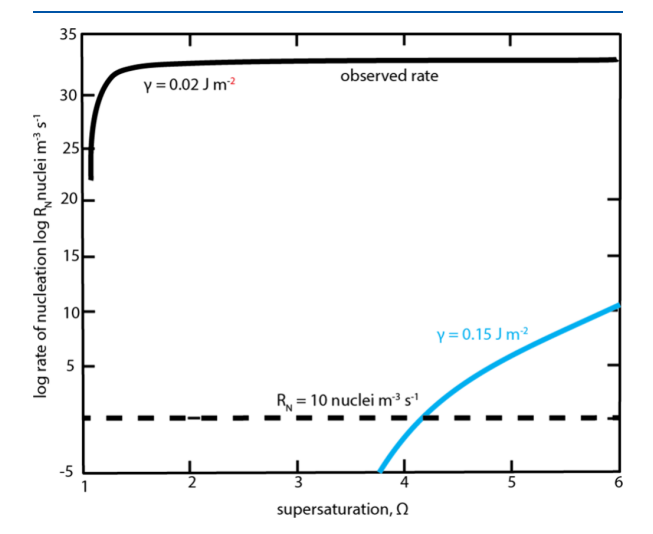


Figure 6. Logarithm of the rate of nucleation R_N (nuclei m⁻³ s⁻¹) versus the supersaturation, Ω, for FeS_m in aqueous solution at STP according to equation 5 for various values of the surface energy, γ (J m⁻²). The limiting rate $R_N = 10$ nuclei m⁻³ s⁻¹ is indicated.

J m⁻² leads to an extremely low nucleation rate, as calculated by equation 5. At $\gamma=0.15$ J m⁻² the supersaturation would need to be greater than 4 (i.e., Fe(II) = S(-II) = 3 mM) for a minimum 10 FeS_m nuclei m⁻³ s⁻¹ to be formed and the observed rate of 5 × 10²² nuclei m⁻³ s⁻¹ would only be reached at impossibly high supersaturations. The conflict between the Wulff-shape averaged surface energy of 0.15 J m⁻² and the observed surface energy of 0.02 J m⁻² is due to the observed shape of FeS_m nanocrystals (Figure 14). ^{19,52} The mean surface energy is closer to that computed for (001) since FeS_m nanoparticles have tabular, equilibrium shapes.

There have been some conflicting reports on the variation of surface energy with particle size, especially with regard to nanoparticles. The result appears to depend on the approach used for the computation. CNT, for example, includes the fundamental assumption that the surface energy is independent of size whereas nonclassical thermodynamic and molecular approaches suggest size-dependence.

The surfaces of nanoparticulate FeS_m are hydrated in aqueous solutions and these hydrated surfaces have smaller surface energies than anhydrous surfaces. ¹⁷¹ The magnitude of the contribution of hydrated surfaces to surface energies for FeS_m particles is unknown. It has been estimated for iron oxides to be $\leq \sim 20-30\%$ relative to the anhydrous forms ^{161,172} and this value has been assumed for iron sulfides. ²⁷ FeS_m particles are initially highly hydrated and dehydration is a major process during particle nucleation and the formation of the first surfaces (section 7). It seems intuitively correct that the energy required to form the first surface of FeS_m is extremely low.

Experimental observations suggest that the critical supersaturation at STP for FeS_m – the maximum supersaturation that a solution of Fe(II) and S(–II) can endure without a detectable amount of FeS_m forming, is <~10 (i.e., Fe(II) = S(–II) < ~5 mM). This can be checked by setting $R_{\rm N}$ in equation 5 to a limiting rate of 1 FeS_m nucleus m $^{-3}$ s $^{-1}$ which suggests a critical

supersaturation of 1.08, equivalent to Fe(II) = (S–II) aqueous concentrations of about 1.5 mM for $\gamma \gtrsim 0.02$ J m⁻².

The experimentally derived values for the nucleation rate of FeS_m from aqueous solutions at STP are consistent with observations. The results show that the rate of nucleation rapidly increases to values greater that $10^{20}~FeS_m$ nuclei $m^{-3}~s^{-1}$ as the solution concentrations of Fe(II) and S(-II) exceed the solubility product for FeS_m at low millimolar dissolved Fe(II) and S(-II) concentrations. The result also suggests that the surface energy of nanoparticulate FeS_m nuclei is far less than the computed Wulff shape mean value of 0.15 J m^{-2} but similar to DFT calculations of the surface energy of the dominant (001) face (Table 15).

The effect of the surface energy contribution to the value of the Gibbs free energy of formation, ΔG°_{f} (FeS_m), for FeS_m particles of various sizes can be estimated from the experimental data. The ΔG°_{f} (FeS_m) value of -97.44 ± 1 kJ mol $^{-1}$ (section 6.1) is determined from solubility measurements of colloid-sized, if not nanoparticle size, FeS_m particles. The specific surface area for the smallest observed FeS_m particles is 579 m² g $^{-1}$ (Table 17) or 5 × 10⁴ m² mol $^{-1}$. A surface energy of 0.02 J m $^{-2}$ is then equivalent to 1 kJ mol $^{-1}$ which is within the uncertainty in the standard free energy of formation. As the particle size increases the SSA decreases and the relative contribution of γ to ΔG°_{f} (FeS_m) decreases. These estimates suggest that, for FeS_m particles, the relative contribution of the surface energy to the total free energy is approximately constant and within the uncertainties in the reported total free energy values.

This conclusion does not conflict with the results of DFT computations which suggest that the surface energy contribution for nanoparticulate FeS_{m} is much lower than the computed values for both nanoparticulate $\text{Fe}_{3}\text{S}_{4g}$ (greigite) and nanoparticulate FeS_{2p} (pyrite). 161 The relative differences in the computed values are such that, even with the large uncertainties in the computed values, it appears that FeS_{m} nuclei are stable relative to FeS_{2p} and $\text{Fe}_{3}\text{S}_{4g}$ nuclei. This provides an alternative approach to explaining the observed preferential nucleation of FeS_{m} in aqueous solutions and links the thermodynamics with kinetic (i.e., mechanistic) data.

6.3. Thermal Stability

There are conflicting reports on the apparent thermal stability of FeS_m . FeS_m is a metastable phase in the Fe-S system and therefore changes irreversibly to more stable phases at all temperatures. The thermal stability of FeS_m then refers to the rate of equilibration which depends on kinetic factors such as the rate of temperature change, the presence or absence of water or a vapor phase or the particle size.

Reports of the thermal stabilities of natural mackinawites and synthetic FeS_{m} are listed in Table 16. The thermal stability of this metastable material is kinetically controlled and the reported stability temperatures reflect both the nature of the material and the method of measurement. A major complication is the facile transformation of FeS_{m} to stable $\text{Fe}_{3}\text{S}_{4g}$ (section 10.2), even under experimental vacuum, as well as the more conventional equilibration to pyrrhotite.

Natural mackinawites appear to transform to stable pyrrhotite at \leq 413K (140 °C) depending on the Ni and Co contents. ^{173,174,176,179} The natural material occurs as microscopic exsolution-like bodies enclosed in other sulfides and the contribution of sulfur from the surrounding sulfide minerals affects the thermal stability. ¹³⁴ The most direct measurement referred to observed changes to pyrrhotite in the reflected light

Table 16. Reports of Thermal Stability (Temperature K and $^{\circ}$ C) of Mackinawite and FeS_m^a

,		***		
K	°C	material	comments	ref
≤413	140	mackinawite	varies with Ni and Co contents	173-175
423-443	150-170	FeS_m	transformation to pyrrhotite	36
393-426	120-153	mackinawite	S addition from enclosing minerals	176
518	245	mackinawite	DTA: unspecified phase transformation	17
483	210	mackinawite	transformation to pyrrhotite	17
493-498	220-225	mackinawite	transformation to pyrrhotite	177
530-545	257-272	FeS_m	transformation to hexagonal pyrrhotite	178
453	180	FeS_m	TGA: transformation to greigite	12

"DTA = differential thermal analysis; TGA = thermal gravimetric analysis.

microscope on heating samples under vacuum. These experiments gave similar results. 17,177 However, a small thermal peak on the same material gave a divergent reading.¹⁷ The peaks observed in differential thermal analysis (DTA) were not, however, related to any specific transformation 12,17 although the TGA peak at 180 °C was due to the transformation to Fe₃S_{4g}. The kinetics of the transformation of synthetic FeS_m to hexagonal pyrrhotite were orginally reported by Lennie et al (1995).¹⁷⁸ The mechanism is solid state diffusion and is rapid >523 K (250 °C) and FeS $_{\rm m}$ may persist <453 K (180 °C). Transformations of wet FeS_m to hexagonal pyrrhotite have also been reported after 12 h at 423 K (150 °C). Thermal studies of large single crystals of FeS_m broadly confirm these results with FeS_m beginning to decompose at 100 °C, being transformed to Fe_3S_{4g} completely at 200 °C and hexagonal $Fe_{1-x}S_{po}$ being formed above 300 °C.³¹ The conclusion of all these studies is that FeS_m is unlikely to persist for substantial periods of time much above ~200 °C. As mentioned above, the process is equilibration of metastable to stable assemblages and the rate of FeS_m change at any temperature is dependent on kinetic factors.

The original descriptions of mackinawite 17,18 were from sulfide ores associated with high temperature (i.e., $T > 1400 \,^{\circ}\text{C}$) magmatic intrusions. These ores belong to a class of deposits which include some of the world's largest mineral deposits. Since the original reports, mackinawite has been widely reported from these ores worldwide. It is associated with characteristic pyrrhotite-pentlandite-chalcopyrite assemblages. These assemblages formed from the cooling and crystallization of magma-derived sulfide mattes, consisting predominantly of Fe, Ni, Cu and S, which fractionate to form a sequence of phases on cooling. 180 Below 1100 °C, a (Ni,Fe)S monosulfide solid solution (MSS) crystallizes to leave a Cu-rich sulfide liquid. At ~900 °C, an intermediate solid solution (with a composition approximating CuFeS2) crystallizes out. On further cooling to below ~700 °C, the MSS breaks down to pyrrhotite and pentlandite and the intermediate solid solution generates chalcopyrite.

The occurrence of low temperature, metastable mackinawite within these high temperature assemblages remains somewhat

of a mystery. The mineral commonly appears as apparent exsolution intergrowths within the massive sulfides and these have been interpreted as due to exsolution and replacement textures. 181-183 It seems obvious that it is unlikely that the unstable mineral mackinawite formed by an equilibration process like exsolution. It is more likely that it is formed by replacement of a pre-existing phase that has exsolved during cooling of the high temperature sulfide solid solutions. Indeed in the type deposit in the Mackinaw Mine in Washington, the mineral is associated with late stage processes.¹⁸ It seems probable that the mackinawites associated with this high temperature assemblage formed mainly through the reaction between late stage lower temperate sulfide solutions with Fe-rich alloys which had exsolved from the sulfides on cooling. 184,3 There is abundant evidence for mackinawite formation through replacement in these ores including a cohort of mackinawites forming in fractures and cleavages and at grain boundaries in the sulfide minerals. They commonly form from cracks and grain boundaries and are consistent with the late-stage, low temperature, hydrothermal processes which cool these igneous bodies to ambient temperatures. Mackinawite occurring in late-stage lower temperature deep sea hydrothermal vents has been implicated in the origin of life.18

Some support for the conclusion that mackinawites associated with high temperature magmatic ores were formed from late-stage lower temperature hydrothermal processes is provided by the occurrence of mackinawite, associated with greigite and smythite, in the Moschellandsberg mercury deposit in SW Germany. ¹⁸⁷ In this deposit, mackinawite was formed at temperatures between about 50 and 200 °C.

6.4. Pressure Stability

 ${\rm FeS_m}$ shows an irreversible first-order structural phase transition to an orthorhombic FeS phase at around 3 GPa. 128 The orthorhombic phase has been designated FeS-II, 188 which is also derived from ${\rm FeS_v}$ stoichiometric FeS with the hexagonal troilite structure, at high pressure. FeS-II has a space group Pnma with lattice parameters a=5.77449, b=3.3782 and c=5.8048. FeS-II transforms to a series of six further FeS polytypes with increasing pressure. $^{189-191}$ The implication of these pressure data is that ${\rm FeS_m}$ will not transform to FeS-II in the Earth oceans and may be retained at rock burial depths < 100km.

7. KINETICS AND MECHANISM OF FORMATION OF FeS_m

7.1. Rate of Nucleation of FeS_m

The observed rate of nucleation of $\mathrm{FeS}_{\mathrm{m}}$ in aqueous solutions at STP is rapid and experimentally appears to be limited by transport factors, such as mixing and diffusion.

The original experimental observations 192 on the kinetics and mechanism can be reinterpreted in terms of the rate of removal of S(-II) from aqueous solution being a measure of the rate of nucleation of FeS_m .

$$-dS/dt = k_1 c_S \tag{6}$$

The rate of decrease in the total aqueous sulfide concentration due to FeS_m precipitation dS/dt mol L^{-1} s⁻¹ is directly proportional to the sulfide concentration, c_S mol L^{-1} (eq 6). ¹⁹² The pseudo first order rate constant, k_1 , is 48 ± 9 s⁻¹. The rate was originally written in terms of the dissolved sulfide concentration. However, later reports showed that the Fe:S ratio of the nucleated FeS_m approaches unity, ¹² so that the moles of sulfide removed closely approximate the moles of Fe removed

and the rate can be written in terms of the rate of formation (i.e., nucleation) of FeS_m .

If it is assumed that the measured rate of removal of aqueous Fe(II) and S(-II) from solution approximates the rate of FeS $_{\rm m}$ formation, then the experimentally observed rate of FeS $_{\rm m}$ formation, then the experimentally observed rate of FeS $_{\rm m}$ formation 192 is about 10 mol FeS $_{\rm m}$ s $^{-1}$ which is a measure of the rate of nucleation of FeS $_{\rm m}$ from aqueous solution at STP. Assuming that the minimum supersaturation required to precipitate FeS $_{\rm m}$ from aqueous solution at STP approaches 2, this equates to aqueous concentrations of Fe(II) = S(-II) = 2 mM, which is consistent with experimental observations. If the smallest observed particle is similar to the FeS $_{\rm m}$ nuclei then these nuclei are cuboid in shape with dimensions 2 nm \times 3 nm \times 3 nm, a volume of 18 nm 3 and a mass of 71.4 \times 10 $^{-21}$ g at a computed FeS $_{\rm m}$ density of 4.3 g cm $^{-3}$. This suggests a nucleation rate of 1.137 \times 10 21 cuboid FeS $_{\rm m}$ nuclei m $^{-3}$ s $^{-1}$ at millimolar concentrations of dissolved Fe (II) and S(-II).

Most experimentation is performed at millimolar concentrations and above in batch reactors in order to obtain sufficient amounts of product for analysis. The effect is that FeS_m appears to precipitate immediately: e.g. it takes $\sim\!0.1$ ms for the dissolved Fe(II) and S(-II) to be removed from solution assuming instantaneous mixing.

7.2. Mechanism of Formation of ${\sf FeS_m}$ from Aqueous Solution

A synthesis of current information on the mechanism of FeS_m formation from aqueous solution is shown in Figure 7. The rate

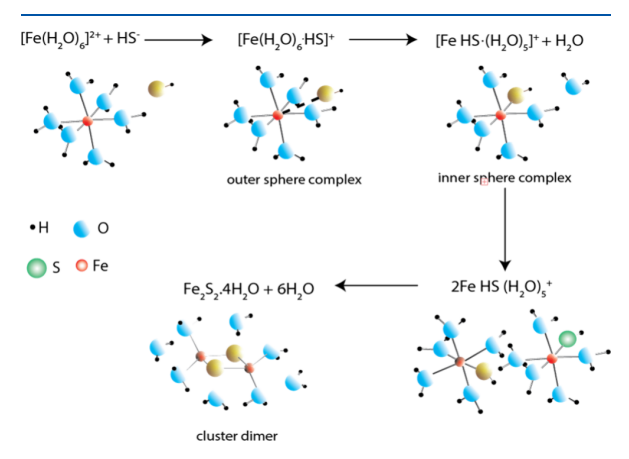


Figure 7. Mechanism of FeS_m formation from aqueous solution. Classical Eigen—Wilkins kinetics leads to the formation of outer sphere $[Fe(H_2O)_6 \cdot HS]^+$ and inner sphere $[FeHS \cdot (H_2O)_5]^+$ complexes. The inner sphere complexes associate to produce aqueous FeS dimer clusters which have the same form as the basic moiety in FeS_m .

laws for the reactions between aqueous Fe^{2+} and HS^- and Fe^{2+} and H_2S are both consistent with Eigen–Wilkins mechanisms 192,193 The rates are determined by the rate of exchange between water molecules in hexaqua iron (II) sulfide outer sphere complexes, $[Fe(H_2O)_6^{2+}\cdot H_2S]$ and $[Fe(H_2O)_6^{2+}\cdot HS^-]$, and inner sphere complexes $[FeH_2S\cdot (H_2O)_5]^{2+}$ and $[FeSH\cdot (H_2O)_5]^{-1}$.

Since this original work, aqueous FeS clusters have been shown to play a key role in FeS_m formation and form as a consequence of the substitution reactions. $^{20,194-196}$ FeS clusters are well-known in biochemistry where they constitute the oldest biological cofactors and FeS proteins, such as ferredoxin, are key compounds in biologic electron transfer processes. At least 3659

papers were published on FeS clusters in biology between 1920 and 2020. 111 The literature on aqueous FeS clusters, where FeS molecules are ligated directly to H₂O molecules, is more limited. They were first described in 1988 from lake waters and their chemistry has been reviewed just a few times. 20,195,197-199 However, there has been a recent upsurge in interest in these clusters because of their use in biomimetic templates, sustainable batteries and catalysts. ²⁰⁰ A series of reports have described the results of molecular computational analyses of these compounds. These have evolved from electronic structure and geometry of the clusters in the gas phase, through detailing their structural properties utilizing nonreactive interatomic potentials to probing the dynamic nature of these clusters in an aqueous environment. 200 These studies confirmed that the most stable geometry of the smallest FeS_{aq} cluster below 400K is $Fe_2S_2(H_2O)_4$. The detailed compositions of the larger aqueous FeS clusters are unresolved as yet, although Fe₄S₄ has been reported also to be ligated to 4 H₂O molecules.²⁰ The biologic FeS clusters display flexible assemblies with varying Fe^{II} and Fe^{III} contents and Fe:S ratios.²⁰

Nucleation of FeS_m from solution occurs as the clusters reach a critical size which is $\leq \sim 150$ FeS molecular units based on the observed smallest sized FeS_m particles. ^{19–21,203}

The nucleation of FeS_m from aqueous FeS clusters is facile since the fundamental FeS moieties in each form are similar (Figure 8).⁷³ As discussed in section 6.2, this can alternatively be

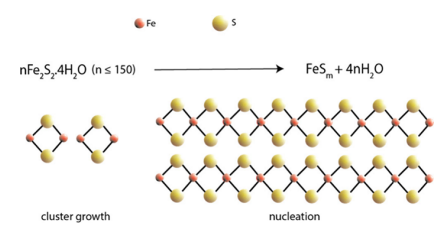


Figure 8. Homology between aqueous FeS clusters and the FeS_m structure, projected on to a plane perpendicular to the c-axis without H_2O . Adapted with permission from ref 255. Copyright 2005 Elsevier.

described in terms of the large DFT-calculated surface area free energy contribution to the Gibbs energy of formation of nanoparticulate ${\sf FeS_m}$.

Figure 8 is a projection of all the atoms onto a plane perpendicular to the c-axis and effectively parallel to mackinawite 001. Reference to the three-dimensional view of the mackinawite structure (Figure 1) shows that the S atoms in Figure 8 are alternatively above and below this plane maintaining the tetrahedral symmetry. The whole process is accompanied by entropy gain as H_2O is eliminated.⁷³

The aqueous FeS cluster size is greater than the size of the first observed particle and this caused some consternation among the original investigators²⁰⁴ although they correctly interpreted the data as reflecting a process where nucleation of the solid phase involves a density discontinuity.

More recent studies of similar systems show that nucleation from solution may proceed through a two-step process involving the initial formation of clusters and nucleation of the solid phase within the cluster (Figure 9). This process has been called nonclassical nucleation and has been widely reviewed. 205,206 The thesis that FeS $_{\rm m}$ nucleation from solution proceeds through aqueous FeS clusters explains the observation that the first-formed FeS $_{\rm m}$ particles are electroactive and they are

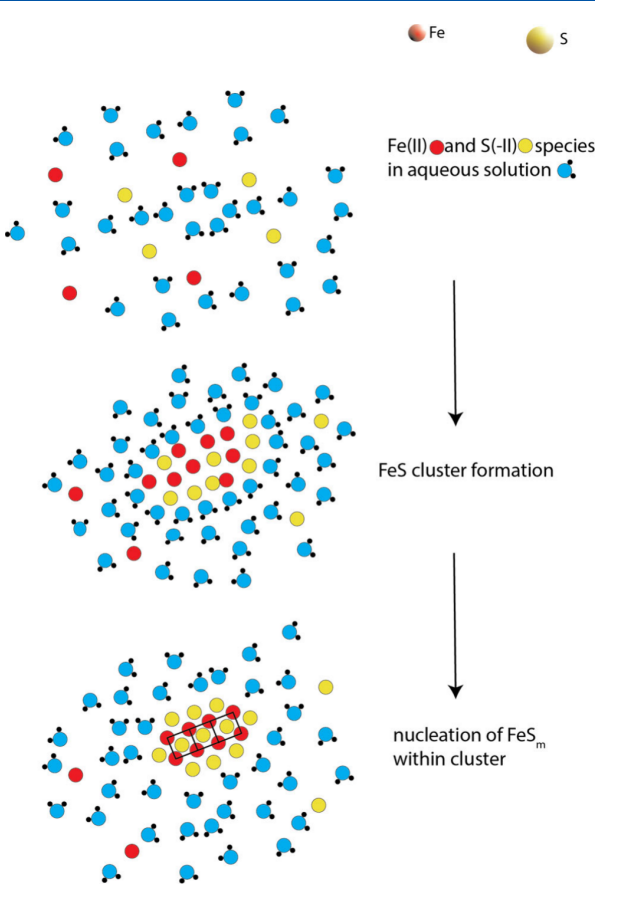


Figure 9. Illustration of the steps in FeS_m nucleation from aqueous solution. Aqueous Fe (II) and S(II-) species in aqueous solution react to form FeS clusters in which FeS_m nucleates.

indistinguishable from the aqueous FeS clusters at electrode surfaces. 198 The Fe–Fe distance in bulk mackinawite is 0.256 nm which is close to that of α -iron (0.248 nm) and results in strong Fe–Fe bonding. The nucleation of FeS $_{\rm m}$ involves the formation of extensive Fe–Fe bonds and the development of a planar Fe lattice analogous to that of α -iron. The calculated Fe–Fe distance in the Fe₂S₂·4H₂O cluster complex is 0.283 nm whereas that estimated for the 2 nm mackinawite phase is about 0.28 nm. This process is accompanied by an increase in density from the density of the aqueous cluster (\rightarrow 1 g cm $^{-3}$) to that of the FeS $_{\rm m}$ solid (\rightarrow 4.3 g cm $^{-3}$).

As described in section 2, since the first report of a less well-defined variant of FeS $_{\rm m}$ which appears in the earliest FeS precipitates but transforms to the more conventional form with time, 21 the number of FeS $_{\rm m}$ variants is not limited to 2. Rather there exists a variety of FeS $_{\rm m}$ particles with different interlayer spacings. 30 In the charged-layers model, these particles contain varying combinations of uncharged and charged layers which transform over time to standard, uncharged FeS $_{\rm m}$. The diffractogram shown in Figure 2 was collected from an FeS $_{\rm m}$ precipitate aged for 7 days in aqueous solution at 80 °C and is interpreted as showing both the developing crystallinity of the material and the increased dominance of the uncharged standard FeS $_{\rm m}$.

7.3. Mechanism of Formation of FeS_m from α -Iron

The formation of $\mathrm{FeS_m}$ from the reaction between aqueous sulfide and α -iron has been widely studied because it is a key reaction in the sulfide corrosion of iron, mainly in pipes in the hydrocarbon industry but also in the construction industry. It has also been widely used experimentally to synthesize larger $\mathrm{FeS_m}$ crystals. Earlier work on the sulfidation process generally described an anodic mechanism where $\mathrm{H_2S}$ diffuses into the steel surface where it reacts with the Fe to form $\mathrm{FeS_m}$. The $\mathrm{FeS_m}$ then dissolves to $\mathrm{Fe}(\mathrm{HS})^+$ and HS^- and $\mathrm{Fe}(\mathrm{HS})^+$ diffuse away from the metal surface. $\mathrm{^{207}}$ The problem with this idea was that the activation energy for the reaction is negligible and far below even the activation energy for diffusion. $\mathrm{^{32}}$

The mechanism involves an epitactic reaction between α -iron and sulfide. ³² Although the Fe–Fe distance in α -iron (2.866 A) is similar to that of the Fe–Fe (2.597 A) in the square planar sheets that define the FeS_m structure, the small difference is important in determining the mechanism and the rate of sulfidation of α -iron.

A key parameter for determining the rate of sulfidation of α -iron is spalling of the $\mathrm{FeS_m}$ to expose new surfaces of α -iron. The small differences between the Fe–Fe lattice dimensions in the two materials lead to strains between the two structures. The accumulated strain produced by the contraction of Fe–Fe distances when S attaches to the Fe surface leads to curling of the S layer away from the bulk Fe (Figure 10A) and detachment of

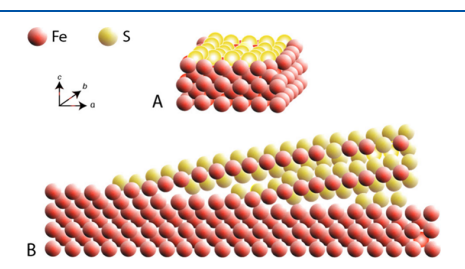


Figure 10. (A) Molecular mechanics simulation of S reaction with α -iron, showing the development of curvature in the S layer and the contraction in the surface layer of α -iron. (B) Continued reaction of S with the surface of α -iron leads to detachment of the FeS layers and the exposure of fresh surfaces for reaction. Adapted with permission from ref 32. Copyright 2024 Elsevier.

the FeS_m layer (Figure 10B), exposing new Fe surfaces for reaction. The dependence of the reaction rate on the mechanical process of spallation leads to the negligible activation energy for the reaction.³² Crystallization of the FeS_m continues via translational stacking (section 9.2.2).

An older variant of the sulfide reaction with iron is the reaction between elemental sulfur and iron in damp or wet conditions which produces FeS_m at room temperature. 30 The mechanism of the reaction involves sulfur disproportionation to sulfide and sulfate followed by reaction between Fe^{2+} released through acidification of the Fe and the S(–II) product of the disproportionation reaction to precipitate FeS_m from solution. $^{208-210}$ An electrically conducting layer is produced between the initial FeS precipitate and the iron surface. Dissolution of the Fe releases Fe^{2+} and electrons move through the FeS and react with surface S molecules to produce polysulfides. 210,211 These react with the diffusing Fe^{2+} ions to produce FeS_m . In this model, the growth of the FeS_m area only continues at the edges of the original FeS precipitate. 30,210,211 By contrast with the epitactic reaction, this process produces fine-

grained nanoparticulate FeS_m , typical of nucleation and restricted particle growth in precipitation from aqueous solution.³⁰ The reaction is characterized by a long induction period²⁰⁹ which is thought to reflect the initial sulfur disproportionation reaction.³⁰

8. PARTICLE GROWTH OF FeS_m

The particle size of FeS_m precipitated from aqueous solutions has been the subject of many investigations and has been more accurately determined as technology has improved. The original size of FeS_m particles can be defined as the size of critical nuclei, the size limit at which a nucleus is likely to grow rather than dissolve.

8.1. Critical Radius of FeS_m Nuclei

In classical nucleation theory (CNT), the critical radius, r^* (m), of a spheroidal nucleus forming homogenously can be estimated via equation 7 where R is the universal gas constant (8.3147 J K⁻¹ mol⁻¹), γ is the surface energy (J m⁻²), $\nu_{\rm m}$ is the molecular volume (m³ molecule ⁻¹), T is the temperature (K), and Ω is the supersaturation, defined as the ratio of the ion activity product (IAP) to the solubility product, $K_{\rm sp}$.

$$r^* = 4\gamma \nu_{\rm m}/RT \ln \Omega \tag{7}$$

Figure 11 shows solutions for equation 7 for surface energies of 0.02 and 0.15 J mol⁻¹ for FeS_m, $K_{\rm sp}=10^{-5.7}.^{153}$ At the

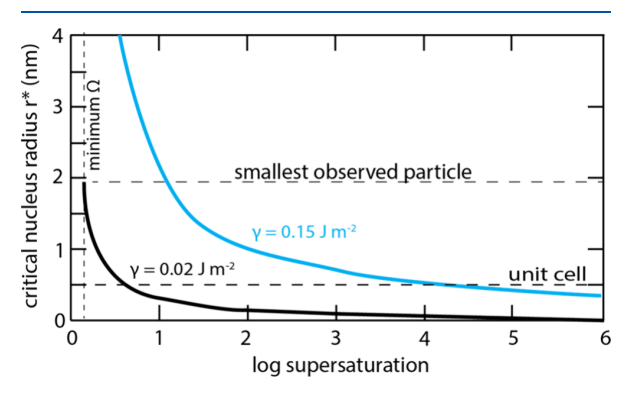


Figure 11. Critical radius, r^* , (nm) for FeS_m nucleation from aqueous solution at STP versus log supersaturation computed according to equation 7. The smallest observed FeS_m particle size and the largest unit cell dimension are indicated. Curves are shown for surface energies γ = 0.02 and 0.15 J m⁻².

minimum $\Omega \to 1.08$ (section 6.2), IAP = 2×10^{-6} and the concentration of aqueous Fe(II) = the concentration of S(-II) ~ 1.5 mM. The minimum value of r^* is 0.5 nm or approximately equal to the maximum unit cell dimension of FeS_m: by definition, if the particle size is smaller than the unit cell, the material can no longer be described as FeS_m. Figure 11 shows that at a minimum surface energy of 0.02 J m⁻², the critical radius of the FeS_m nucleus only exceeds the unit cell size at Ω values approaching 4 (log Ω = 0.6), equivalent to solutions with Fe(II) and S(-II) concentrations around 3 mM. For particles with γ = 0.15 J m⁻², the limiting supersaturation for FeS_m nucleation is about 100, equivalent to solutions with Fe(II) and S(-II) concentrations around 15 mM. This concentration is at least one magnitude higher than the concentrations observed experimentally and confirms that the surface energy of the FeS_m nucleus cannot be as high as 0.15 J m⁻².

The number of FeS molecules contained in an FeS nucleus is inversely proportional to the supersaturation and varies between $<\!2$ to $>\!1200$ as the supersaturation increases from 1 through 10^6 (Figure 11). The smallest observed FeS $_{\rm m}$ particle contains around 150 FeS units and this limits the maximum size of aqueous FeS clusters. 20,73

8.2. Particle Size

Investigations of the size and crystallographic structure of the initial FeS_m precipitates are limited by simple practical considerations. The initial precipitation from aqueous solution is effectively instantaneous ²¹² and subsequent particle growth can be stopped by freeze-drying the sample. However, most samples analyzed are at least 20 min old 153 since it takes this length of time to pump down the machine, apart from the time taken for filtration or other methods of particle concentration. A work-round has used X-ray adsorption near edge structure spectroscopy (XANES) and extended X-ray adsorption fine structure spectroscopy (EXAFS) to probe continuous flow and stopped-flow systems. 213 This investigation probed the precipitate at less than 10 ms age. The Fe K edge XANES was consistent with tetrahedrally coordinated Fe; EXAFS showed Fe-S distance = 2.24Å and Fe-Fe = 2.57Å which compares with the interatomic distances obtained from Rietveld refinement of the crystal structure of well-crystalline FeS_m (Fe-S = 2.2558 Å and Fe-Fe = 2.5976 Å).²³

The classical method to determine particle size is the Scherrer approach to conventional Braggian X-ray powder diffraction (XRPD) spectra. The Bragg theory assumes the presence of an infinite periodic lattice which is a good approximation for large crystalline solids.

The classic X-ray powder diffraction (XRPD) trace for precipitated FeS_m is shown in Figure 12a. It is typified by a broad

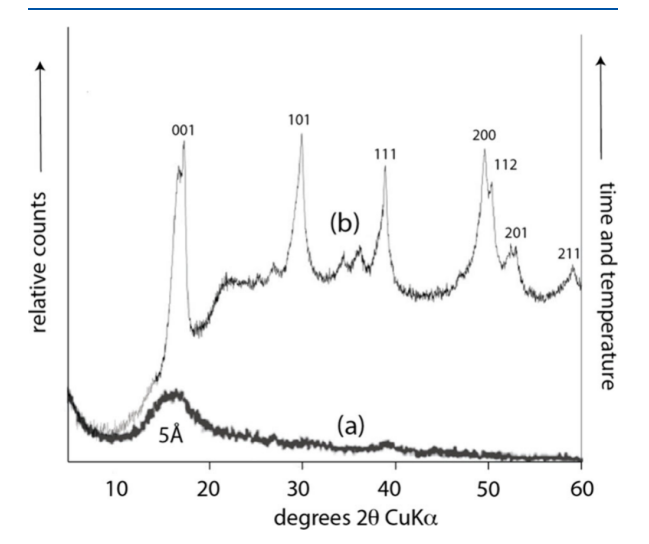


Figure 12. XRPD scans of (a) precipitated FeS showing typical broad peak at around 5 Å and (b) aged FeS_m showing Laue indices (modified from Figure 2).

peak around SÅ. The lack of further XRD peaks was originally interpreted as due to the amorphous nature of the precipitate. ^{109,143,214} The nanoparticulate nature of precipitated FeS was first demonstrated by XRPD analyses ²¹ and subsequently confirmed by high resolution electron microscopy. ¹⁹ Low angle X-ray diffraction spectra of precipitated FeS

was originally deconvoluted into two phases with distinct characteristics: a 2 nm phase with a tetragonal unit cell size of 6.6 Å \times 4 Å and a 5.4 nm phase with a unit cell of 5.5 Å \times 3.7 Å. 21 The size of the smallest particle was computed to be 2.2 nm \times 2.2 nm \times 1.7 nm which is consistent with neutron diffraction data 203 and pair distribution function analyses of high energy XRD data. 116 With time, the proportion of the smaller particles with the larger unit cell decreases. These results were confirmed by HRTEM which showed individual laminar rectilinear prisms, ranging from 2 to 5.7 nm in thickness with the smallest being approximately 2 nm \times 2 nm \times 2 nm \times 2 nm. 19

These particles contain about 75 $\rm FeS_m$ unit cells equating to around 150 FeS moieties. ²¹ It seems improbable that 75 unit cells can be modeled as an infinite periodic lattice with the Bragg interpretation and, consequently, the Scherrer equation should break down. In fact, this is not the case and application of the Scherrer equation to $\rm FeS_m$ XRPD patterns predicted similar particle sizes to those observed in HRTEM²¹ and computed by PDF analysis of high energy XRD data. ¹¹⁶ The solution to the conflicting data came through serendipity (section 8.3).

The variation in reported particle sizes (Table 17) reflects both the preparation and measurement methods.²⁹ Particle size

Table 17. Measured Specific Surface Areas (SSA) for FeS_m Precipitate Particles in Aqueous Solution^a

SSA $(m^2 g^{-1})$	size (nm)	method	ref
44	33	light microscopy	159
7	210	BET	215
53 ± 46	15-220	BET	71
16-21	70-90	BET	161
80	18	BET	216
40 -80	<30	BET	30
47 ± 1	31	BET	130
424 ± 120	4	EGME	29
220	8	XRPD	29
350	4	LAXRPD	130
40-140	10-35	XRPD+SEM	144,217
4-73	20-400	TEM	218
103	22	TEM	29
579	2	HRTEM	19
186	11	HRTEM	19
531	3	HRTEM	29
210	11	HRTEM	29

"Size is the maximum dimension of the observed particles. Method abbreviations: BET, gas adsorption measurements using the Brunauer–Emmet–Teller theory; XRPD, X-ray powder diffraction; SEM, scanning electron microscopy; LAXRPD, low angle X-ray powder diffraction; HRTEM, high resolution transmission electron microscopy; EGME, ethylene glycolmonoethyl uptake.

is a general and unspecific term for platelike or irregular shapes. In Table 17 only the maximum reported dimension is listed. As can be seen, reported particle sizes for FeS_m vary between 2 and 400 nm or over 2 orders of magnitude. The measured specific surface area (SSA) for FeS_m is then also highly variable and the reported SSA values range over 2 orders of magnitude (Table 17). This depends on the manner of preparation of the sample but also on the measurement method. As discussed above, the variation in reported SSA values leads to significant uncertainty in the surface energy estimates for FeS_m particles.

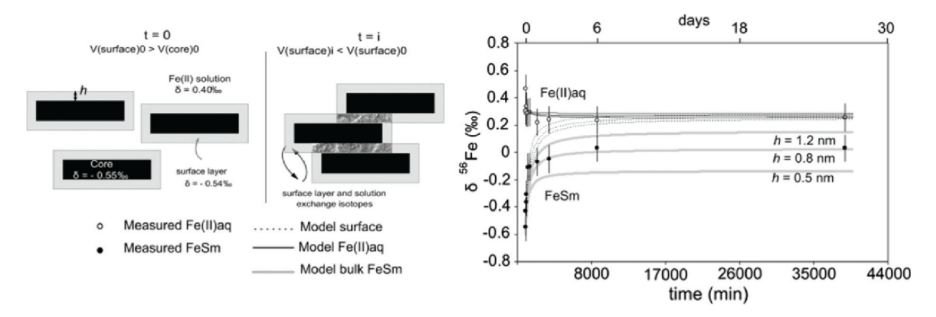


Figure 13. Fe isotopic exchange between the mackinawite surface layer and the solution, assuming a constant surface layer thickness, *h* nm, and a nonexchanging core. Adapted with permission from ref 219. Copyright 2010 Elsevier.

8.3. Particle Growth

The growth of FeS_m particles mainly occurs through oriented attachment (OA), sometimes referred to as aggregation growth. This suggests a two-stage process where the initial stage is Ostwald-type dissolution-precipitation in which the growth occurs by monomer attachment. This produces the original nanoplates which then grow mainly by oriented attachment.²²⁰ Since this pioneering work, the physics, chemistry and mathematics of OA have received considerable attention because of its importance to particle growth in semiconductors, metals, silicates, oxides, and organic compounds²²¹ but there have been no further mathematical descriptions of OA of FeS_m nanoparticles. Data collected by Guilbard et al. 219 show that the second stage of crystal growth of FeS_m in aqueous solution fits closely with a simplified mathematical oriented attachment model. 220 By contrast, data fitting algorithms for Ostwald-type processes require physically unreasonable parameters²²² which suggest that Ostwald growth is not responsible for the whole of the particle growth process for FeS_m.

This was confirmed by examining the fractionation in Fe isotopes between the $\text{FeS}_{\rm m}$ precipitate and solution. 219

The original reactant Fe solution contained a natural mass distribution of ⁵⁴Fe, ⁵⁶Fe and ⁵⁷Fe. In a closed system the ⁵⁶Fe/⁵⁴Fe and ⁵⁷Fe/⁵⁴Fe ratios of the whole system, Fe in the FeS_m precipitate plus solution Fe, is constant. Precipitation of FeS_m leads to a relative depletion of ⁵⁶Fe in the FeS_m and a consequent relative enrichment of ⁵⁶Fe in the solution. ²¹⁹ The competing processes of crystal growth, Ostwald-ripening and OA, produce different effects on the ⁵⁶Fe/⁵⁴Fe and ⁵⁷Fe/⁵⁴Fe ratios of the precipitates and solutions over time. Ostwald ripening involves the total dissolution of smaller ⁵⁶Fe-enriched FeS_m particles and reprecipitation of larger FeS particles. Oriented attachment proceeds by oriented attachment of FeS_m platelets: Fe isotope exchange between the particle and solution during crystal growth is then limited to a surface reaction zone.

The rate of iron isotopic exchange during the experiment is directly proportional to the mackinawite crystal size during crystal growth. This is not consistent with a conventional Ostwald-ripening mechanism of crystal growth but is described, with precision, by an oriented attachment mechanism (Figure 13). The model estimates that the thickness of the surface phase on the nanoparticles of 0.8 nm which constitutes a substantial fraction of these nanoparticles which, as described above, may originally be only 2 nm thick. These results are consistent with earlier conclusions based on HRTEM analyses ¹⁹ and pair distribution function analysis ¹¹⁶ which showed that the majority

of FeS pairs in this material were in edge and surface positions. Since FeS_m is anhydrous, this surface phase is disordered rather than hydrated — which is consistent with the earlier XRPD analyses of disordered synthetic mackinawite. The result was independently confirmed by Lai et al 52 who prepared FeS_m microsheets and showed that these were aggregates of smaller well-defined single crystal nanoplates (Figure 14).

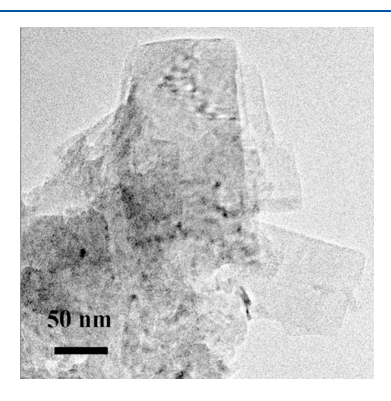


Figure 14. Transmission electron micrograph image of relatively large FeS_{m} nanoplates synthesized by Lai et al. ⁵² showing aggregation growth. Reproduced with permission from ref 52. Copyright 2015 American Chemical Society.

The rapid aggregation of ${\rm FeS_m}$ nanoparticles has important practical and theoretical consequences. On the practical side, aggregation means that ${\rm FeS_m}$ precipitates from aqueous solution are readily filtrable. Although individual nanoparticles down to 2nm in size are challenging to mechanically separate for analysis, the larger clumps particles are readily filtrable with the simplest of systems. 153

Drying, whether at ambient temperature or freeze-drying, increases the tendency of the ${\rm FeS_m}$ nanoplates to clump together. The product ${\rm FeS_m}$ can be observed in low resolution SEMs and appears as large flakes or flame-like particles (Figure 15).

Several studies have compared the growth rates of FeS_m nanoparticles formed by standard processes with those synthesized with additives such as trace metals and microorganisms. The particle growth rate is accelerated by aqueous Ni(II). In the presence of Ni, the computed coordination numbers for Fe in FeS_m determined by Fe K-edge EXAFS are significantly higher. 140 The increase in the numbers of Fe neighbors in FeS_m is related to the development of the square-planar arrays of Fe atoms in the crystalline mackinawite structure

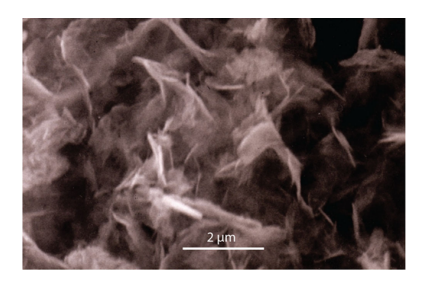


Figure 15. SEM image of flame-like aggregates of FeS_{m} nanoparticles formed after drying.

(see section 7.2). 223 The rates of particle growth and crystallization of FeS_m are also reported to markedly increase in the presence of microorganisms, 223 suggesting that biologic surfaces might catalyze these processes. 224 (see section 12.5).

The reasons for the increase in particle growth in the presence of Ni remains uncertain. There is a possibility that the presence of Ni (and other transition metals) in the mackinawite structure increase its entropy and thus its thermodynamic stability 38 although this has not been quantified. Whether this increased stability would be sufficient to significantly increase the already extremely rapid homogeneous nucleation rate of FeS_m (section 7.1) seems unlikely.

9. CRYSTALLIZATION OF FeS_m

The second key process observed during "aging" of FeS_m precipitates is increased crystallinity. The FeS_m precipitate is still sometimes described as *amorphous* FeS_m^{36} (see section 1.1) because it gives no clear reflections on conventional XRPD analyses (Figure 12a) and SAED patterns show only short-range ordering. With time and/or increased temperature the XRPD scan develops the characteristic peaks of crystalline mackinawite (Figure 12b). However, oxidation of the precipitate to Fe_3S_4 is also reported accompanying this increased crystallinity.³⁶

Long-range ordering in precipitated FeS_m develops within 1 h¹⁴³ if precipitated directly from aqueous solution, 1 s¹¹³ if formed on an α -Fe substrate² or within 2h if heated to 120 °C. ³⁶ Electron diffraction shows that the smallest particles often show a lack of distinct d_{110} , d_{210} and d_{003} reflections and a significant decrease in intensity of the d_{111} reflection. ¹⁹ EXAFS analyses of 1 s old FeS precipitates showed that the local atomic environment is similar to that of well-crystalline FeS_m (Table 18).

Table 18. Refinements of Fe K-Edge EXAFS Spectra for Quenched FeS Precipitates Compared with Well-Crystalline ${\rm FeS_m}~({\rm Bold})^{113a}$

	r (Å)		N	
age (s)	shell 1 (S)	shell 2 (Fe)	S	Fe
1	2.24	2.59	3.8	2.0
5	2.22	2.57	3.8	2.8
10	2.26		3.0	
20	2.25		3.4	
60	2.20	2.59	3.9	3.5
300	2.23	2.68	4.0	2.5
1800	2.21	2.62	4.0	2.8
FeS_m	2.26	2.56	4.0	4.0

^aAge = liquid N₂ quench time after reaction (seconds). r radial distance of fitted shell from central Fe atom (Å); N, coordination number.

Pair distribution analysis of high energy XRD data (Table 18) revealed that the structural parameters of freshly precipitated FeS (8 h old) are similar to those of well-crystalline FeS_m. ¹¹⁶ The effect of crystallization is thus to extend the range of ordering from ~ 1 nm to the effective infinite Braggian ordering of bulk well-crystalline FeS_m. That is freshly precipitated FeS_m is not truly amorphous.

9.1. Crystal Shape

 FeS_m crystals commonly develop thin tabular habits (Figure 16), often colloquially referred to as quasi two-dimensional crystals, with extreme development of the $\{001\}$ leading to the characteristic XRPD pattern (Figure 2).



Figure 16. Wulff shape for FeS_m crystals based on differential computed surface energies of FeS_m surfaces. Adapted with permission from ref 225. Copyright 2008 American Chemical Society.

The observed development of crystals of FeS_m is consistent with computed surface energies of individual FeS_m surfaces. As shown in Table 16, computed surface energies for the (001) surface are far lower than other FeS_m surfaces. Crystal growth is more rapid perpendicular to the plate edge planes such as (101), (100) and (111) than perpendicular to the highly stable, low energy, (001) surface which produces the typical FeS_m nanoplates.

The formation of larger FeS_m crystals on α -Fe is due to epitaxial growth of FeS_m on a structurally homologous substrate. This process is important industrially in the sulfide corrosion of iron and has become significant in materials science since the reaction has been the preferred route for the synthesis of the FeS_m crystals used in electrical and magnetic studies.

9.2. Stacking Architectures

 ${\rm FeS_m}$ is a quasi-two-dimensional layered material characterized by a van der Waals (vdW) space between the layers in the stacking direction. The aggregation-growth process leads to the development of quite complex interactions between mackinawite nanoplates leading to variable spacings for the dominant d_{100} 5Å peak. The XRPD pattern of well-crystalline ${\rm FeS_m}$ in Figure 12b, for example, shows complex development of the d_{001} reflection.

Various stacking architectures of mackinawite nanoplates can give rise to multiples of the main 5 Å XRPD reflection. These stacking architectures can be classified into three groups (Figure 17): (a) simple stacking where the layers are stacked directly on top of each other (b) translational stacking where the 2D layers are offset relative to each other and (c) rotational (twisted) stacking where successive layers are rotated with respect to each other.

9.2.1. Simple Stacking. Simple stacking (Figure 17a) gives rise to multiples of the 5 Å XRPD reflection. This was originally reported in the quasi-mineral *dorite* which was synthesized in media similar to that of saline lakes ²²⁶ where the major XRPD peak was at around 10 Å, twice that of mackinawite. The intensity of this 10 Å peak decreased with time commensurate with the appearance of the conventional 5 Å peak. Ritvo et al. ²²⁶ interpreted this phase as a precursor phase to mackinawite. It appears that they had captured a stage in the aggregation growth

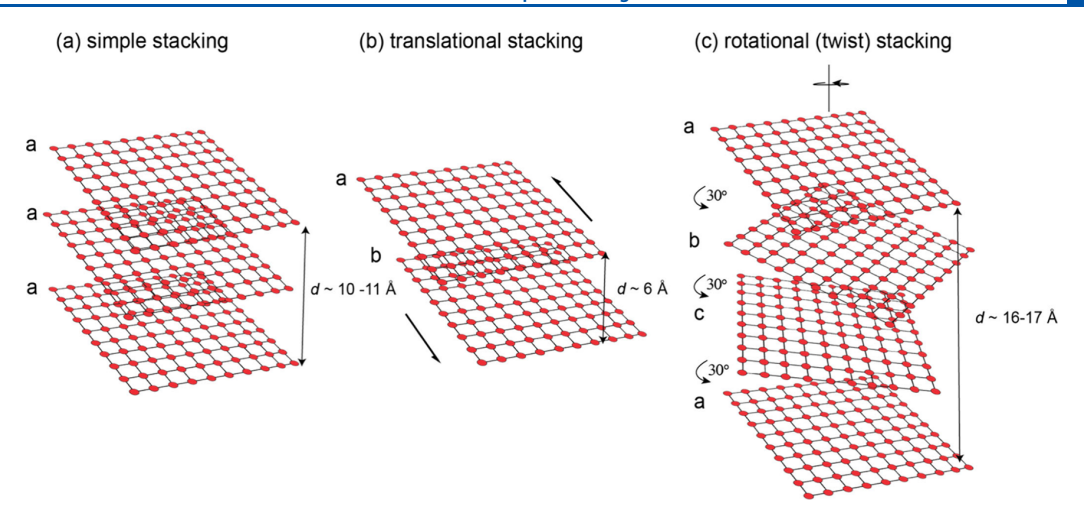


Figure 17. Three different stacking architectures for square ²²³ arrays similar to FeS_m: (a) simple stacking with plates located directly over each other. The d_{001} spacing is then a simple multiple of the number of aggregated plates ($d_{001} \sim 10-11$ Å for three FeS_m plates: e.g., dorite). (b) translational stacking with a superjacent plate laterally displaced ($d_{001} \sim 6$ Å: e.g., FeS_m on α -Fe; see Figure 19). (c) rotational (twisted) stacking with superjacent plates rotated at 30° to each other. In a square planar array the fourth plate will have a similar orientation to the first plate giving a 3d sublattice (e.g., FeS_m with intercalated ethylenediamine ³⁴).

of mackinawite where a fraction of the FeS_m nanoplates had paired in the precipitate to produce a 10Å XRPD reflection.

9.2.2. Translational Stacking. Translational stacking (Figure 17b) has been reported for FeS_m growth on metallic $Fe.^{227}$ In this process, successive FeS_m type layers are shifted unidirectionally. The aqueous sulfide reacts with the α -Fe surface to produce a layer of FeS with a tetragonal, mackinawite-like structure. The geometry of the square planar array of Fe atoms in FeS_m is similar, but not identical, to that of α -Fe. The Fe—Fe distance in FeS_m is 2.5976 Å, a little less than the Fe-Fe distance of 2.866 Å in α -Fe. The α -Fe substrate then provides a strong epitaxial control on the architecture of the initial FeS_m layers.

Detailed analyses of the structure of this epitaxial precipitate showed that the XRD reflection varies with time, initially increasing to 5.30 Å before decreasing to 5.03 Å, the normal value for mackinawite (Figure 18). This variation in d_{001} with time is consistent with molecular modeling of the process (Figure 19) which shows that, in the initial stage of formation of FeS_m, the mackinawite (001) layers are offset bringing the sulfur (S) $3p_z$ lone pairs of one layer into close proximity with and between the lone pairs of the adjacent layer.³²

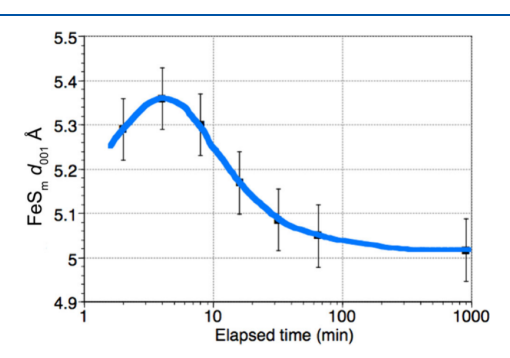


Figure 18. Variation of d_{001} with time for FeS_m formed on α-Fe. Adapted with permission from ref 32. Copyright 2024 Elsevier.

At an offset of 0.5a (where XRD peak offset a is the unit cell dimension parallel to [001]) the Fermi energy is at a local maximum. Offsets greater or less than 0.5a are more stable and the Fermi level of normal mackinawite (0 offset) being at a minimum.

The crystal structural development of FeS_m shown by relative offsets of (001) to the ideal mackinawite structure is confirmed by the observations of variations of peak intensities of 200 and 112 reflections with time (Figure 20). Multiplicity is the number of peaks that overlap in a powder pattern and this plays an important role in determining the relative intensities of these reflections. In the mackinawite tetragonal (P4/nmm) structure the d_{200} XRD reflection has a multiplicity of 4 and the d_{112} reflection a multiplicity of 8. When adjacent layers are offset along [001] the structure is distorted and the multiplicity of the 200 reflection decreases; this reverts to 4 as the offset \rightarrow 0 with the formation of the normal mackinawite structure. The relative intensities of the d_{112} and d_{200} peaks thus change with time as the multiplicity of the d_{200} peak varies. In these experiments which were run between 25 and 45 °C the time taken for the development of the regular mackinawite structure was around 15 h.

9.2.3. Rotational Processes: Twistronics. The search for new and cheaper superconducting material has led to a burgeoning interest in the science of twistronics, 228 the study of how the relative angle between adjacent layers of sheet materials like ${\rm FeS}_{\rm m}$ can change their electrical properties. The original simple translational offset model 227 has been refined to a general model of twisting layers of ${\rm FeS}_{\rm m}$ by intercalating ethylenediamine ($C_2{\rm H_8N_2}$) molecules between the layers. 34

The insertion of ethylenediamine results in the formation of Fe-vacancies in the FeS_m layers. This makes the FeS_m layers anionic and slightly distorted from a planar array. The Fe-S sheets become relatively rotated (Figure 21) forming a coincident site lattice where the Fe vacancies are capped by a sulfur atom from the underlying layer³² or an $[\text{Fe}(\text{en})_3]^{2+}$ complex. The reason for the rotation of the FeS_m sheets in these intercalated compounds is presently unclear. It appears to result from the combined effects of vacancy creation, charge

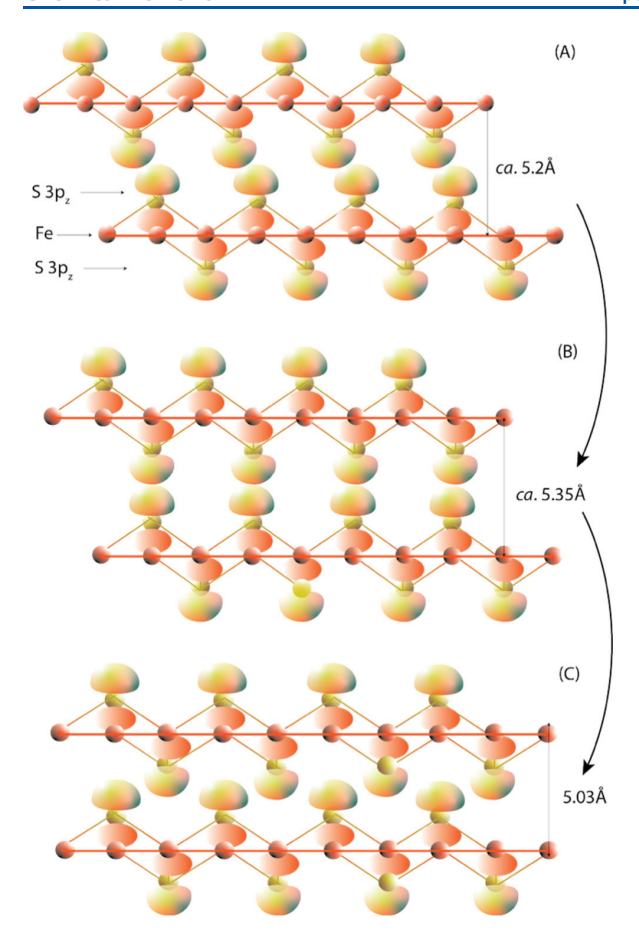


Figure 19. Effect of sulfur (S) $3p_z$ nonbonding lone-pair orbitals on the development of the mackinawite structure: (a) Initial stage of formation with S $3p_z$ orbitals slightly offset from nearest orbitals in the adjacent layer, (d_{001} ca. 5.2 Å); (b) at 0.5a offset (maximum repulsion, d_{001} ca. 5.35 Å); (c) normal mackinawite structure (d_{001} 5.03 Å). The upward-pointing $3p_z$ lobes are offset into the page by 1/2a relative to the downward-pointing lobes. Adapted with permission from ref 32. Copyright 2024 Elsevier.

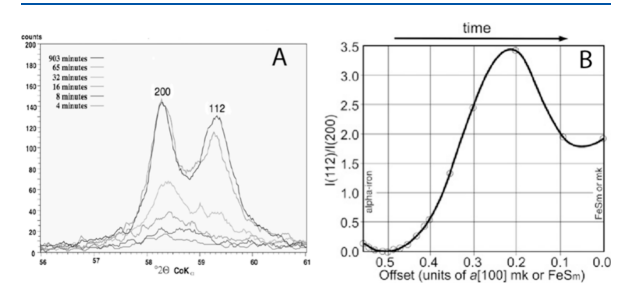


Figure 20. Changes in intensities of mackinawite 112 and 200 with time (A) experimental XRD measurements, (B) computed intensity ratios from α -Fe (0.5508a offset) to normal mackinawite (0a offset). Adapted with permission from ref 32. Copyright 2024 Elsevier.

balance intercalation and noncovalent bonding interactions of the intercalated complexes. The resulting vacancy architectures result in the development of supercells based on the FeS_m structure with $a \approx a \text{ FeS}_m$ and $c \leq 20.62 \text{\AA}.^{34}$

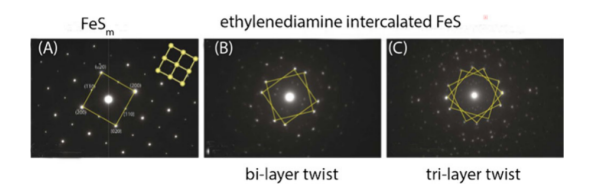


Figure 21. Electron diffraction images of (a) FeS_m showing the reflections of the square planar Fe substructure (b) and (c) FeS_m with intercalated ethylenediamine. Reproduced with permission from ref 34. Copyright 2024 Royal Society of Chemistry.

10. OXIDATION

Experimental investigations into the chemistry of FeS_m have been constrained by the extraordinary sensitivity of the precipitate to oxidation. Oxidation in air is easily observed but the sensitivity of the material means that pressures as low as 10^{-7} MPa (10^{-6} bar or $<10^{-3}$ torr) may result in oxidation of the material. 27,229 This means that FeS_m analyses in all instruments not attaining ultrahigh vacuum may be subject to oxidation and oxidation may occur in the sample while the instrument is being pumped down. The extreme sensitivity of the material to oxidation is further illustrated by the observation that H_2S is an effective oxidation agent for FeS_m .

10.1. Oxidation by O₂

The rate of oxidation of FeS_m has proved controversial. In some preparations, oxidation is very rapid, and the material is pyrophoric. In other cases, it seems to last for weeks in air at room temperature. It has been suggested that well-crystalline FeS_m is oxygen-resistant whereas the nanoparticulate precipitate is rapidly oxidized. Esc by contrast, others have reported that nanoparticulate FeS_m is resistant to oxidation when wet but pyrophoric when dry, but this is not a general observation.

The oxidation of electroactive, nanoparticulate FeS, may cast some light onto the mechanism of oxidation of FeS_m. The enhanced surface:volume ratio of the nanoparticulate material means that it is particularly susceptible to oxidation. It also means that sample handling in most microscopic and spectroscopic systems is particularly difficult. The results of the experimentation risk being empirical and there is some support for this interpretation in the variety of differentially oxidized forms of nanoparticulate FeS with variable amounts of Fe^{II}, Fe^{III}, S^{-II}, S₂^{-II} and S_n^{-II} that have been reported. ²⁸,35,105,106,118,138 The original study by Mullet et al. ²⁸ used X-ray photoelectron spectroscopy (XPS) to probe FeS_m composition and reported up to 20% Fe^{III} and 19 atomic% O in an FeS_m surface layer and this was later confirmed by Raman spectroscopy. ³⁵ Cryptic oxidation of FeS_m has led to misidentification of Raman spectra, particularly since some of the peaks of α -Fe₂O₃ are similar to those of FeS_m.

The final product of the oxidation of FeS_m is a Fe^{III} oxyhydroxide. If the Fe^{III} oxyhydroxide is produced by precipitation from an aqueous medium, then the form of the material merely follows the standard aqueous chemistry of Fe(III)^{231,232} and has no direct relation to FeS_m. The FeS_m structure has an effect on the oxyhydroxide product where the oxidation is a solid-state transformation. The oxidation product has been reported to be orthorhombic γ -FeOOH, equivalent to the mineral lepidocrocite, ³⁰ monoclinic β -FeOOH, equivalent to the mineral akageneite, ²³⁰ and an unspecified Green Rust (mixed valence iron oxyhydroxides with an hexagonal structure). ²³³ However, in most cases, the exact nature of this

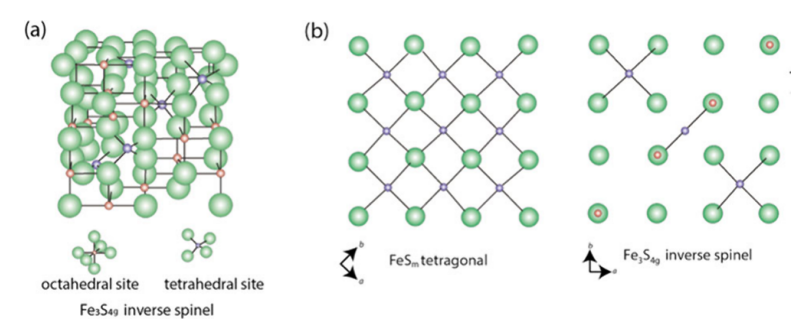


Figure 22. (a) Inverse spinel structure for $Fe_3S_{4g'}$ greighte. Fe^{III} atoms are situated in tetrahedral sites and mixed Fe^{II}/Fe^{III} atoms occupy the octahedral sites. (b) homology of the tetragonal FeS_m and the inverse spinel Fe_3S_{4g} structures Adapted with permission from ref 27. Copyright 2007 American Chemical Society.

material is unknown: most of the reported experimentation is highly empirical and the oxidized products poorly defined.

10.2. Mackinawite → Greigite

The transformation of ${\rm FeS_m}$ (mackinawite) to ${\rm Fe_3S_{4g}}$ (greigite) is facile and often difficult to prevent. The transformation is an equilibration reaction and has been mainly responsible for the uncertainties in the properties of ${\rm FeS_m}$ and ${\rm Fe_3S_{4g}}$. For example, the solubility of ${\rm Fe_3S_{4g}}$ was overestimated because of the tendency for synthetic ${\rm Fe_3S_{4g}}$ particles to contain relic ${\rm FeS_m}$ layers 107,150 and the composition of ${\rm FeS_m}$ has been uncertain because of possible incipient oxidation to ${\rm Fe_3S_{4g}}$.

The overall unbalanced reaction is described in equation 8 where the formal oxidation states of the iron and sulfur are indicated. It involves 75% of the $\mathrm{Fe^{II}}$ in $\mathrm{FeS_m}$ being oxidized to $\mathrm{Fe^{III}}$ and the $\mathrm{S^{-II}}$ to remain unoxidized.

$$Fe^{II}S^{-II} \rightarrow Fe^{II}Fe^{III}{}_{2}S^{-II}{}_{4}$$
 (8)

The oxidation reaction is complicated by the distribution of Fe^{II} and Fe^{III} in the product Fe_3S_{4g} between the spinel tetrahedral and octahedral sites: the tetrahedral sites are occupied by Fe^{III} whereas equal amounts of Fe^{II} and Fe^{III} occupy the octahedral sites (Figure 22a). During the oxidation reaction, Fe^{III} is preferentially located in the tetrahedral, FeS₄, sites of the original $\mbox{FeS}_{\mbox{\scriptsize m}}.$ There is a clear difference in the charge distribution between the tetrahedral and octahedral sites with Fe in the tetrahedral sites carrying a positive charge, but a lower charge $(\rightarrow 0)$ at the octahedral sites. By contrast to the octahedral sites, the d₂₂ level of the Fe 3d orbitals at the tetrahedral sites strongly interact with the S 3p orbitals and excess Fe^{II} is accommodated at the octahedral sites. In effect the transformation occurs through the rearrangement of Fe atoms within a ccp sulfur substructure (Figure 22b). The structural homology of isometric Fe_3S_{4g} with tetrahedral FeS_m has led to uncertainties in the interpretation of simple XRPD data of FeS reaction products. The XRPD patterns of the two phases are quite distinct except for the coincidence of the most intense 100 reflection of Fe₃S_{4g} at 2.98 Å with the fourth most intense d_{101} reflection of FeS_m. As noted in section 5, this may have led to overestimates of the reported abundance of Fe_3S_{4g} in FeSreaction products which have been widely identified solely on the basis of XRPD data.

$$4Fe^{II}S^{-II} = Fe^{II}Fe^{III}{}_{2}S^{-II}{}_{4} + Fe^{2+} + 2e^{-}$$
(9)

Although the electronic and structural changes during the transformation of FeS_m to Fe_3S_{4g} are well established (equation 9) the oxidation mechanism is not well understood. The kinetics

of the reaction have not been studied in a manner which allows the reaction mechanism to be determined. In particular, equation 9 as written suggests that Fe^{2+} is a product and this is accompanied by the production of 2 electrons per mole of Fe_3S_{4g} produced. The problem has been that the oxidation of FeS_m to Fe_3S_{4g} has also been observed to occur in anhydrous conditions under vacuum in an electron microscope. 23,234,235

$$4Fe^{II}S^{-II} = Fe^{II}Fe^{III}_{2}S_{4}^{-II} + Fe^{0}$$
(10)

$$4Fe^{II}S^{-II} + 0.5O_2 = Fe^{II}Fe^{III}_2S_4^{-II} + FeO$$
 (11)

There appears to be two possible reactions for the oxidation reaction in these conditions: Equation 10 describes the reaction where the product is metallic Fe and equation 11 presents an overview of the reaction where the product is an iron oxide: in this case, FeO represents an unspecified ferrous iron oxide.

Equation 10 was found to be thermodynamically improbable using the older ${\rm Fe_3S_{4g}}$ stability data²⁰ but the revised stability data show $\Delta G^{\circ}_{\rm r} = -40.7~{\rm kJ~mol^{-1}}$ for equation 10 and the assemblage ${\rm Fe_3S_{4g}} + {\rm Fe^0}$ is stable relative to ${\rm FeS_m}$. The result explains why the Fe:S ratio in the observed anhydrous reaction does not appear to change.²⁷ Even though an additional phase such as metallic iron has not been identified, it is possible that dispersed ${\rm Fe^0}$ nanoparticles within the product greigite would not have been detected.

The oxidation of FeS_m by molecular oxygen is considered in equation 11 where FeO represents an unspecified oxide of iron. This reaction is thermodynamically and kinetically probable. $\Delta G_{\rm r}^{\circ}$ for reaction 11 is -294.2 kJ mol⁻¹ and log $P_{\rm O_2}$ at equilibrium is $\sim 10^{-10}$ bars or $\sim 10^{-7}$ torr which suggests that oxygen partial pressures in a high vacuum electron microscope of 10⁻⁶ torr would be above the level needed to facilitate the oxidation. The result explains why the $FeS_m \rightarrow Fe_3S_{4g}$ transformation can be observed in the vacuum of an electron microscope. Older electron microscopes may have been pumped down by single stage rotary vacuum pumps, which provide a pressure of 10^{-3} torr, well above the P_{O_2} needed to complete the transformation reaction. The formation of a surface layer of Fe_3S_{4g} on FeS_m can occur through storage in the ambient atmosphere for several days.³⁰ The formation of the Fe_3S_{4g} layer results in a reduction in the BET determined specific surface area from 80 to 3 g m⁻². The reduction in the specific surface area together with armoring of the FeS_m particles with stable Fe_3S_{4g} both contribute to the apparent stability of FeS_m in

The result is important for the analytical chemistry of FeS. Considerable efforts are commonly documented to exclude oxygen during the synthesis of FeS compounds. For example, the gas phase used has evolved from earlier inert gas (e.g., N_2), to a scrubbed inert gas (e.g., O_2 -free N_2) to a mixture of a scrubbed inert gas and hydrogen (e.g., 95% O_2 -free $N_2+5\%$ H_2). The products of these careful syntheses are then analyzed in electron microscopes and various spectrometers. These commonly work at high vacuums which are above the equilibrium P_{O_2} level for FeS_m oxidation. Ultrahigh vacuum systems, such as the Diamond Light Source, can maintain a vacuum of $\sim 10^{-14}$ bar, which is below the equilibrium level. However, in all cases there is a practical problem of oxidation occurring during sample handling. 28,107,236

The same process occurs in any analytical instrument involving a simple vacuum system. For example, greigite XRD reflections were first observed in an X-ray powder diffractometer at 100 °C after stepwise heating of FeS_m from room temperature. 237 The reaction may be catalyzed by damage caused to the FeS_m structure by electron or X-ray beams. 20 The problem with this explanation of the oxidation process is that Fe oxides have not been observed in the reaction products.

In aqueous solutions, the autoxidation of FeS_m by H_2O was considered (equation 12).²⁰

$$4Fe^{II}S^{-II} + 2H_2O = Fe^{II}Fe^{III}_2S^{-II}_4 + Fe^{II}(OH)_2 + H_2$$
(12)

However, ΔG°_{r} for reaction 12 is large and positive ²⁰ and even inclusion of the revised stability data for Fe₃S_{4g}¹⁵⁶ still results in $\Delta G^{\circ}_{r} = +56 \text{ kJ mol}^{-1}$. This means that P_{H2} fugacity for the equilibrium reaction is inhibitingly high in most laboratory and natural environments.

The oxidation reaction with molecular oxygen (equation 11) appears the most likely route in aqueous systems. In these systems, the addition of H_2O to the reactants in equation 11 would result in the production of Fe hydroxides, oxyhydroxides or oxides, but ΔG°_r does not change sufficiently for the equilibrium P_{O2} values to be significantly different. The O_2 system in most aqueous systems is not at equilibrium concentrations but up to 1.2×10^{-3} mol L^{-1} can be dissolved in pure water at STP which is several magnitudes greater than the equilibrium value for reaction 11.

Against the background of the facile transformation of FeS_m to stable Fe_3S_{4g} , the absence of any reports of greigite associated with mackinawite in the high temperature sulfide ore association is mysterious. It may well be that it has been missed since greigite under the reflected light microscope is both isotropic and has a low reflectivity. The absence of any reports of greigite in this mineral association is consistent with this explanation.

10.3. Oxidation by Sulfur Compounds

The oxidation of the sulfide in FeS $_m$ often leads to the formation of the stable phase, pyrite, isometric FeS $_{2p}$. By contrast the transformation of FeS $_m$ to Fe $_3$ S $_{4g}$, pyrite formation from FeS $_m$ requires significant rearrangement of both the Fe and S substructures: no parts of the structures of the two phases are homologous (Figure 23). The reaction cannot proceed via a simple solid state, equilibration, transformation. Rather the process appears to involve reaction of $\langle \text{FeS} \rangle$ moieties either on the surfaces of iron materials or in solution. 20,194,195

The oxidation of FeS_m by $S_2(-II)$ species (Table 19, eq 13) is written in terms of the polysulfane ion, HS_2^- , since this dominates polysulfide speciation in aqueous solutions at STP, 5

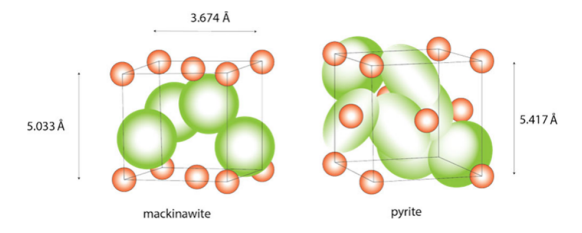


Figure 23. Comparison between the mackinawite and pyrite structures showing lack of homology. The rendering of the pyrite structure follows an original computation by ref 238.

Table 19. Sulfur Oxidation Reactions of ${\rm FeS_m}$ and the Logarithm of Their Equilibrium Constants at STP

reaction	$\log K$
$FeS_m + HS_2^- = FeS_{2p} + HS^-$ (13)	12.6
$FeS + H_2S_{aq} = FeS_{2p} + H_{2g}$ (14)	6.0
$FeS + S^0 = FeS_{2p} $ (15)	28.1

< pH $<10^{239,240}$ and the formulation avoids the uncertainties in the stability of the sulfide ion, $S^{2-,20}$ The reaction is a substitution reaction whereby $S_2(-II)$ replaces the S(-II) in $\langle FeS \rangle$ either on the FeS_m surface or in solution, or both. The mechanism has been proven isotopically. 241

The oxidation reaction was originally written in terms of elemental sulfur (Table 19, equation 15). 242 Although this reaction is thermodynamically favored, it was shown to be the sum of two reactions involving the formation of polysulfides by the reaction between S^0 and aqueous S(-II) and the substitution of the S(-II) in FeS by $S_n(-II)$. 214,243 The reaction appears to be facile at higher temperatures in both anhydrous and aqueous systems 244 but the form of the FeS reactant is difficult to control experimentally since FeS_m is metastable and rapidly transforms irreversibly to hexagonal pyrrhotite, $\text{Fe}_{1-x}S_{po}$, at higher temperatures. 178

The oxidation of FeS by H_2S (Table 19, equation 14) was originally described by Berzelius²⁴⁵ and has been revisited several times, in different contexts, during the last 200 years (e.g., $^{115,246-248}$). The logarithm of the equilibrium constant for the oxidation of FeS_m by H_2S at 25 °C (14) is 6.0. The mechanism involves the formation of an inner-sphere complex between $\langle \text{FeS} \rangle$ and H_2S followed by electron transfer between S(-II) and H(I) to produce $S_2(-II)$. The initio molecular dynamics computations suggest that H_2S is initially physically absorbed on the (001) surface of FeS_m , dissociates and the H atoms are trapped in the interlayers. The reaction mechanism has been proven isotopically. So By contrast with H_2S , which is a good oxidizing agent on a par with O_2 , HS^- is nucleophilic and does not oxidize S(-II). Since at STP, H_2S dominates aqueous S(-II) speciation at PH < 7, the oxidation of the PeS_m by P_2S in aqueous solutions becomes important in acidic sulfide solutions. The PH regime in which this reaction occurs is quite limited since PeS_m becomes increasingly soluble at $PH < \sim 6$.

11. SURFACE CHEMISTRY

A surface complexation model was developed for ${\rm FeS_m}^{252}$ which suggested two equally distributed surface site types of functional sulfide groups that readily exchange ${\rm H^+:(1)}{\equiv}{\rm FeSH^0}$, a strongly acidic monocoordinated group and ${\rm (2)}{\equiv}{\rm Fe_3SH^0}$, a weakly acidic tricoordinated group. The site density is 4 sites ${\rm nm}^{-2}$ and

the site concentration is 1.2 mM g⁻¹ FeS_m. The point of zero charge for FeS_m has been determined to be $\sim 7.5^{252}$ and earlier reported values $\sim 2.9^{216}$ were a consequence of irreversible surface protonation.

11.1. Adsorption

Acid volatile sulfide (AVS) is a measure of the H₂S released on acidification of natural samples with HCl.²⁵³ It has been combined with analyses of extracted metals, called simultaneously extracted metals (SEM), to provide a cheap and simple indicator of metal toxicity. 254 AVS was originally equated with mackinawite although this was shown later not to be the case and the AVS derives from a variety of solid and dissolved sulfide phases.²⁵⁵ Although toxicological studies questioned the validity of the results from the method, 256 it became a standard procedure of several national environmental protection agencies worldwide.

Trace and minor elements are sequestered by FeS_m by 5 major processes (Table 20). The basic process is surface reaction sensu

Table 20. Mechanisms of Sequestration of Exotic Compounds (X) by FeS_m

process	reaction
surface reaction	$FeS_m + X \rightarrow Fe - S \equiv X$ (16)
replacement	$Fe - S \equiv X \rightarrow Fe(X)S + Fe$ (17)
exchange (metathesis)	$FeS_m + X \rightarrow XS + Fe$ (18)
coprecipitation	$Fe(II)_{aq} + X_{aq} + S(-II)_{aq} \rightarrow FeS_m + XS \downarrow (19)$
	$S(-II)_{aq} + X \rightarrow XS$
intercalation	$FeS_m + X \rightarrow FeS_m X FeS_m$ (20)

stricto which involves the formation of a chemisorbed product (Fe-S \equiv X) on the FeS_m surface (equation 16). Surface reaction is a necessary precursor to the inclusion of an exotic element into FeS_m (equation 17). It is a significant process since the inclusion of metals such as Ni, Co, Cu, Cr, V, and Mn in mackinawites in high temperature ores was one of the original impetuses for the subsequent interest in FeS_m as a potential material for the removal of deleterious elements from the environment. The metals replace Fe in the mackinawite structure.^{2,38} Exchange (equation 18) - also known as metathesis- was originally promulgated as the most widespread process for the incorporation of exotic species, especially metals, in FeS_m. The process results in the formation of a distinct sulfide compound of the exotic element. The importance of coprecipitation (equation 19) was underestimated until techniques became available to identify phases on the FeS_m surface at the molecular level. The documentation of the relative solubility of FeS_m and the relative kinetics of metal sulfide precipitation from aqueous solutions 195 contributed to documenting the importance of coprecipitation as a sequestration process. Intercalation of exotic species (equation 20) in the interlayers of the FeS_m structure, (FeS_m|X|FeS_m), is discussed in section 4.

11.2. Element Sequestration

There is a substantial literature dealing with the sequestration of elements by FeS_m, mainly in response to environmental concerns. However, minor and trace elements rarely occur in aqueous solutions as free ions: they are normally complexed or ligated. 195 This means that the chemistry of the element varies

according to the chemical characteristics of the medium. The concentration of complexing and ligating agents, pH and pe may all play important roles in determining the chemical form of the element in any particular natural solution at any given time. The consequence is that determining the efficiency of FeS_m as a sequestrating agent for any specific element is complicated and likely to be highly empirical.

The sequestration of substances by FeS_m is conventionally considered on an elemental basis and Table 21 summarizes

Table 21. Examples of Element Sequestration by FeS_m

	comment	ref
V(V)	reduced to V(III)	24
V(IV)	incorporated into structure	125
Cr(VI)	reduced to Cr(III)	259-261
Mn(II)	adsorbed (pH \leq 7)	70,262
	coprecipitated (pH > 7)	
Co(II)	coprecipitated	188
Ni(II)	coprecipitated	188
	exchange	140,263
Cu(II)	coprecipitation	
	exchange	264-267
Zn(II)	coprecipitation	267
As (III)	adsorption and coprecipitation	233,268-271
As(V)	adsorption and coprecipitation	268,272-274
Se(-II)	coprecipitation	275
Se(IV)	adsorption	276,277
Se(VI)	adsorption	276
Mo(VI)	adsorption	278
Tc(VII)	reduced to Tc(IV)	279
Cd(II)	exchange	266,280,281
	coprecipitation	266,282
	surface reaction on oxidized surface	283
Sb(III)	adsorption and coprecipitation	284,285
Sn(II)	chemisorbed	286
I	chemisorbed on oxidized surface	287
Au(I)	reduction to Au ⁰	216
Hg(II)	adsorption	288-291
	coprecipitation	267,292,293
	exchange	192
Pb(II)	exchange	280
U(VI)	reduced to U(IV)	279,294-296
Np(V)	reduced to Np(IV)	279,297
Pu(V)	reduced to Pu(III)	298

examples of elements sequestered in FeS_m that have been reported in the literature. Experimental data on the sequestration of more than 20 elements have been reported to date.

FeS_m is also susceptible to oxidation during storage, transport and utilization and these processes can substantially modify the apparent adsorptive capacity of the material. The empirical nature of much experimentation has given rise to inconsistent results regarding FeS_m adsorption. The careful experimental identification of oxidation has clarified some of the variable results. For example, oxidation of FeS_m enhances the removal of As, Sb, and W,^{285,299} whereas it decreases the sequestration capacity for Mo and Hg.^{299,300} U(VI) undergoes reductive precipitation forming a U^{VI}/U^{IV} solid often identified as uraninite. ^{145,294,296,301,302} The effect of surface oxidation of FeS_m on adsorption increases U(VI) adsorption. ^{295,296} Although $Sn(\widetilde{II})$ is chemisorbed onto the pristine FeS_m surface, at pH > 9 a

mixed Fe^{II}/Fe^{III} oxyhydroxide (green rust (II)) forms on the FeS_m surface and oxidizes Sn(II) to Sn(IV).

One approach to ameliorate these problems is to attach a stabilizer, such as polymers and surfactants, in order to reduce aggregation of the ${\rm FeS_m}$ particles. These stabilizers may also provide surface functional groups to increase the efficiency of the ${\rm FeS_m}$ particles in reducing the concentration of deleterious substances. For example, sodium carboxymethyl cellulose (CMC) and gelatin suppress the aggregation of ${\rm FeS_m}$ particles, increase U(VI), Hg, Cd, Cr (VI), Cu, Ni, Pb, Tl, Tc, and Zn adsorption efficiency and reduce the effect of salinity on ${\rm FeS_m}$ particle aggregation. $^{303-313}$ In addition to CMC, starch, glucose, beef extract, gelatine, peptone, yeast extract, 303 cyclodextrin, xanthum gum, activated carbon 314 and polysaccharide sodium alginate have been used in a similar fashion. 315 Stabilization techniques also include carefully controlling ${\rm FeS_m}$ particle shape and size distribution. 316

A further method for increasing the efficiency of FeS_m as an absorbant in natural systems, is the dispersal of FeS_m nanoparticles within porous materials, such as biochar, 317,318 biochar composites 319 and with MgO, 320 starch, 321 chitosan, 322 and CMC, 323 limestone, 324,325 and aluminum oxide. 300

11.3. Surface Reactions

The surface complexation model for FeS_m suggest that the pristine FeS surface is dominated by $\equiv FeSH^0$ and $\equiv Fe_3SH^0$. These undergo a series of protonation reactions (equations 21–24, (Table 22).

Table 22

reaction	$\log K$
$\equiv \text{FeSH}^0 + \text{H}^+ \leftrightarrow \equiv \text{FeSH}_2^+ $ (21)	8.0
$\equiv FeSH^0 \leftrightarrow \equiv FeS^- + H^+ (22)$	-6.5
$\equiv Fe_3SH^0 + H^+ \leftrightarrow \equiv Fe_3SH_2^+ \qquad (23)$	7.9
$\equiv Fe_3SH^{0=} \leftrightarrow \equiv Fe_3S^- + H^+ \qquad (24)$	<-9.5

The surface reaction with arsenic species has been studied in some detail. As $^{\rm V}$ is not reduced to As $^{\rm III}$ at the FeS surface. 268,274,326 As $^{\rm III}$ forms an outer-sphere complex at the FeS $_{\rm m}$ surface and both As species bind to \equiv FeSH $^{\rm 0}$ sites. 268,274

11.4. Reduction

Reported elemental reduction reactions at the FeS_m surface are listed in Table 23. The surface reduction mechanisms are not well constrained, and it has been noted that surface and solution reactions can be described by the same equations. 327 A further problem is distinguishing between the contribution of the

Table 23. Reported Elemental Reduction Reactions at FeS_m surface.

species	reaction	ref
Se ^{IV}	reduced to Se ⁰ and Se ^{-II}	117
V^V	reduced to V^{IV} and V^{III}	24,125
Cr^{VI}	reduced to Cr ^{III}	259-261
$\mathrm{Tc^{VII}}$	reduced to $\mathrm{Tc^{IV}}$	279
Au^{I}	reduction to Au ⁰	216
U^{VI}	reduced to \mathbf{U}^{IV}	279,294-296
Np^{V}	reduced to NpIV	279,297
Pu^{V}	reduced to Pu ^{III}	298

surface reaction to the reduction process and that of reduction in solution and reprecipitation.

$$UO_2^{2+} + \equiv FeS \rightarrow \equiv [S^{2-}.UO_2^{2+}] + Fe^{2+}$$
 (25)

$$\equiv [S^{2-}UO_2^{2+}] \rightarrow S^o + UO_{2(s)}.$$
 (26)

$$FeS_{(s)} + H_2O \rightarrow Fe^{2+} + HS^- + OH^-$$
 (27)

$$\equiv UO_2^{2+} + HS^- \rightarrow S^0 + UO_{2(s)} + H^+$$
 (28)

The problem is illustrated with respect to the reduction of U(VI) to U(IV) where equations 25 and 26 represent the surface reaction with generic \equiv FeS surface species and equations 27 and 28 result in the same surface U^{IV} product (elemental sulfur and nanoparticulate uraninite) via reduction in solution. ¹⁴⁵ By contrast with reductive dechlorination of halogenated hydrocarbons by FeS_m (section 12.1), the rate of U(VI) reduction decreases with increasing pH due to decreasing FeS_m solubility with increasing pH. This shows the relative importance of the solution reduction and reprecipitation route (equations 27 and 28) in U(VI) reduction by FeS_m.

$$H_2V^VO_4^-_{(aq)} + Fe^{2+}_{(aq)} + 3H^+$$

= $V^{IV}O(OH)^+_{(aq)} + Fe^{3+}_{(aq)} + 2H_2O$ (29)

Likewise, aqueous Fe^{2+} promotes V^V reduction to V^{IV} (equation 29) at a slower rate than the adsorption-reduction process at the FeS_m surface, ¹²⁵ but the reaction, which subsequently involves reprecipitation of V^{IV} as $V^{IV}O(OH)_2$, contributes to the kinetics of the overall process.

The standard electrode potentials for many of the reduction reactions listed in Table 23 are shown in Table 24. These are

Table 24. Standard Electrode Potentials, E^0 in V Relative to the Standard Calomel Electrode (from ref 328 Except Where Noted)

reaction	$E^{0}(V)$
$Au^+ + e^- = Au^0$	1.69
$0.17Cr_2O_7^{2-} + 2.33H^+ + e^- = 0.67Cr^{3+} + 1.17H_2O$	1.36
$Pu^{5+} + e^{-} = Pu^{4+}$	1.10
$VO_2^+ + 2H^+ + e^- = VO_2^+ + H_2O$	0.99
$0.33 \text{TcO}_4^- + 1.33 \text{H}^+ + \text{e}^- = 0.33 \text{TcO}_2 + 0.67 \text{H}_2 \text{O}$	0.78
$\mathrm{NpO_2}^+ \rightarrow \mathrm{Np^{4+}} + \mathrm{e^-}$	0.60^{329}
$UO_2^{2+} + e^- = UO_2^+$	0.06
$HS^- = HS_2^- + H^+ + e^-$	-0.03^{330}
$V^{3+} + e^{-} = V^{2+}$	-0.26
$0.25 \text{SeO}_3^{2-} + 0.75 \text{H}_2 \text{O} + \text{e}^- = 0.25 \text{Se} + 1.50 \text{OH}^-$	-0.366
$Fe^{2+} \rightarrow Fe^{3+} + e^{-}$	-0. 77
$0.5Se^0 + e^- = 0.5Se^{2-}$	-0.93

relatively crude indicators of the reducing potential of FeS_{m} given in terms of Fe(II) and S(-II) oxidation potentials. Most of these reactions are initiated by single electron transfer (SET) processes where a single electron is inserted into the incoming species and further reduction may subsequently cascade down. The electropotential scale in Table 24 suggests that the oxidation potential of Fe(II) is sufficiently low to supply

electrons to all the reported redox reactions (except the reduction of Se(0) to Se(-II)), even in view of the likely errors due to kinetic factors. By contrast, the oxidation of sulfide to disulfide has a higher potential suggesting that it will not reduce V(III) to V(II) nor Se(IV) to Se(0).

$$6 \equiv \text{Fe}^{\text{II}} + \text{HSeO}_3^- + \text{FeS} + 6\text{H}^+ \rightarrow 6 \equiv \text{Fe}^{\text{III}} + \text{FeSe}$$

+ HS⁻ + 3H₂O (30)

$$4 \equiv \text{Fe}^{\text{II}} + \text{HSeO}_3^- + 5\text{H}^+ \rightarrow 4 \equiv \text{Fe}^{\text{III}} + \text{Se} + 3\text{H}_2\text{O}$$
(31)

The reported products of the reaction between FeS_m and $\operatorname{Se}(\operatorname{IV})$, in the form of the $\operatorname{HSeO_3}^-$ ion, include both $\operatorname{Se}(0)$ and FeSe (equations 30 and 31). 117 The reduction in both cases is coupled to the oxidation of surface $\equiv \operatorname{Fe^{II}}$ to $\equiv \operatorname{Fe^{III}}$. However, E^0 for the reduction of $\operatorname{Se}(0)$ to $\operatorname{Se}(-\operatorname{II})$ is below that for the oxidation of $\operatorname{Fe}(\operatorname{II})$ to $\operatorname{Fe}(\operatorname{III})$ and it appears difficult to couple these reactions. It has been suggested that Se reduction is kinetically decoupled from the rapid oxidation of aqueous $\operatorname{Fe}(\operatorname{II})$ to $\operatorname{Fe}(\operatorname{III})$, but the reduction continues with a slower reaction with $\operatorname{Fe^{II}}$ at clay mineral surfaces, possibly due to the formation and storage of a hydrogen intermediate. 331 The similar formation and storage of a hydrogen intermediate has been identified for the oxidation of FeS_m by $\operatorname{H}_2\operatorname{S}$ (section 10.3).

Surface sulfide oxidation has been reported as the major source of the reduction of Au(I) to Au(0). Au(I) (as $AuHS^0$) is readily reduced at the mackinawite surface to Au^0 with the formation of S^0 (equation 32).

$$Au(I) + \equiv S(-II) \rightarrow Au^{0} + S^{0} + e^{-}$$
 (32)

Both Fe(II) and S(-II) oxidation have been implicated in the reduction of Cr(VI) to Cr(III) (equations 33 and 34) and these equations describe both solution and surface reactions.³²⁷

$$3Fe(II) + Cr(VI) \Leftrightarrow 3Fe(III) + Cr(III)$$
 (33)

$$3S(-II) + 2Cr(VI) \Leftrightarrow 3S(0) + 2Cr(III)$$
 (34)

Elemental sulfur is well-known³³² as a product of the oxidation of aqueous H_2S by Cr(VI) and a mixed $Fe^{III}Cr^{III}$ hydroxide (or a mixture of Fe^{III} and Cr^{III} hydroxides) precipitates on the FeS_m surface at pH > 4.

12. ORGANIC CHEMISTRY

Recent progress has shown that particulate FeS_m has a rich organic chemistry. Interest was first aroused when it was shown³³³ that aldehydic carbonyls facilitated the oxidation of FeS_m to Fe₃S_{4g} but inhibited its oxidation to FeS_{2p}; that is, in the presence of aldehydic carbonyls, Fe^{II} in FeS_m was oxidized to Fe^{III} but the oxidation of S^{-II} to S_2^{-II} was inhibited. The electrophilicity of -CHO results in electron loss from Fe^{II}. 119 The reaction was found to occur with a variety of oxo-acids, including glyoxilic acid, oxalacetic acid, ketaglutaric acid, 3methyl-2-oxovaleric acid and phenylpyruvic acid. $^{\rm 334}$ $\rm FeS_{\rm m}$ is oxidized to γ -FeOOH (lepidocrocite) and elemental sulfur by dissolved organic matter. The composition of the dissolved organic matter used in these experiments was complex with some 9992 different organic molecules identified, mainly unsaturated lignin/phenolic (60%), N-aliphatic (20%), polycyclic aromatics (5%) and carbohydrates (1%). The reaction appears to involve the sulfurization of dissolved organic matter molecules with the formation of organic compounds containing -CHONS and -CHOS groups.

These exploratory results have uncovered the exceptionally rich organic chemistry of ${\rm FeS_m}$. However, the organic compounds considered are often described merely as organic carbon, dissolved organic matter or natural organic matter and this is compounded by a lack of information on the nature of the iron sulfide reactant (e.g., refs 335–337). These problems have been addressed in studies of the reactions between ${\rm FeS_m}$ and halogenated hydrocarbons (sections 12.1 and 12.2), ${\rm CO_2}$ -reduction (section 12.3) and free radical reactions, especially with nucleic acids (sections 12.4 and 12.5).

Since FeS_m is a solid the reactions are primarily surface reactions. The pioneering $work^{252}$ on the surface complexation model for FeS_m (section 12), which demonstrates the prevalence of protonated $\equiv FeSH$ groups on the FeS_m surface, has proven critical to understanding the organic chemistry of FeS_m .

12.1. Reductive Dehalogenation

 ${\rm FeS_m}$ particles degrade halogenated organics, including chlorinated and brominated hydrocarbons. ${\rm FeS_m}$ and its precursor forms are more reactive toward halogenated solvents than other solid iron compounds including both synthetic and natural forms of metallic Fe, pyrite, adsorbed ${\rm Fe^{2+}}$, green rust, magnetite, biotite, and vermiculite. 338

These halogenated hydrocarbons (listed with a key to abbreviations in Table 25) are environmental pollutants since

Table 25. Abbreviations for Halogenated Hydrocarbons Used in Text and an Example of Major Usage

abb	compd	example of use
CT	carbon tetrachloride	solvent
DAC	dichloroethane	VC manufacture
DCB	dichlorobenzene	deodorant
DCE	dichloroethylene	degreasing agent
HBCD	hexabromocyclododecane	flame retardant
HCA	hexachloroethylene	insecticide
HCH	hexachlorocyclohexane	pesticide
PCA	pentachloroethane	solvent
PCB	polychlorinated biphenyls	electrical products
PCE	perchloroethylene	dry cleaning
TBM	tribromomethane	bromoform
TCA	trichloroethane	solvent
TCB	trichlorobenzene	herbicide
TCE	trichloroethylene	degreasing agent
TCM	trichloromethane	chloroform
TeCA	tetrachloroethane	solvent
VC	vinyl chloride	PVC manufacture

they are variously injurious to human, animal and/or plant health and are long-lasting. They are all subject to restrictive use or outright bans in the EU and USA, as well as other jurisdictions.

Table 26 lists examples of reports of dehalogenation reactions with FeS $_{\rm m}$ -like materials. The authors' own descriptions of these materials are listed. There has been much interest in the effect of freeze-drying FeS $_{\rm m}$, especially since it was shown that freeze-dried FeS $_{\rm m}$ did not reduce cis-DCE whereas an aqueous suspension did. ¹²⁴ The other forms listed in Table 26 include aqueous suspensions and centrifuged slurries. The biogenic FeS was prepared by bacteria (with *Shewanella oneidensis* ¹³⁹ and an unspecified sulfate-reducer ¹⁴²) and is not well defined. The results are contradictory: the biogenic FeS $_{\rm m}$ prepared with *Shewanella oneidensis* reduced TCE several times faster than an

Table 26. FeS_m -Like Materials (As Described by the Authors of the Cited Reports), Form of FeS_m Reactant, Halogenated Hydrocarbon Reactant, and the Products of Reductive Dehalogenation, Together with the Date of the Report and the Reference

reactant	description	form	products	date	ref
CT	FeS	centrifugation	TCM	2009	120
CT	FeS	suspension	TCM	2016	123
CT	poorly crystalline mackinawite	freeze-dried	TCM	2000	131
DCA	poorly crystalline mackinawite	freeze-dried	N/A	2000	131
DCE	mackinawite $(Fe_{1-x}S)$	suspension	acetylene	2015	124
HCA	FeS	freeze-dried	PCE, PCA	1998	132
HCA	FeS	freeze-dried	PCE	2001	339
HCA	mackinawite	freeze-dried	PCE	2003	340
HCA	poorly crystalline mackinawite	freeze-dried	PCE and PCA	2000	131
HCH	FeS nanoparticles	freeze-dried	TCB. DCB, benzene	2021	121
HCH	FeS nanoparticles	suspension	TCB	2005	122
PCE	biogenic FeS	suspension	DCA	2013	142
PCE	FeS	freeze-dried	acetylene, DCE and TCE	1999	131,13
PCE	FeS	suspension	DCE, TCE, ethene	2007	136
PCE	mackinawite (FeS)	freeze-dried	acetylene, DCE and TCE,	2007	133,34
PCE	nanosized mackinawite (nFeS)	freeze-dried	acetylene, TCE	2015	130
TBM	poorly crystalline mackinawite	freeze-dried	dibromomethane	2000	131
TCA	FeS	centrifugation	TCA, DCA, ethylene	2009	120
TCA	FeS	centrifugation	DCA	2009	120
TCA	poorly crystalline mackinawite	freeze-dried	DCA	2000	131
TCA	poorly crystalline mackinawite	freeze-dried	DCE, VC	2000	131
TCE	biogenic FeS	freeze-dried	DCE, VC, ethylene	2020	139
TCE	FeS	freeze-dried	acetylene, DCE	1999	134
TCE	FeS	freeze-dried	acetylene, DCE,	2001	339
TCE	FeS	freeze-dried	acetylene, DCE,	2007	133
TCE	FeS	freeze-dried	DCE, VC, ethylene. acetylene	2020	139
TCE	FeS_m		DCE, VC, ethene	2007	136
TeCA	poorly crystalline mackinawite	freeze-dried	DCE	2000	131
TeCA	poorly crystalline mackinawite	freeze-dried	TCE, DCE, acetylene	2000	131

^aAbbreviations are listed in Table 25.

abiogenic control, whereas the material produced by the sulfate -reducers was reported to be not highly reactive.

The mechanisms of the reductive dehalogenation of halogenated hydrocarbons have been reported. 132,133 The process follows multiple pathways involving both the formation of additional carbon-carbon bonds and halogen loss (equation 35) and the replacement of halogens by hydrogen (hydrogenolysis) (eq 36).

$$RCX - CXR + 2e^{-} \rightarrow RC = CR + 2X^{-}$$
 (35)

$$RX + H^{+} + 2e^{-} \rightarrow RH + X^{-}$$
 (36)

The two halogen atoms can be removed from a single carbon atom (α -elimination) or from two separate carbon atoms (β -elimination). It has been reported that, with Fe particles, β -elimination dominates the reduction of compounds containing α , β -chlorine pairs whereas compounds with only α -chlorines are primarily reduced by α -elimination and hydrogenolysis.³⁴² However, with FeS, TCE undergoes both β -elimination to produce acetylene and α -elimination to yield 1,1-DCE.³⁴¹ By contrast, biogenic FeS reduces TCE by hydrogenolysis producing DCE, VC and ethylene but no acetylene. ^{130,139}

Table 27 lists standard electrode potentials for chlorinated hydrocarbons in water. These values were taken from linear free energy computations for E^0 in a dimethylformamide solvent 343 and converted to the aqueous values. 344 The values are all well below those for the oxidation of HS(-I) and Fe(II) (Table 23) showing that FeS_m is a good electron donor for reductive halogenation of chlorinated hydrocarbons. However, the

Table 27. Standard Electrode Potentials (E^0 in V Relative to the Standard Calomel Electrode) In Water for the Reduction of Chlorinated Hydrocarbons (Data from ref 343 Corrected for $\rm H_2O$ as the Solvent by the Method Described by ref 344)

	E^0
carbon tetrachloride	-1.199
hexachloroethane	-1.209
1,1,1,2-tetrachloroethane	-1.581
1,1,1-trichloroethane	-1.795
tetrachloroethylene	-1.817
chloroform	-1.838
1,1,2,2-tetrachloroethane	-1.903
trichloroethylene	-1.946
1,1,2-trichloroethane	-2.089
1,1-dichloroethylene	-2.269
dichloromethane	-2.396
1,1-dichloroethane	-2.414
1,2-dichloroethylene (Z)	-2.415
1,2-dichloroethane	-2.46
chloromethane	-2.54

reaction of aqueous sulfides with PCE and TCE is kinetically inhibited. 133

In any redox reaction there are changes to both the electron donor and the electron acceptor and, although the pathway followed by the organic compounds has been traced in some detail, there is less information about how this process is coupled

to FeS_m. In particular, the surface complexation model for FeS_m would suggest that the reactant groups would be \equiv FeSH 0 and \equiv Fe $_3$ SH 0 . If Fe is the electron acceptor this would suggest the formation of Fe III sites on the FeS_m surface; if the reductant is S $^{-II}$ then it is likely that S $_n^{-II}$ sites would be formed during the reaction. The rate of reductive dehalogenation of chlorinated hydrocarbons by FeS_m is strongly pH dependent suggesting that deprotonation of \equiv FeHS-groups at the FeS surface is a key factor in determining the reduction rate. 120,121,132,339 This is consistent with the ZPC for FeS being around 7.5. 252

Bulk precipitated FeS $_{\rm m}$ itself does not change during reductive dehalogenation of TCE 37 although Fe $_3$ S $_{4g}$ was detected after reaction of FeS $_{\rm m}$ with CT. 123 The reductive dehalogenation of TCE is accompanied by oxidation of surface Fe $^{\rm II}$ in FeS to Fe $^{\rm III30}$ although electron transfer was reported from both S $^{\rm -II}$ and Fe $^{\rm II}$ to the carbon atoms of TCE and HBCD. 139,345 Fe $^{\rm III}$ oxyhydroxide (equivalent to the mineral two-line ferrihydrite) is precipitated on the FeS $_{\rm m}$ surface after reaction with CT. 123

$$RX + e - \rightarrow R \cdot + X \tag{37}$$

The first step in the reaction is an initial single electron transfer. This is assumed 346 to occur via a dissociative mechanism in which cleavage of the carbon-halogen bond occurs simultaneously with the transfer of a single electron (equation 37, where X refers to Cl, Br, or I). Injection of a single electron into the σ^* antibonding orbitals is accompanied by barrierless dissociation of the C-X bond.

A secondary problem in evaluating the chemistry of the FeS_m reactant in reductive dehalogenation is the assumption in many reports that FeS_m is the only FeS reactant present initially and that no other FeS compound is formed during the process. For example, freeze-dried FeS_m may partially transform to Fe_3S_{4g} during handling and the subsequent reaction with TCE produces $\gamma FeOOH$, α -FeOOH and FeS_{2p} , which substantially reduces the efficacity of FeS_m as a dehalogenation agent. ³⁷

12.2. Nonreductive Dehalogenation

Two dehalogenation processes have been reported with FeS which do not involve redox reactions. Dehydrochlorination eliminates one halogen atom and one proton from adjacent carbon atoms producing an unsaturated bond. It was identified as the dominant degradation process for α -HCH by FeS_m and resulted in the stepwise generation of PCH, 1,2,4-TCB, and 1,2-DCB. ¹²¹ Nucleophilic substitution occurs when a nucleophilic group, typically a hydroxyl group, replaces a halogen atom. For example, the dehalogenation of γ -HCH (lindane) involves hydrolysis with the production of TCCH, DCCD, DCB, and chlorobenzene. ¹³⁷

12.3. CO₂ Reduction

Autotrophic carbon fixation was a key process in the original development of biologic molecules and there has been considerable interest in the chemistry of the involvement of iron sulfides in the origin of life since the iron-sulfur world theory, which suggests life started on the surface of iron sulfide minerals, was proposed. The pyrite-forming reaction with $Fe_{1-x}S_{po}$ (synthetic pyrrhotite) was shown to catalyze the formation of a number of reduced carbon compounds (including thiols, CS_2 and dimethylsulfide).

When it was demonstrated that a similar H₂-producing reaction occurred with FeS_m as a reactant, ¹¹⁵ experimental interest expanded to encompass both mackinawite³⁵¹ and greigite. ¹⁸⁶ At the same time, as is usual with fundamental chemistry, interest in these reactions has extended to other

technological fields such as carbon capture and fuel production.³⁵² Some of these reactions are listed in Table 28.

Table 28. Reported Organic Reduction Reactions Involving FeS_m Compounds as Catalysts

S reactant	C reactant	products	environment	ref
Ni-doped FeS?	CO ₂	HCOO ⁻	pH gradient	349
Mn -doped FeS_m	CO ₂	CH ₃ OH	80-120 °C	126
$FeS_m + H_2S$	KCN	CS ₂ , CH ₃ SH CH ₄ , C ₂ H ₅ SH, (CH ₃) ₂ S, (CH ₃) ₂ S ₂ , Fe ₃ S _{4g}	80 °C	350

The thermodynamics of the direct reduction of CO_2 by H_2 to formic acid (equation 38) is endergonic in the gas phase ($\Delta G^{\circ}_{r}^{298} = +33 \text{ kJ mol}^{-1}$) but slightly exergonic in the aqueous phase ($\Delta G^{\circ}_{r}^{298} = -4 \text{ kJ mol}^{-1}$). ³⁵³ This suggests that the solvent effects of H_2O and the deprotonation of formic acid with base are important cofactors in the reaction. The direct reaction is possible under a substantial pH gradient with an undefined Nidoped FeS phase as a catalyst. ³⁴⁹

$$CO_2 + H_2 = HCO_2H \tag{38}$$

The hydrogenation of CO_2 can also produce methanol with H_2O as a byproduct (equation 39).

$$CO_2 + 3H_2 = CH_3OH + H_2O$$
 (39)

Again, water makes the reaction thermodynamically favorable $(\Delta G^{\circ}^{298} = -79 \text{ kJ mol}^{-1})$ and the reaction is catalyzed by Mndoped FeSm. 126 However, the composition of the Mn-doped FeSm reactant was not reported and the composition of the FeS product was not determined. The free energy changes in reactions 40,41 become less favorable as the temperature and total pressure rise. 353

cyanide protonation:
$$CN + H_2O = HCN + KOH$$
 (40)

 \equiv FeSH deprotonation:

$$\equiv \text{FeSH}_{2}^{+} + 2\text{OH}^{-} = \equiv \text{FeS}^{-} + 2\text{H}_{2}\text{O}$$
 (41)

nucleophilic attack:

$$\equiv$$
FeS⁻ + HCN + H₃O⁺ = Fe-S-CH =NH + H₂O (42

By contrast, a defined FeS_m reactant was used in the reduction of KCN, KSCN, KOCN and CS_2 and the products of the reaction were shown to contain Fe_3S_{4g} . The process involves a nucleophilic attack by deprotonated \equiv FeSH groups on the FeS_m surface (see section 11). The proposed reaction sequence for KCN reduction is summarized in equations 40-42.

12.4. Free Radical Reactions

Reactive oxygen species (ROS) include $O_2^{\bullet -}$, H_2O_2 and $OH \bullet$. The production of these species by the Fenton reaction in pyrite is well established. $^{354-356}$ ROS production during the oxidation of FeS_m 357 has been implicated in the degradation of a number of organic compounds including phenols 358 and fluoroquinolones. 359 However, the production of ROS during the oxidation of FeS_m has proven more controversial, with $OH \bullet$, high valence Fe (e.g., Fe^{IV} , Fe^V) and/or sulfur-based radicals being reported. 360 One report has identified problems with the

interpretation of results using 5,5-dimethyl-1-pyrroline N-oxide (DMPO), aromatic probe compounds such as benzoic acid and phthalhydrazide as spin trapping agents, in iron-based Fenton-like reactions. ³⁶¹ Further analyses of the experimental products show that the products of FeS_m oxidation cannot be freely diffusing, homogeneous $OH \bullet$, $OC^{\bullet-}$, 1O_2 , or Fe(IV). It is more likely to be a surface species, possibly surface-bound $OH \bullet$. ³⁶⁰

 E^0 for OH•/H₂O is 2.81bV which makes OH• an efficient oxidant: most organic contaminants, for example, can be readily degraded by reaction with OH•. The problem with OH• in natural systems is its short half-life of less than 1 μ s which limits both its mass transfer efficiency and long-range reactions. ³⁶² However, OH• production is greater during the oxidation of nanoparticulate FeS_m by O₂ than in the oxidation of siderite, pyrite and Fe⁰ nanoparticles. A partially oxidized form of FeS_m (section 4.3) has been reported to produce more OH• than regular FeS_m. ¹⁰⁸ OH• generated during FeS_m oxidation has been reported to play key role in the oxidation of As(III). ^{363,364} In this case, Fe^{II} in the FeS_m structure was the principal reactant for OH• production.

By contrast with ROS, peroxydisulfate $(S_2O_8^{\ 2-})$ can be activated by FeS_m to generate strongly oxidizing sulfate radicals, $\text{SO_4}^{\ -}$ ($E^0(\text{SO_4}^{\ -}/\text{SO_4}^{\ 2-})=2.6-3.1$ V). These radicals are highly reactive to a wide range of substances, including polycyclic aromatic hydrocarbons. In oxidative treatments, $\text{SO_4}^{\ -}$ radicals are the main species responsible for the extraordinary effectiveness (i.e., 100% in <4 h) of $S_2O_8^{\ 2-}$ for the degradation of 2.4-dinitrololuene (an extremely toxic compound used in the production of polyurethane foams) and the highly toxic, carcinogenic, pesticide, 4-chloraniline. 362 The detailed process involved in the activation of persulfate by FeS_m is not well understood. It appears to be a surface reaction, but how the process is maintained is unclear.

$$Fe^{2+} + H_2S_2 \rightarrow Fe^{3+} + HS^- + HS^-$$
 (43)

The fully protonated disulfide H_2S_2 is the sulfur analog of hydrogen peroxide, $H_2O_2^{365}$ and the comparative frontier molecular orbital energies for the two molecules suggests that a mechanism analogous to Fenton's (43) is possible in the sulfur system. ³⁶⁶

There is a marked symmetry between oxygen- and sulfur-containing free radicals. 366 However, sulfide radical monomers, generally described as HS•, have proven difficult to trap using conventional spin traps because they are highly reactive, transient forms. They have been implicated in other radical reactions 367 including the denaturization of DNA in the presence of FeS_m (section 12.5) and pDNA has been suggested to be a potential sensitive marker of the presence of sulfide radical monomers.

12.5. Biological Chemistry

The biological chemistry of iron sulfides in general is vast since FeS clusters are key moieties in the active centers of respiratory proteins. However, this review refers strictly to the biological chemistry of particulate ${\rm FeS_m}$, which is a far more limited subject. Even so it has been the target of several major reviews since it is a key area of biomineralization. $^{199,224,368-370}$

Sulfate-reducing microorganisms produce c.97% of the contemporary Earth surface sulfide and they are intimately related to iron sulfides. Indeed, the blackening of SRP cultures is used by microbiologists as a sign of growth. These iron sulfides are precipitated within the cell, within the cell wall, in the

extracellular proteins (EPS) and as coatings on the cell wall (Figure 24).

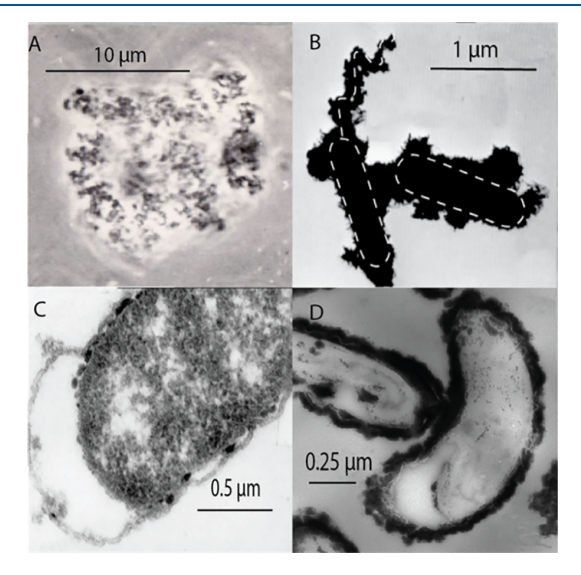


Figure 24. FeS_m coatings of sulfate-reducing bacteria at various magnifications. (A) Classic optical microscope view of a clump blackened D. vulgaris in medium. Adapted with permission from ref 199. Copyright 2012 Elsevier. (B) TEM image of D. vulgaris coated by platy FeS_m crystals in medium. The bacterial cell walls and a flagellum are outlined. Adapted with permission from ref 199. Copyright 2012 Elsevier. (C) Detail of FeS nanoparticles on *D. vulgaris* cell wall and in protoplasm. Adapted with permission from ref 199. Copyright 2012 Elsevier. (D) HRTEM of 80 nm thin section of FeS_m coating *D. hydrothermalis* cells.. Adapted with permission from ref 112. Copyright 2024 Flsevier.

It is reasonable to ask whether this biogenic sulfide produces any different product to abiotic sulfides. There is little evidence for this, and it seems as though the organisms merely produce sulfide which then react with Fe compounds to form FeS_m . The question was addressed experimentally in 1968 and the result was that no differences could be detected between abiologic FeS_m and FeS_m produced in cultures of sulfate-reducing microorganisms. 143,371 Technology has progressed since then and the question has been readdressed. 112,140 These new studies reported that the unit cell parameters for biologic FeS_m and abiotic FeS_m were similar.

EXAFS analyses (Table 29) show that the local Fe environment in biogenic FeS_m matches that for standard, inorganic FeS_m . Have Biologic FeS_m is similar to inorganic FeS_m in displaying a low number of computed Fe neighbors compared to the number expected in the standard mackinawite structure. The number increases with time 140 as the particles grow and this may reflect the development of the square-planar sheets of Fe atoms that are characteristic of crystalline mackinawite (sections 2 and 9) as well as being a function of the quality of the EXAFS data for these nanomaterials. 112

The particle sizes of the biologic FeS_m are about twice the size of abiotic FeS_m , suggesting that the rate of FeS_m particle growth, as well as the rate of crystallization, are catalyzed by bacterial surfaces. ²²³ The increased rate of particle growth on microbial surfaces has been related to the general faster rate of heterogeneous nucleation compared with homogeneous nucleation and the chemistry of microbial surfaces, especially

Table 29. Comparison of Results of Rietveld Refinement of XRPD Analyses and EXAFS Shell-Fitting Results for Standard ${\rm FeS_m}^{11308}$, ${\rm FeS_m}$ after 1 s Aging, 113 and ${\rm FeS_m}$ Precipitated with Microbial Sulfide 140,a

		inorganic		
	FeS _m (XRD)	FeS_m	$FeS_{m}(1 s)$	Bio-FeS
Fe-S (Å)	2.26	2.26	2.24	2.24
Fe-Fe (Å)	2.60	2.56	2.59	2.62
N(S)	4	4.0	3.8	4.0
N(Fe)	4	4.0	2.0	0.9

"The first shell Fe-S and second shell Fe-Fe distances, (Å), and the coordination numbers for S, N(S), and Fe, N(Fe), are listed. Compare Table 18.

the abundance of negatively charged carboxyl groups (COO-) which bind metal cations. ^{224,372}

However, the precise composition of the biological FeS_m has not been determined although element ratios have been reported (Table 30). The methods noted in Table 30 include

Table 30. Reported Fe:S Ratios of Biogenic FeS_m, Experimental Temperatures, Analytical Methods (See Text)

Fe:S	total (wt %)	temperature	method	
1.01	85.2	45 °C	wet chemical	373
1.35	59.8	22 °C	wet chemical	373
0.88	n/a	30 °C	wet chemical difference	112
0.84	n/a	30 °C	wet chemical difference	112
1.37	n/a	35 °C	EDX	140

(1) wet chemical, where both the cells and the FeS precipitate is dissolved in 20% HCl and the evolved Fe and S contents are measured directly; (2) wet chemical difference where the Fe:S ratio of FeS_m is the difference between the Fe and S contents in the supernatant and the totals in the cells and FeS precipitate; (3) EDX where the software corrects the results to give 100% totals. The analytical chemistry of FeS_m and mackinawite has been discussed in detail and the reason these methods give imprecise results have been identified. The resolution of analytical protocols for the precise determination of the composition of biologic FeS_m may be significant since it is possible that FeS_m growing in close proximity to cell walls and EPS might sequester organic compounds between the interlayer spaces in the structure, as described for synthetic interlayer FeS_m compounds in section 4.

The interaction of nucleic acids with nanoparticulate FeS_m was first reported in 2008. This study investigated the reaction between nanoparticulate FeS_m and wild DNA, chromosomal DNA (cDNA), oligomeric DNA (oDNA), RNA, and the DNA monomers, deoxyadenosine monophosphate (dAMP), deoxyadenosine and adenine. The results showed that the degree to which these molecules were sedimented with FeS_m was proportional to the relative size of the nucleotides: cDNA > RNA > oDNA > DNA monomers. The nanoparticles were up to 1000x smaller than the largest polynucleotide molecules and these FeS_m nanoparticles attached to several sites on the nucleotide molecules. The interaction between FeS_m and nucleic acids was shown to involve more than just electrostatic interactions.

Plasmid DNA (pDNA) uncoils after reaction with FeS_m (Figure 25). 366 Note that the FeS nanoparticles are about 2 nm in size and are much smaller than the ca. 300 nm DNA

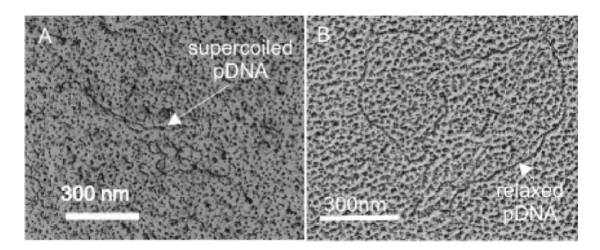


Figure 25. HRTEM images of the effect of FeS nanoparticles on plasmid DNA (pDNA). (A) Original supercoiled DNA. (B) Relaxed pDNA after reaction with FeS nanoparticles. Reproduced with permission from ref 366. Copyright 2011 Springer.

molecules, so that many of these nanoparticles attach to the larger DNA molecules. The uncoiling is caused by nicking, that is the removal of a phosphodiester bond between adjacent nucleotides. It was concluded 366 that the reaction involved free radicals, possibly the highly transient HS \bullet radicals discussed in section 12.4. DNA supercoiling affects nearly all DNA—protein interactions so the relaxation of supercoiled forms on reaction with FeS $_{\rm m}$ will affect plasmids in sediments. Interactions of these mobile elements with organisms in sulfidic systems may contribute to the develop of mutant forms in sulfidic systems and consequently to organic evolution.

 ${\rm FeS_m}$ nanoparticles are genotoxic. They cause alterations to genes related to immune and inflammatory responses, detoxification, oxidative stress and DNA repair. The results may explain the observation that ${\rm FeS_m}$ coatings of sulfate-reducing bacterial cells (Figure 24) is a sign of a declining culture: the cells in healthy cultures with well-developed extracellular polysaccharides remain essentially ${\rm FeS_m}$ -free. The organisms appear to have evolved a mechanism for keeping genotoxic ${\rm FeS_m}$ out of their cells.

13. SUMMARY AND PERSPECTIVES

After being stranded in the backwaters of chemical research for decades, the chemistry of the simple binary material, tetragonal FeS_m, the synthetic equivalent of the mineral mackinawite, has become a fast-growing field at the frontiers of chemical research. The reasons are 2-fold and probably interrelated. First, recent advances in the technology of probing the structure and chemistry of nanoparticulate materials have meant that the nature of these familiar, black, quasi-amorphous nanoprecipitates is becoming better understood. This has also contributed to advances in the general understanding of the chemistry and thermodynamics of nanoparticles, including surface chemistry, particle and crystal growth mechanisms, nucleation processes especially in aqueous media, the synthesis of unstable and highly sensitive materials, and the organic and biological chemistry of inorganic nanoparticles. Second, these materials have become of key interest to industry and the environment. Advances in understanding the electrical and magnetic structures of FeS_m have been encouraged by the discovery that the material shows superconducting properties and belongs to a class of unconventional superconductors, raising the possibility of manufacturing cheap, FeS_m-based superconducting materials. This has led to further advances in the syntheses of layered chalcogenides with exotic compounds in the vdW spaces between the FeS layers. FeS_m displays a strong tendency to sequester both inorganic (e.g., As) and organic (e.g., halogenated hydrocarbons) species which has led to extensive studies of its surface chemistry with a view to using this inexpensive material to remove or transform

environmental pollutants. This in turn has encouraged the synthesis of different means of delivering FeS_m nanoparticles to the environment by dispersing them in porous materials or stabilizing them with surfactants and polymers.

Future research in FeS_m needs to address the following aspects:

- Analytical approaches to determining the composition of FeS_m need to be urgently improved. Fine tuning the composition may be important in developing superconductivity in FeS_m and merely reporting Fe:S ratios, with no real totals, is not sufficient.
- FeS_m is one of a spectrum of nanoparticulate iron sulfides and the interspecies transformations of these compounds are influenced by the differential surface energy contributions to the total reaction free energy leading to the possibility of reversing the anticipated equilibration reactions
- The syntheses of FeS_m need to be standardized so that the results are not empirical. The new synthesis route based on using interlayered varieties of FeS_m and removing the interlayer material is very promising. The standardization of the reactant material is needed for any industrial application of the material as well as being significant in interrogating its electrical and magnetic properties.
- The organic chemistry of FeS_m is in its infancy. The original exploration of organic reactions with FeS_m with samples of wild organic matter identified many thousands of organic compounds which may react with this material. Systematic investigations of the reactions of FeS_m with organics will lead to new reactions and new processes.
- The biological chemistry of FeS_m needs to be urgently addressed. There are conflicting data about the genotoxicity of the material and this needs to be resolved if manufactured FeS_m nanoparticles are planned to be distributed into the environment for pollution control purposes. This becomes even more pertinent if these nanoparticles are injected as carriers for medical purposes.
- The environmental use of FeS_m particles for pollution control seems to be limited by the inability to detect, define and collect natural FeS_m in sediments. This is a perennial problem and one that has not progressed since it was identified as a stumbling block by the founders of the study of FeS_m over 70 years ago.

AUTHOR INFORMATION

Corresponding Author

David Rickard — School of Earth and Environmental Sciences, Cardiff University, Cardiff CF10 3AT Wales, U.K.;

orcid.org/0000-0002-4632-5711; Email: rickard@cardiff.ac.uk

Complete contact information is available at: https://pubs.acs.org/10.1021/acs.chemrev.5c00763

Notes

The author declares no competing financial interest.

Biography

David Rickard started sulfide chemistry research as a senior undergraduate at Imperial College, London in 1965, with a thesis on pyrite framboids and published his first paper in 1966. He has since published over 300 research papers and 5 books. Following a period as a

Research Professor (Forskardocent) with the Swedish NSF (NFR) based at the University of Stockholm, Sweden, he was appointed Professor in Cardiff University in 1983 and Emeritus in 2010. His latest interests have involved characterizing nanoparticulate metal sulfides and their interactions with biochemical molecules, including nucleic acid polymers. He has been awarded Fellowships of the Geochemical Society, the European Association of Geochemistry, and the Society of Geology Applied to Mineral Deposits, and been elected to Fellowships of the Royal Chemical Society, the Royal Biological Society, the Geological Society of London and the Learned Society of Wales.

ACKNOWLEDGMENTS

This wide-ranging review could not have been completed without the inputs of many colleagues at various stages of manuscript preparation. I thank Ian Butler, Edinburgh, UK; Laurent Charlet, Grenoble, France; Amy Gartman, Santa Cruz, CA,USA; Hoon Jeong, Busan, South Korea; Amy Kan, Houston, TX, USA; Dimo Kaschiev, Sofia, Bulgaria; George Luther III, Lewes, DE, USA; Yuri Mikhlin, Ramat Gan, Israel; James Murowchick, Kansas City, Mo, USA; Damien Murphy, Cardiff, UK; Massimo Nespolo, Nancy, France; Anthony Oldroyd, Cardiff, UK; Mihàly Pósfai, Veszprém, Hungary; Rob Raiswell, Leeds, UK; Marc Singer, Athens, OH, USA; Stephen Smith, Colorado Springs, CO, USA; Wolfgang Wegand, Jena, Germany; Mariette Wolthers, Utrecht, Netherlands and David Young, Athens, OH, USA.

REFERENCES

- (1) Berzelius, J. J. Försök till ett rent kemiskt mineralsystem. Afhandlingar i fysik, kemi och mineralogi 1815, 4, 1–147.
- (2) Rickard, D. The composition of mackinawite. *Am. Mineral.* **2024**, 109 (3), 401–407.
- (3) Meyer, F. H.; Riggs, O. L.; McGlasson, R. L.; Sudbury, J. D. Corrosion products of mild steel in hydrogen sulfide environments. *Corrosion* 1958, 14 (2), 69–75.
- (4) Berner, R. A. Tetragonal iron sulfide. Science 1962, 137 (3531), 669.
- (5) Mellor, J. W. A Comprehensive Treatise on Inorganic and Theoretical Chemistry; Longmans Green, 1935.
- (6) Cotton, F. A.; Wilkinson, G. Advanced Inorganic Chemistry: A Comprehensive Text; Interscience Publishers, 1963.
- (7) Rose, H. Handbuch der Analytischen Chemie; Mittler, 1829.
- (8) Fresenius, C. R. Anleitung zur qualitativen chemischen Analyse oder die Lehre von den Operationen, von den Reagentien, und von dem Verhalten der bekannteren Körper zu Reagentien für Anfänger und Geübtere; Vieweg, 1841
- (9) Vogel, A. I. a Text Book of Quantitative Inorganic Analysis; Longmans, Green, 1939.
- (10) Buchanan, J. Y. On the occurrence of sulphur in marine muds and nodules, and its bearing on their mode of formation. *Proc. R. Soc. Edinburgh* **1892**, *18*, 17–39.
- (11) Šiderenko, M. Petrograficheskie danniye po sovremennym otlozheniyam v Khadzhibeiskom limane I o litologicheskom sostave poverkhnostnykh osadkov Kuyal'nitsko-Kadzhibeiskoy Peresipi. *Mem. Soc. Nat. Nouvelle-Russie (Odessa)* **1901**, *24*, 97–119.
- (12) Rickard, D.; Griffith, A.; Oldroyd, A.; Butler, I. B.; Lopez-Capel, E.; Manning, D. A. C.; Apperley, D. C. The composition of nanoparticulate mackinawite, tetragonal iron(II) monosulfide. *Chem. Geol.* **2006**, 235 (3–4), 286–298.
- (13) Doss, B. Melnikovit, ein neues Eisenbisulfid, und seine Bedeuting für Genesis der Kieslagerstatten. Z. Prakt. Geologie 1912, 20, 453–483.
- (14) Ramdohr, P. The Ore Minerals and Their Intergrowths; Pergamon, 1980.
- (15) Birks, L. S.; Brooks, E. J.; Adler, I.; Milton, C. Electron probe analysis of minute inclusions of a copper-iron mineral. *Am. Mineral.* **1959**, 44 (9–10), 974–978.

- (16) Milton, C.; Milton, D. J. Nickel-gold ore of the Mackinaw mine, Snohomish County, Washington. *Econ. Geol.* **1958**, *53*, 426–447.
- (17) Kuovo, O.; Vuorelainen, Y.; Long, J. V. P. A tetragonal iron sulfide. *Am. Mineral.* **1963**, 48, 511–524.
- (18) Evans, H. T.; Milton, C.; Chao, E. C. T.; Adler, I.; Mead, C.; Ingram, B.; Berner, R. A. Valleriite and the new iron sulfide, mackinawite. *USGS Prof. Pap.* **1964**, *475D*, 133.
- (19) Ohfuji, H.; Rickard, D. High resolution transmission electron microscopic study of synthetic nanocrystalline mackinawite. *Earth Planet. Sci. Lett.* **2006**, 241 (1–2), 227–233.
- (20) Rickard, D.; Luther, G. W. Chemistry of iron sulfides. *Chem. Rev.* **2007**, *107* (2), 514–562.
- (21) Wolthers, M.; Van Der Gaast, S. J.; Rickard, D. The structure of disordered mackinawite. *Am. Mineral.* **2003**, *88*, 2007–2015.
- (22) Li, P.; Zhang, W. C.; Hu, F.; Ye, J. F.; Xu, Z. X. The amorphous mackinawite produced during the blackening of hypoxic waters: determination methods, generation process, and existing patterns. *Reviews in Environmental Science and Bio-Technology* **2022**, 21 (4), 1017–1033.
- (23) Lennie, A. R.; Redfern, S. A. T.; Schofield, P. F.; Vaughan, D. J. Synthesis and Rietveld crystal structure refinement of mackinawite, tetragonal FeS. *Mineral. Mag* **1995**, *59*, *677*–*683*.
- (24) Haase, F. J.; Vessey, C. J.; Sekine, R.; Doriean, N. J. C.; Welsh, D. T.; Otte, J. A.; Hamilton, J.; Canfield, D. E.; Wang, Y.; Lombi, E. Reductive sorption of vanadium by iron monosulfide in seawater. *Chem. Geol.* 2024, 649, 121983.
- (25) Uda, M. Structure of tetragonal FeS. Z. Phys. Chem. 1968, 361 (1-2), 94-98.
- (26) Taylor, L. A.; Finger, L. W. Structural refinement and composition of mackinawite. *Carnegie Inst. Washington, Yearb.* **1970**, 69, 318–322.
- (27) Lennie, A. R.; Redfern, S. A. T.; Champness, P. E.; Stoddart, C. P.; Schofield, P. F.; Vaughan, D. J. Transformation of mackinawite to greigite: An in situ X-ray powder diffraction and transmission electron microscope study. *Am. Mineral.* **1997**, *82* (3–4), 302–309.
- (28) Mullet, M.; Boursiquot, S.; Abdelmoula, M.; Génin, J. M.; Ehrhardt, J. J. Surface chemistry and structural properties of mackinawite prepared by reaction of sulfide ions with metallic iron. *Geochim. Cosmochim. Acta..* 2002, 66 (5), 829–836.
- (29) Jeong, H. Y.; Lee, J. H.; Hayes, K. F. Characterization of synthetic nanocrystalline mackinawite: Crystal structure, particle size, and specific surface area. *Geochim. Cosmochim. Acta. 2.* **2008**, 72 (2), 493–505.
- (30) Bolney, R.; Grosch, M.; Winkler, M.; van Slageren, J.; Weigand, W.; Robl, C. Mackinawite formation from elemental iron and sulfur. *RSC Adv.* **2021**, *11* (51), 32464–32475.
- (31) Borg, C. K. H.; Zhou, X.; Eckberg, C.; Campbell, D. J.; Saha, S. R.; Paglione, J.; Rodriguez, E. E. Strong anisotropy in nearly ideal tetrahedral superconducting FeS single crystals. *Phys. Rev. B.* **2016**, *93* (9), 094522.
- (32) Murowchick, J. B.; Oldroyd, A.; Rickard, D. Molecular mechanism of the sulfide corrosion of α -iron. *Corros. Sci.* **2024**, 231, 111949.
- (33) Nespolo, M. Lattice versus structure, dimensionality versus periodicity: a crystallographic Babel? *J. Appl. Crystallogr.* **2019**, 52, 451–456.
- (34) Balisetty, L.; Wilfong, B.; Zhou, X.; Zheng, H.; Liou, S.-C.; Rodriguez, E. E. Twisting two-dimensional iron sulfide layers into coincident site superlattices via intercalation chemistry. *Chem. Sci.* 2024.
- (35) Bourdoiseau, J. A.; Jeannin, M.; Sabot, R.; Rémazeilles, C.; Refait, P. Characterisation of mackinawite by Raman spectroscopy: Effects of crystallisation, drying and oxidation. *Corros. Sci.* **2008**, *50* (11), 3247–3255.
- (36) Csákberényi-Malasics, D.; Rodriguez-Blanco, J. D.; Kis, V. K.; Recnik, A.; Benning, L. G.; Pósfai, M. Structural properties and transformations of precipitated FeS. *Chem. Geol.* **2012**, 294, 249–258.

- (37) He, Y. T.; Wilson, J. T.; Wilkin, R. T. Impact of iron sulfide transformation on trichloroethylene degradation. *Geochim. Cosmochim. Acta* **2010**, 74 (7), 2025–2039.
- (38) Kwon, K. D.; Refson, K.; Sposito, G. Transition metal incorporation into mackinawite (tetragonal FeS). *Am. Mineral.* **2015**, 100 (7), 1509–1517.
- (39) Devey, A. J.; Grau-Crespo, R.; de Leeuw, N. H. Combined density functional theory and interatomic potential study of the bulk and surface structures and properties of the iron sulfide mackinawite (FeS). J. Phys. Chem. C. 2008, 112 (29), 10960–10967.
- (40) Subedi, A.; Zhang, L.; Singh, D. J.; Du, M. H. Density functional study of FeS, FeSe, and FeTe: Electronic structure, magnetism, phonons, and superconductivity. *Phys. Rev. B* **2008**, 78 (13), 134514.
- (41) Zeng, S. L.; Wang, H. X.; Dong, C. Synthesis and electrical conductivity of nanocrystalline tetragonal FeS. *Chin. Phys. B* **2014**, 23 (8), 087203.
- (42) Denholme, S. J.; Demura, S.; Okazaki, H.; Hara, H.; Deguchi, K.; Fujioka, M.; Ozaki, T.; Yamaguchi, T.; Takeya, H.; Takano, Y. Evidence for non-metallic behaviour in tetragonal FeS (mackinawite). *Mater. Chem. Phys.* **2014**, *147* (1–2), 50–56.
- (43) Denholme, S. J.; Okazaki, H.; Demura, S.; Deguchi, K.; Fujioka, M.; Yamaguchi, T.; Takeya, H.; El Massalami, M.; Fujiwara, H.; Wakita, T.; et al. Pressure-dependent magnetization and magnetoresistivity studies on tetragonal FeS (mackinawite): revealing its intrinsic metallic character. Sci. Technol. Adv. Mater. 2014, 15 (5), 055007.
- (44) Vaughan, D. J.; Ridout, M. S. Mössbauer studies of some sulphide minerals. J. Inorg. & Nucl. Chem. 1971, 33, 741–746.
- (45) Morice, J.; Rees, L.; Rickard, D. Mössbauer studies of iron sulphides. J. Inorg. & Nucl. Chem. 1969, 31, 3797–3802.
- (46) Schroeder, C.; Wan, M.; Butler, I. B.; Tait, A.; Peiffer, S.; McCammon, C. A. Identification of mackinawite and constraints on its electronic configuration using Mössbauer spectroscopy. *Minerals.* **2020**, *10* (12), 1090.
- (47) Boursiquot, S.; Mullet, M.; Abdelmoula, M.; Genin, J.-M.; Ehrhardt, J.-J. The dry oxidation of tetragonal FeS_{1-x}mackinawite. *Phys. Chem. Miner.* **2001**, 28 (9), 600–611.
- (48) Bertaut, E. F.; Burlet, P.; Chappert, J. Regarding the absence of magnetic order in quadratic forms of FeS. *Solid State Commun.* **1965**, 3 (10), 335–338.
- (49) Kwon, K. D.; Refson, K.; Bone, S.; Qiao, R.; Yang, W.-l.; Liu, Z.; Sposito, G. Magnetic ordering in tetragonal FeS: Evidence for strong itinerant spin fluctuations. *Phys. Rev. B* **2011**, 83 (6), 064402.
- (50) Moriya, T. Spin Fluctuations in Itinerant Electron Magnetism; Springer, 1985.
- (51) Rasaki, S. A.; Thomas, T.; Yang, M. Iron based chalcogenide and pnictide superconductors: From discovery to chemical ways forward. *Prog. Solid State Chem.* **2020**, *59*, 100282.
- (\$\(\frac{5}{2}\) Lai, X.; Zhang, H.; Wang, Y.; Wang, X.; Zhang, X.; Lin, J.; Huang, F. Observation of superconductivity in tetragonal FeS. *J. Am. Chem. Soc.* **2015**, *137* (32), 10148–10151.
- (53) Lin, H.; Li, Y.; Deng, Q.; Xing, J.; Liu, J.; Zhu, X.; Yang, H.; Wen, H.-H. Multiband superconductivity and large anisotropy in FeS crystals. *Phys. Rev. B* **2016**, 93 (14), 144505.
- (54) Kuhn, S. J.; Kidder, M. K.; Parker, D. S.; dela Cruz, C.; McGuire, M. A.; Chance, W. M.; Li, L.; Debeer-Schmitt, L.; Ermentrout, J.; Littrell, K. C.; et al. Structure and property correlations in FeS. *Phys. C (Amsterdam, Neth.)* **2017**, 534, 29–36.
- (55) Man, H.; Guo, J.; Zhang, R.; Schönemann, R.; Yin, Z.; Fu, M.; Stone, M. B.; Huang, Q.; Song, Y.; Wang, W.; et al. Spin excitations and the Fermi surface of superconducting FeS. *npj Quantum Mater.* **2017**, 2 (1), 14.
- (56) Miao, J.; Niu, X. H.; Xu, D. F.; Yao, Q.; Chen, Q. Y.; Ying, T. P.; Li, S. Y.; Fang, Y. F.; Zhang, J. C.; Ideta, S.; et al. Electronic structure of FeS. *Phys. Rev. B* **2017**, *95* (20), 205127.
- (57) Xie, W.; Zheng, F.; Xu, H. S. Hydrothermal synthesis of tetragonal FeS: Dome-shaped superconductivity vs Fe:S actual molar ratios. *J. Appl. Phys.* **2024**, *136* (4), 043903.
- (58) Tresca, C.; Giovannetti, G.; Capone, M.; Profeta, G. Electronic properties of superconducting FeS. *Phys. Rev. B* **2017**, *95* (20), 205117.

- (59) Bardeen, J.; Cooper, L. N.; Schrieffer, J. R. Theory of superconductivity. *Phys. Rev.* **1957**, *108* (5), 1175–1204.
- (60) Si, Q. M.; Yu, R.; Abrahams, E. High-temperature superconductivity in iron pnictides and chalcogenides. *Nat. Rev. Mater.* **2016**, *1* (4), 16017.
- (61) He, S.; He, J.; Zhang, W.; Zhao, L.; Liu, D.; Liu, X.; Mou, D.; Ou, Y.-B.; Wang, Q.-Y.; Li, Z.; Wang, L.; Peng, Y.; Liu, Y.; Chen, C.; Yu, L.; Liu, G.; Dong, X.; Zhang, J.; Chen, C.; Xu, Z.; Chen, X.; Ma, X.; Xue, Q.; Zhou, X. J. Phase diagram and electronic indication of high-temperature superconductivity at 65 K in single-layer FeSe films. *Nat. Mater.* 2013, 12 (7), 605–610.
- (62) Yang, H.; Zhou, Y.; Miao, G.; Xu, X.; Han, X.; Zhu, X. X.; Guo, J.; Wu, R.; Pan, X. Role of substrate phonon in the electron-phonon coupling at FeSe/SrTiO₃ interface. *Microsc. Microanal* **2023**, *29*, 1629–1630
- (63) Kirschner, F. K. K.; Lang, F.; Topping, C. V.; Baker, P. J.; Pratt, F. L.; Wright, S. E.; Woodruff, D. N.; Clarke, S. J.; Blundell, S. J. Robustness of superconductivity to competing magnetic phases in tetragonal FeS. *Phys. Rev. B* **2016**, *94* (13), 134509.
- (64) Holenstein, S.; Pachmayr, U.; Guguchia, Z.; Kamusella, S.; Khasanov, R.; Amato, A.; Baines, C.; Klauss, H. H.; Morenzoni, E.; Johrendt, D.; et al. Coexistence of low-moment magnetism and superconductivity in tetragonal FeS and suppression of T_c under pressure. *Phys. Rev. B* **2016**, 93 (14), 140506.
- (65) Sweeney, R. E.; Kaplan, I. R. Pyrite framboid formation: Laboratory synthesis and marine sediments. *Econ. Geol.* **1973**, *68*, 618–634.
- (66) Rickard, D. T. The chemistry of iron sulphide formation at low temperatures. *Stockholm Cont. Geology* **1969**, 20 (4), 67–95.
- (67) Ward, J. C. The structure and properties of some iron sulphides. Rev. Pure Appl. Chem. 1970, 20, 175–206.
- (68) Allen, R. E.; Parkes, R. J. Digestion procedures for determining reduced sulfur species in bacterial cultures and in ancient and recent sediments. *Geochemical Transformations of Sedimentary Sulfur*; ACS Symp. Ser.; American Chemical Society, 1995; Vol. 612, pp 243–257.
- (69) Polushkina, A. P.; Sidorenko, G. A. Melnikovit dolzhen schitatsia opredelennym mineralnym vidom. *Zapiski VMO* **1963**, *92*, 547–554.
- (70) Rickard, D. Metal sequestration by sedimentary iron sulfides. Sulfidic Sediments and Sedimentary Rocks. Elsevier. 2012.
- (71) Kornicker, W. A. Interactions of divalent cations with pyrite and mackinawite in seawater and NaCl solutions. *PhD Thesis*. Texas A&M University, 1988.
- (72) Siderenko, M. Petrograficheskie danniye po sovremennym otlozheniyam v Khadzhibeiskom limane I o litologicheskom sostave poverkhnostnykh osadkov Kuyal'nitsko-Kadzhibeiskoy Peresipi. Zap. Novorossiiskago Obshchestva Estestvoispytatelei (Odessa) 1901, 24, 97–119
- (73) Luther, G.; Rickard, D. Metal sulfide cluster complexes and their environmental significance. *Geochim. Cosmochim. Acta* **2004**, *68* (11), A217.
- (74) Voigt, B.; Moore, W.; Maiti, M.; Walter, J.; Das, B.; Manno, M.; Leighton, C.; Aydil, E. S. Observation of an internal p-n Junction in pyrite FeS₂ single crystals: Potential origin of the low open circuit voltage in pyrite solar cells. *ACS Mater. Lett.* **2020**, *2* (7), 861–868.
- (75) Vaughan, D. J.; Craig, J. R. Mineral Chemistry of Metal Sulfides Cambridge University Press, 1978.
- (76) Hsu, F. C.; Luo, J. Y.; Yeh, K. W.; Chen, T. K.; Huang, T. W.; Wu, P. M.; Lee, Y. C.; Huang, Y. L.; Chu, Y. Y.; Yan, D. C.; et al. Superconductivity in the PbO-type structure α -FeSe. *Proc. Natl. Acad. Sci. U. S. A. America* **2008**, *105* (38), 14262–14264.
- (77) Lei, H. C.; Abeykoon, M.; Bozin, E. S.; Wang, K. F.; Warren, J. B.; Petrovic, C. Phase dagram of $K_x Fe_{2-y} Se_{2-z} S_z$ and the suppression of its superconducting state by an Fe2-Se/S tetrahedron distortion. *Phys. Rev. Lett.* **2011**, *107* (13), 137002.
- (78) Wu, D.; Guo, Z. N.; Liu, N.; Zhou, L.; Mao, Y. L.; Wan, L.; Sun, F.; Yuan, W. X. A new intercalated iron sulfide $(C_2H_8N_2)_{0.4}Fe_2S_2$ from solvothermal route: Synthesis, structure and tunable magnetism. *Inorg. Chem. Commun.* **2018**, *91*, 72–76.

- (79) Harmer, C. P.; Kamali, S.; Lebedev, O. I.; Lee, S. J.; Ribeiro, R. A.; Canfield, P. C.; Kovnir, K. Pseudo-polymorphism in layered FeS intercalates: A competition between charged and neutral guest species. *Chem. Mater.* **2022**, *34* (12), 5397–5408.
- (80) Zhou, X. Q.; Eckberg, C.; Wilfong, B.; Liou, S. C.; Vivanco, H. K.; Paglione, J.; Rodriguez, E. E. Superconductivity and magnetism in iron sulfides intercalated by metal hydroxides. *Chem. Sci.* **2017**, *8* (5), 3781–3788.
- (81) Lei, H.; Abeykoon, M.; Bozin, E. S.; Petrovic, C. Spin-glass behavior of semiconducting K_xFe_{2-y}S₂. *Phys. Rev. B* **2011**, 83 (18), 180503.
- (82) Guo, M.; Lai, X.; Tan, X.; Xiao, M.; Wu, R.; Jian, J. Hydrazine intercalated iron sulfide $(N_2H_4)_{1-x}Fe^{2+}\delta S_2$: Synthesis and characterization. *J. Solid State Chem.* **2021**, 303, 122507.
- (83) Harmer, C. P.; Pak, C.; Greenfield, J. T.; Adeyemi, A. N.; Gamage, E. H.; Kovnir, K. Non-innocent intercalation of diamines into tetragonal FeS superconductor. ACS Appl. Energy Mater. 2021, 4 (1), 42–46.
- (84) Zheng, H. F.; Wilfong, B. C.; Hickox-Young, D.; Rondinelli, J. M.; Zavalij, P. Y.; Rodriguez, E. E. Polar ferromagnetic metal by intercalation of metal-amine complexes. *Chem. Mater.* **2021**, 33 (13), 4936–4947.
- (85) Organova, N. I.; Genkin, A. D.; Drits, V. A.; Dmitrik, A. L.; Kuzima, O. V. Tochilinite, a new iron and magnesium sulfide-hydroxide (Tochilinit-novyi sulfid-gidrookisel zheleza i magniya). *Zap. VMO* **1971**, *4*, 477–487.
- (86) Mackinnon, I. D. R.; Zolensky, M. E. Proposed structures for poorly characterized phases in C2M carbonaceous chondrite meteorites. *Nature* **1984**, 309 (5965), 240–242.
- (87) Mikhlin, Y.; Likhatski, M.; Borisov, R.; Karpov, D.; Vorobyev, S. Metal chalcogenide-hydroxide hybrids as an emerging family of two-dimensional heterolayered materials: An early review. *Materials* **2023**, *16*, 6381
- (88) Pekov, I. V.; Sereda, E. V.; Polekhovsky, Y. S.; Britvin, S. N.; Chukanov, N. V.; Yapaskurt, V. O.; Bryzgalov, I. A. Ferrotochilinite, 6FeS·5Fe(OH)₂, a new mineral from the Oktyabr'sky deposit, Noril'sk district, Siberia, Russia. *Geology of Ore Deposits* **2013**, 55 (7), 567–574.
- (89) Organova, N. I.; Drits, V. A.; Dmitrik, A. L. Structure study of tochilinite.2. Needle-shaped variety—unusual diffraction patterns. *Kristallografiya* **1973**, *18* (5), 966–972.
- (90) Fleischer, M. New Mineral Names. Am. Mineral. 1972, 57, 1552–1561.
- (91) Bolney, R.; Grosch, M.; Winkler, M.; van Slageren, J.; Weigand, W.; Robl, C. Facile synthesis and characterization of pure tochilinite-like materials from nanoparticulate FeS. *Z. Phys. Chem.* **2022**, *648* (23), e202200219.
- (92) Organova, N. I.; Drits, V. A.; Dmitrik, A. L. Structure study of tochilinite-II: an acicular variety and unusual diffraction patterns. *Sov. Phys., Crystallogr.* **1974**, *18*, 605–609.
- (93) Organova, N. I.; Drits, V. A.; Dmitrik, A. L. Selected area electron diffraction study of a type II "valleriite-like" mineral. *Am. Mineral.* **1974**, 59 (1–2), 190–200.
- (94) Blomstrand, C. W. On some new Swedish minerals and the composition of pyrrhotite. Öfversigt Kong. Vetenskaps-Akademiens Förh., Stockholm. 1870, 27, 19–27.
- (95) Evans, H. T.; Allmann, R. Crystal structure and crystal chemistry of valleriite. *Z. Kristallogr. Krist.* **1968**, *127* (1–4), 73–93.
- (96) Rice, C. M.; Atkin, D.; Bowles, J. F. W.; Criddle, A. J. Nukundamite, a new mineral, and idaite. *Miner. Mag.* **1979**, 43 (326), 193–200.
- (97) Huhma, M.; Vuorelainen, Y.; Hakli, T. A.; Papunen, H. Haapalaite, a new nickel-iron sulphide of the valleriite type from East Finland. *Bull. Geol.Soc. Finland* 1973, 45, 103–106.
- (98) Soboleva, S. V.; Boeva, N. M.; Evstigneeva, T. E.; Bortnikov, N. S. The crystal structure of vyalsovite FeCaAlS(OH)₅: First example of the commensurate combination of iron sulfide and hydroxide layers. *Dokl. Earth Sci.* **2022**, 503 (2), 164–167.

- (99) Evstigneeva, T. L.; Genkin, A. D.; Sandomirskaya, S. M.; Trubkin, N. V. Vyalsovite, a new sulfide-hydroxide of iron, calcium, and aluminum. *Am. Mineral.* **1992**, *77* (1–2), 201–206.
- (100) Soboleva, S. V.; Evstigneeva, T. E.; Boeva, N. M.; Bortnikov, N. S. Crystal structure of yushkinite $[(Mg_{0.60}Al_{0.30}V_{0.10})\Sigma 1.0(OH)_2]$ - $[V_{0.875}S_2]$: An example of a commensurate combination of brucite and sulfide layers. *Dokl. Earth Sci.* **2020**, 491 (2), 210–213.
- (101) Makeev, A. B.; Evstigneeva, T. L.; Troneva, N. V.; Vyalsov, L. N.; Gorshkov, A. L.; Trubkin, N. V. Yushkinite V1-[Mg,Al)(OH)₂]–A new mineral. *Mineral. Zhurnal* **1984**, *6*, 91–98.
- (102) Pekov, I. V.; Yapaskurt, V. O.; Polekhovsky, Y. S.; Vigasina, M. F.; Siidra, O. I. Ekplexite (Nb,Mo)S₂·(Mg_{1-x}Al_x)(OH)_{2+x}, kaskasite (Mo,Nb)S₂·(Mg_{1-x}Al_x)(OH)_{2+x} and manganokaskasite (Mo,Nb)S₂·(Mn_{1-x}Alx)(OH)_{2+x}, three new valleriite-group mineral species from the Khibiny alkaline complex, Kola peninsula, Russia. *Mineral. Mag.* **2014**, 78 (3), 663–679.
- (103) McCollom, T. M.; Hoehler, T.; Fike, D. A.; Houghton, J. L.; Bell, A.; Klein, F.; Moskowitz, B.; Solheid, P. Formation of mixed-layer sulfide-hydroxide minerals from the tochilinite-valleriite group during experimental serpentinization of olivine. *Am. Mineral.* **2024**, *109* (1), 61–72.
- (104) Liu, Y.-Y.; Xu, L.; Guo, X.-T.; Lv, T.-T.; Pang, H. Vanadium sulfide based materials: synthesis, energy storage and conversion. *J. Mater. Chem.A* **2020**, *8* (40), 20781–20802.
- (105) Sanden, S. A.; Szilagyi, R. K.; Li, Y. M.; Kitadai, N.; Webb, S. M.; Yano, T.; Nakamura, R.; Hara, M.; McGlynn, S. E. Electrochemically induced metal- vs. ligand-based redox changes in mackinawite: Identification of a Fe³⁺- and polysulfide-containing intermediate. *Dalton Trans.* **2021**, *50* (34), 11763–11774.
- (106) Matamoros-Veloza, A.; Cespedes, O.; Johnson, B. R. G.; Stawski, T. M.; Terranova, U.; de Leeuw, N. H.; Benning, L. G. A highly reactive precursor in the iron sulfide system. *Nat. Commun.* **2018**, *9*, 3125.
- (107) Posfai, M.; Buseck, P. R.; Bazylinski, D. A.; Frankel, R. B. Iron sulfides from magnetotactic bacteria: Structure, composition, and phase transitions. *Am. Mineral.* **1998**, 83 (11–12), 1469–1481.
- (108) Wang, C. L.; Li, W. J.; Zhang, Z. H.; Lei, D. S.; Che, G. Q.; Gou, C. L.; Zhang, J.; Hao, Z. P. A novel iron sulfide phase with remarkable hydroxyl radical generation capability for contaminants degradation. *Water Res.* **2024**, *251*, 121166.
- (109) Berner, R. A. Iron sulfides formed from aqueous solution at low temperatures and atmospheric pressure. *J. Geol.* **1964**, *72*, 293–306.
- (110) Morse, J.; Millero, F.; Cornwell, J.; Rickard, D. The chemistry of the hydrogen sulfide and iron sulfide systems in natural waters. *Earth-Sci. Rev.* **1987**, 24 (1), 1–42.
- (111) Boncella, A. E.; Sabo, E. T.; Santore, R. M.; Carter, J.; Whalen, J.; Hudspeth, J. D.; Morrison, C. N. The expanding utility of iron-sulfur clusters: Their functional roles in biology, synthetic small molecules, maquettes and artificial proteins, biomimetic materials, and therapeutic strategies. *Coord. Chem. Rev.* **2022**, 453, 214229.
- (112) Picard, A.; Gartman, A.; Clarke, D. R.; Girguis, P. R. Sulfate-reducing bacteria influence the nucleation and growth of mackinawite and greigite. *Geochim. Cosmochim. Acta* **2018**, 220, 367–384.
- (113) Lennie, A. R.; Vaughan, D. Spectroscopic studies of iron sulfide formation and phase relations at low temperatures. In *Mineral Spectroscopy; A Tribute to Roger G. Burns*; Special Pub. 5; The Geochemical Society, 1996; pp 117–131.
- (114) Patterson, R. R.; Fendorf, S.; Fendorf, M. Reduction of hexavalent chromium by amorphous iron sulfide. *Environ. Sci. Technol.* **1997**, *31* (7), 2039–2044.
- (115) Rickard, D.; Luther, G. Kinetics of pyrite formation by the H_2S oxidation of iron(II) monosulfide in aqueous solutions between 25 and 125 °C: The mechanism. *Geochim. Cosmochim. Acta* **1997**, *61* (1), 135–147.
- (116) Michel, F. M.; Antao, S. M.; Chupas, P. J.; Lee, P. L.; Parise, J. B.; Schoonen, M. A. A. Short- to medium-range atomic order and crystallite size of the initial FeS precipitate from pair distribution function analysis. *Chem. Mater.* **2005**, *17* (25), 6246–6255.

- (117) Scheinost, A. C.; Charlet, L. Selenite reduction by mackinawite, magnetite and siderite: XAS characterization of nanosized redox products. *Environ. Sci. Technol.* **2008**, *42* (6), 1984–1989.
- (118) Bourdoiseau, J. A.; Jeannin, M.; Rémazeilles, C.; Sabot, R.; Refait, P. The transformation of mackinawite into greigite studied by Raman spectroscopy. *J. Raman Spectrosc.* **2011**, 42 (3), 496–504.
- (119) Ma, H.; Wang, P.; Thompson, A.; Xie, Q.; Zhu, M.; Teng, H. H.; Fu, P.; Liu, C.; Chen, C. Secondary mineral formation and carbon dynamics during FeS oxidation in the presence of dissolved organic matter. *Environ. Sci. Technol.* **2022**, *56* (19), 14120–14132.
- (120) Choi, J.; Choi, K.; Lee, W. Effects of transition metal and sulfide on the reductive dechlorination of carbon tetrachloride and 1,1,1-trichloroethane by FeS. *J. Hazard. Mater.* **2009**, *162* (2), 1151–1158.
- (121) Badea, S.-L.; Stegarus, D.-I.; Niculescu, V.-C.; Enache, S.; Soare, A.; Ionete, R.-E.; Gori, D.; Höhener, P. Dehalogenation of α -hexachlorocyclohexane by iron sulfide nanoparticles: Study of reaction mechanism with stable carbon isotopes and pH variations. *Sci. Total Environ.* **2021**, *801*, 149672.
- (122) Paknikar, K. M.; Nagpal, V.; Pethkar, A. V.; Rajwade, J. M. Degradation of lindane from aqueous solutions using iron sulfide nanoparticles stabilized by biopolymers. *Sci. Tech. Adv.Mater.* **2005**, *6* (3–4), 370–374.
- (123) Lan, Y.; Butler, E. C. Iron sulfide associated products formed during reductive dechlorination of carbon tetrachloride. *Environ. Sci. Technol.* **2016**, *50* (11), 5489–5497.
- (124) Hyun, S. P.; Hayes, K. F. Abiotic reductive dechlorination of cis-DCE by ferrous monosulfide mackinawite. *Environ. Sci. Pollut. Res.* **2015**, 22 (21), 16463–16474.
- (125) Vessey, C. J.; Lindsay, M. B. J. Aqueous vanadate removal by iron(II)-bearing phases under anoxic conditions. *Environ. Sci. Technol.* **2020**, *54* (7), 4006–4015.
- (126) Nan, J.; Luo, S.; Tran, Q. P.; Fahrenbach, A. C.; Lu, W.-N.; Hu, Y.; Yin, Z.; Ye, J.; Van Kranendonk, M. J. Iron sulfide-catalyzed gaseous CO₂ reduction and prebiotic carbon fixation in terrestrial hot springs. *Nat. Comm.* **2024**, *15* (1), 10280.
- (127) Kim, E.-J.; Murugesan, K.; Kim, J.-H.; Tratnyek, P. G.; Chang, Y.-S. Remediation of trichloroethylene by FeS-coated iron nanoparticles in simulated and real groundwater: Effects of water chemistry. *Ind. Eng. Chem. Res.* **2013**, 52 (27), 9343–9350.
- (128) Ehm, L.; Michel, F. M.; Antao, S. M.; Martin, C. D.; Lee, P. L.; Shastri, S. D.; Chupas, P. J.; Parise, J. B. Structural changes in nanocrystalline mackinawite (FeS) at high pressure. *J. Appl. Crystallogr.* **2009**, *42*, 15–21.
- (129) Bone, S. E.; Bargar, J. R.; Sposito, G. Mackinawite (FeS) reduces mercury(II) under sulfidic conditions. *Environ. Sci. Technol.* **2014**, 48 (18), 10681–10689.
- (130) Kim, S.; Park, T.; Lee, W. Enhanced reductive dechlorination of tetrachloroethene by nano-sized mackinawite with cyanocobalamin in a highly alkaline condition. *J. Environ. Manage.* **2015**, *151*, *378*–385.
- (131) Butler, E. C.; Hayes, K. F. Kinetics of the transformation of halogenated aliphatic compounds by iron sulfide. *Environ. Sci. Technol.* **2000**, *34* (3), 422–429.
- (132) Butler, E. C.; Hayes, K. F. Effects of solution composition and pH on the reductive dechlorination of hexachloroethane by iron sulfide. *Environ. Sci. Technol.* **1998**, 32 (9), 1276–1284.
- (133) Jeong, H. Y.; Hayes, K. F. Reductive dechlorination of tetrachloroethylene and trichloroethylene by mackinawite (FeS) in the presence of metals: Reaction rates. *Environ. Sci. Technol.* **2007**, 41 (18), 6390–6396.
- (134) Butler, E. C.; Hayes, K. F. Kinetics of the transformation of trichloroethylene and tetrachloroethylene by iron sulfide. *Environ. Sci. Technol.* **1999**, 33 (12), 2021–2027.
- (135) Jeong, H. Y.; Hayes, K. F. Reductive dechlorination of tetrachloroethylene and trichloroethylene by mackinawite (FeS) in the presence of metals: Reaction rates. *Environ. Sci. Technol.* **2007**, *41* (18), 6390–6396.
- (136) Liang, X.; Dong, Y.; Kuder, T.; Krumholz, L. R.; Philp, R. P.; Butler, E. C. Distinguishing abiotic and biotic transformation of

- tetrachloroethylene and trichloroethylene by stable carbon isotope fractionation. *Environ. Sci. Technol.* **2007**, *41* (20), 7094–7100.
- (137) Liu, X.; Peng, P. a.; Fu, J.; Huang, W. Effects of FeS on the transformation kinetics of γ -hexachlorocyclohexane. *Environ. Sci. Technol.* **2003**, 37 (9), 1822–1828.
- (138) Boursiquot, S.; Mullet, M.; Abdelmoula, M.; Génin, J. M.; Ehrhardt, J. J. The dry oxidation of tetragonal FeS_{1-x} mackinawite. *Physics and Chemistry of Minerals* **2001**, 28 (9), 600–611.
- (139) Nie, Z.; Wang, N.; Xia, X.; Xia, J.; Liu, H.; Zhou, Y.; Deng, Y.; Xue, Z. Biogenic FeS promotes dechlorination and thus de-cytotoxity of trichloroethylene. *Bioprocess Biosyst. Eng.* **2020**, 43 (10), 1791–1800.
- (140) Ikogou, M.; Ona-Nguema, G.; Juillot, F.; Le Pape, P.; Menguy, N.; Richeux, N.; Guigner, J. M.; Noël, V.; Brest, J.; Baptiste, B.; et al. Long-term sequestration of nickel in mackinawite formed by *Desulfovibrio capillatus* upon Fe(III)-citrate reduction in the presence of thiosulfate. *Appl. Geochem.* **2017**, *80*, 143–154.
- (141) Kenneke, J. F.; Weber, E. J. Reductive dehalogenation of halomethanes in iron- and sulfate-reducing sediments. 1. Reactivity pattern analysis. *Environ. Sci. Technol.* **2003**, *37* (4), 713–720.
- (142) Velimirovic, M.; Larsson, P.-O.; Simons, Q.; Bastiaens, L. Reactivity screening of microscale zerovalent irons and iron sulfides towards different CAHs under standardized experimental conditions. *J. Hazard. Mater.* **2013**, 252–253, 204–212.
- (143) Rickard, D. The chemistry of iron sulphide formation at low temperatures. *Stockholm Contrib. Geology* **1969**, 20 (4), 67–95.
- (144) Benning, L. G.; Wilkin, R. T.; Barnes, H. L. Reaction pathways in the Fe-S system below 100°C. Chem. Geol. 2000, 167 (1–2), 25–51.
- (145) Hyun, S. P.; Davis, J. A.; Sun, K.; Hayes, K. F. Uranium(VI) reduction by iron(II) monosulfide mackinawite. *Environ. Sci. Technol.* **2012**, 46 (6), 3369–3376.
- (146) Wang, C.; Wang, M.; Jiang, J.; Yang, H.; Yang, L.; Shi, W.; Lai, X.; Mo, S.-K.; Barinov, A.; Yan, B.; et al. Electronic structure and spatial inhomogeneity of iron-based superconductor FeS*. *Chin. Phys. B* **2020**, 29 (4), 047401.
- (147) Gong, Y. Y.; Gai, L. S.; Tang, J. C.; Fu, J.; Wang, Q. L.; Zeng, E. Y. Reduction of Cr(VI) in simulated groundwater by FeS-coated iron magnetic nanoparticles. *Sci. Total Environ.* **2017**, *595*, 743–751.
- (148) Sun, Y.; Zhou, X. X.; Lou, Z. M.; Liu, Y.; Fu, R. Q.; Xu, X. H. Functionalized iron-based nano-materials for removal of mercury from aqueoussolution. *Prog. Chem.* **2016**, 28 (8), 1156–1169.
- (149) Zhang, Q. Y.; Guo, W. L.; Yue, X. X.; Liu, Z. H.; Li, X. H. Degradation of rhodamine B using FeS-coated zero-valent iron nanoparticles in the presence of dissolved oxygen. *Environ. Prog. Sustainable Energy.* **2016**, 35 (6), 1673–1678.
- (150) Rickard, D.; Roberts, A. P.; Navrotsky, A. Sedimentary greigite formation. *Am. J. Sci.* **2024**, 324, 13.
- (151) Suleimenov, O. M.; Seward, T. M. A spectrophotometric study of hydrogen sulphide ionisation in aqueous solutions to 350°C. *Geochim. Cosmochim. Acta* **1997**, *61* (24), 5187–5198.
- (152) Wolery, T. J.; Jove Colon, C. F. Chemical thermodynamic data. 1. The concept of links to the chemical elements and the historical development of key thermodynamic data. *Geochim. Cosmochim. Acta* 2017, 213, 635–676.
- (153) Rickard, D. The solubility of FeS. Geochim. Cosmochim. Acta 2006, 70 (23), 5779-5789.
- (154) Parker, V. B.; Khodakovskii, I. L. Thermodynamic properties of the aqueous ions (2+ and 3+) of iron and the key compounds of iron. *J. Phys. Chem. Ref. Data.* **1995**, 24 (5), 1699–1745.
- (155) Wang, X.; Dai, Z.; Ko, S.; Deng, G.; Zhao, Y.; Dai, C.; Li, W.; Paudyal, S.; Yao, X.; Kan, A. T.; Tomson, M.; et al. Iron sulfide solubility measurement and modeling over wide ranges of temperatures, ionic strength, and pH. SPE J. 2022, 27 (2), 1263–1274.
- (156) Shumway, S. G.; Wilson, J.; Lilova, K.; Subramani, T.; Navrotsky, A.; Woodfield, B. F. The low-temperature heat capacity and thermodynamic properties of greigite (Fe₃S₄). *J. Chem. Thermodyn.* **2022**, *173*, 106836.
- (157) Lemire, R.; Palmer, D.; Taylor, P.; Schlenz, H. Chemical Thermodynamics of Iron, Part 2. In *Chemical Thermodynamics; OECD*

- Nuclear Energy Agency Data Bank; OECD Publications: Paris, 2020; Vol 13b.
- (158) Helgeson, H. C.; Delany, J. M.; Nesbitt, H. W.; Bird, D. K. Summary and critique of the thermodynamic properties of rockforming minerals. *Am. J. Sci.* **1978**, 278, 1–229.
- (159) Berner, R. A. Thermodynamic stability of sedimentary iron sulfides. *Am. J. Sci.* **1967**, 265 (9), 773–785.
- (160) Davison, W. The solubility of iron sulphides in synthetic and natural waters at ambient temperature. *Aquat. Sci.* **1991**, 53 (4), 309–329
- (161) Son, S.; Hyun, S. P.; Charlet, L.; Kwon, K. D. Thermodynamic stability reversal of iron sulfides at the nanoscale: Insights into the iron sulfide formation in low-temperature aqueous solution. *Geochim. Cosmochim. Acta* **2022**, 338, 220–228.
- (162) Kwon, K. D.; Refson, K.; Bone, S.; Qiao, R. M.; Yang, W. L.; Liu, Z.; Sposito, G. Magnetic ordering in tetragonal FeS: Evidence for strong itinerant spin fluctuations. *Phys. Rev. B* **2011**, 83 (6), 064402.
- (163) Kitchaev, D. A.; Ceder, G. Evaluating structure selection in the hydrothermal growth of FeS₂ pyrite and marcasite. *Nat. Comm.* **2016**, *7*, 13799.
- (164) Dzade, N. Y.; Roldan, A.; de Leeuw, N. H. DFT-D2 study of the adsorption and dissociation of water on clean and oxygen-covered {001} and {011} surfaces of mackinawite (FeS). *J. Phys. Chem. C* **2016**, 120 (38), 21441–21450.
- (165) Dzade, N. Y.; Roldan, A.; de Leeuw, N. H. Surface and shape modification of mackinawite (FeS) nanocrystals by cysteine adsorption: a first-principles DFT-D2 study. *Phys. Chem. Chem. Phys.* **2016**, *18* (47), 32007–32020.
- (166) Kashchiev, D. Nucleation: Basic Theory with Applications; Butterworth-Heinemann, 2000.
- (167) Pina, C. M.; Putnis, A. The kinetics of nucleation of solid solutions from aqueous solutions: A new model for calculating non-equilibrium distribution coefficients. *Geochim. Cosmochim. Acta* **2002**, 66 (2), 185–192.
- (168) Nielsen, A. E. Kinetics of Precipitation; Pergamon Press, 1964.
- (169) Shim, H. M.; Kim, J. K.; Kim, H. S.; Koo, K. K. Molecular dynamics simulation on nucleation of ammonium perchlorate from an aqueous solution. *Cryst. Growth Des.* **2014**, *14* (11), 5897–5903.
- (170) Subramani, T.; Lilova, K.; Abramchuk, M.; Leinenweber, K. D.; Navrotsky, A. Greigite (Fe₃S₄) is thermodynamically stable: Implications for its terrestrial and planetary occurrence. *Proc. Natl. Acad. Sci. U. S. A.* **2020**, *117* (46), 28645–28648.
- (171) Navrotsky, A.; Ma, C.; Lilova, K.; Birkner, N. Nanophase transition metal oxides show large thermodynamically driven shifts in oxidation-reduction equilibria. *Science* **2010**, 330 (6001), 199–201.
- (172) Navrotsky, A. Nanoscale effects on thermodynamics and phase equilibria in oxide systems. *Chemphyschem* **2011**, 12 (12), 2207–2215.
- (173) Takeno, S.; Clark, A. H. Observations on tetragonal (Fe, Ni, Co)_{1+x} S, mackinawite. *J. Sci., Hiroshima Univ., Ser. C* 1967, 5, 287–293. (174) Takeno, S. Thermal studies on mackinawite. *J. Sci., Hiroshima Univ., Ser C.* 1965, 4, 445–478.
- (175) Clark, A. H. Some comments on the composition and stability relations of mackinawite. *Neu. Jb. Mineral, Mh.* **1966**, 300–304.
- (176) Zoka, H.; Taylor, L. A.; Takeno, S. Compositional variations in natural mackinawite and the results of heating experiments. *J. Sci., Hiroshima Univ., Ser. C.* **1972**, *7*, 37–53.
- (177) Sarkar, S. C. Mackinawite from the sulfide ores of the Singbaum Copper belt, India. *Am. Mineral.* **1971**, *56*, 1312–1318.
- (178) Lennie, A. R.; England, K. E. R.; Vaughan, D. J. Transformation of synthetic mackinawite to hexagonal pyrrhotite: A kinetic study. *Am. Mineral.* **1995**, *80*, 960–967.
- (179) Clark, A. H. Some comments on the compositions and stability relations of mackinawite. *Neu. Jb. Mineral., Mh.* **1966**, *10*, 300–304.
- (180) Barnes, S. J.; Holwell, D. A.; Le Vaillant, M. Magmatic sulfide ore deposits. *Elements* **2017**, *13* (2), 89–95.
- (181) Misra, K. C.; Fleet, M. E. Chemical compositions of synthetic and natural pentlandite assemblages. *Econ. Geol.* **1973**, *68* (4), 518–539.

- (182) Smith, W. D.; Maier, W. D.; Bliss, I. Distribution of noble metals in magmatic sulfide occurrences in the Montagnais sill complex, Labrador trough, Canada. *Can. Mineral.* **2021**, *59* (6), 1599–1626.
- (183) Van Rensburg, W. C.J.; Liebenberg, L. Mackinawite from South Africa. Am. Mineral. 1967, 52, 1027–1035.
- (184) Kitakaze, A.; Machida, T.; Komatsu, R. Phase relations in the Fe-Ni-S system from 875 to 650°C. *Can. Mineral.* **2016**, *54*, 1175–1186.
- (185) Schwarzenbach, E. M.; Vrijmoed, J. C.; Engelmann, J. M.; Liesegang, M.; Wiechert, U.; Rohne, R.; Plümper, O. Sulfide dissolution and awaruite formation in continental serpentinization environments and its implications to supporting life. *J. Geophys. Res.: Solid Earth.* **2021**, 126 (5), e2021JB021758.
- (186) White, L. M.; Bhartia, R.; Stucky, G. D.; Kanik, I.; Russell, M. J. Mackinawite and greigite in ancient alkaline hydrothermal chimneys: Identifying potential key catalysts for emergent life. *Earth Planet. Sci. Lett.* **2015**, 430, 105–114.
- (187) Krupp, R. E. Phase relations and phase transformations between the low temperature iron sulfides mackinawite, greigite, and smythite. *Eur. J. Mineral.* **1994**, *6* (2), 265–278.
- (188) King, H. E.; Prewitt, C. T. High-pressure and high-temperature polymorphism of iron sulfide (FeS). *Acta Crystallogr., Sect. B:Struct. Sci.* **1982**, 38 (JUL), 1877–1887.
- (189) Liu, S.; Li, Y.; Yang, Z.; Liu, J. Fe isotope fractionation caused by phase transition of FeS and implications for Fe isotope signatures of the mantle and core. *Geochim. Cosmochim. Acta* **2023**, 340, 38–50.
- (190) Marshall, W. G.; Nelmes, R. J.; Loveday, J. S.; Klotz, S.; Besson, J. M.; Hamel, G.; Parise, J. B. High-pressure neutron-diffraction study of FeS. *Phys. Rev. B.* **2000**, *61* (17), 11201–11204.
- (191) Sata, N.; Ohfuji, H.; Hirose, K.; Kobayashi, H.; Ohishi, Y.; Hirao, N. New high-pressure b2 phase of FeS above 180 GPa. *Am. Mineral.* **2008**, 93 (2–3), 492–494.
- (192) Rickard, D. Kinetics of FeS precipitation: Part 1. Competing reaction mechanisms. *Geochim. Cosmochim. Acta* **1995**, 59 (21), 4367–4379.
- (193) Eigen, M.; Wilkins, R. G. The kinetics and mechanism of formation of metal complexes. *Mechanisms of Inorganic Reactions.*; ACS Symposium Series; American Chemical Society, 1965; Vol. 49, pp 55–80
- (194) Rickard, D.; Luther, G. Aqueous metal sulfide clusters in marine sediments: Implications for transport, mineral formation and ecology. *Geochim. Cosmochim. Acta* **2003**, *67* (18), A398–A398.
- (195) Rickard, D.; Luther, G. W. Metal sulfide complexes and clusters. *Rev. Mineral. Geochem.* **2006**, *61*, 421–504.
- (196) Luther, G. W., III.; Mullaugh, K. M.; Yucel, M.; Rickard, D.; Spraggins, J. M., II.; Ridge, D. P.; Hsu-Kim, H. Metal sulfide nanoparticles and clusters in the environment. *Abstr. Pap. Am. Chem. Soc.* **2009**, 237.79
- (197) Spielman-Sun, E.; Boye, K.; Dwivedi, D.; Engel, M.; Thompson, A.; Kumar, N.; Noël, V. A critical look at colloid generation, stability, and transport in redox-dynamic environments: challenges and perspectives. ACS Earth Space Chem. 2024, 8 (4), 630–653.
- (198) Luther, G. W.; Rickard, D. T. Metal sulfide cluster complexes and their biogeochemical importance in the environment. *J. Nanopart. Res.* **2005**, *7* (4–5), 389–407.
- (199) Rickard, D. Sulfidic Sediments and Sedimentary Rocks; Elsevier, 2012.
- (200) Moerman, E.; Furman, D.; Wales, D. J. Development of ReaxFF reactive force field for aqueous iron-sulfur clusters with applications to stability and reactivity in water. *J. Chem. Inf. Model.* **2021**, *61* (3), 1204–1214.
- (201) Terranova, U.; de Leeuw, N. H. Aqueous Fe_2S_2 cluster: structure, magnetic coupling, and hydration behaviour from Hubbard U density functional theory. *Phys. Chem. Chem. Phys.* **2014**, *16* (26), 13426-13433.
- (202) DeRosha, D. E.; Chilkuri, V. G.; Van Stappen, C.; Bill, E.; Mercado, B. Q.; DeBeer, S.; Neese, F.; Holland, P. L. Planar three-coordinate iron sulfide in a synthetic 4Fe-3S cluster with biomimetic reactivity. *Nat. Chem.* **2019**, *11* (11), 1019–1025.

- (203) Watson, J. H. P.; Cressey, B. A.; Roberts, A. P.; Ellwood, D. C.; Charnock, J. M.; Soper, A. K. Structural and magnetic studies on heavy-metal-adsorbing iron sulphide nanoparticles produced by sulphate-reducing bacteria. *J. Magn. Magn. Mater.* **2000**, 214 (1), 13–30.
- (204) Luther, G. W., III; Rickard, D. T. Metal sulfide cluster complexes and their biogeochemical importance in the environment. *J. Nanopart. Res.* **2005**, *7* (4–5), 389–407.
- (205) Karthika, S.; Radhakrishnan, T. K.; Kalaichelvi, P. A review of classical and nonclassical nucleation theories. *Cryst. Growth Des.* **2016**, *16* (11), 6663–6681.
- (206) Russo, J.; Tanaka, H. Nonclassical pathways of crystallization in colloidal systems. MRS Bull. **2016**, 41 (5), 369–374.
- (207) Wen, X. L.; Bai, P. P.; Luo, B. W.; Zheng, S. Q.; Chen, C. F. Review of recent progress in the study of corrosion products of steels in a hydrogen sulphide environment. *Corros. Sci.* **2018**, *139*, 124–140.
- (208) Jeon, S. H.; Kim, S. T.; Lee, I. S.; Park, Y. S. Effects of sulfur addition on pitting corrosion and machinability behavior of super duplex stainless steel containing rare earth metals: Part 2. *Corros. Sci.* **2010**, 52 (10), 3537–3547.
- (209) Macdonald, D. D.; Roberts, B.; Hyne, J. B. Corrosion of carbonsteel by wet elemental sulfur. *Corros. Sci.* 1978, 18 (5), 411–425.
- (210) Schmitt, G. Effect of elemental sulfur on corrosion in sour gas systems. *Corros.* **1991**, 47 (4), 285–308.
- (211) Dowling, N. I. Corrosion of materials used in storage and handling of solid elemental sulfur. In *International Symposium on Materials Performance: Sulphur and Energy, at the 31st Annual Conference of Metallurgists of the Canadian Institution of Mining Metallurgy and Petroleum, Edmonton, Canada, Aug 23–27, 1992*; Metallurgical Society of the Institute of Mining, Metallurgy and Petroleum, 1992; pp 103–115
- (212) Rickard, D. Experimental concentration-time curves for the iron(II) sulphide precipitation process in aqueous solutions and their interpretation. *Chem. Geol.* **1989**, 78 (3–4), 315–324.
- (213) Butler, I.; Bell, A. M. T.; Charnock, J. M.; Rickard, D.; Vaughan, D.; Oldroyd, A. Nanoparticulate mackinawite formation; a stopped and continuous flow XANES and EXAFS investigation. In *American Geophysical Union, Fall Meeting*; American Geophysical Union: San Francisco, 2009; Vol. 43, p V43C2269B.
- (214) Luther, G. W. Pyrite synthesis via polysulfide compounds. *Geochim. Cosmochim. Acta* **1991**, 55 (10), 2839–2849.
- (215) Taylor, P.; Rummery, T. E.; Owen, D. G. Conversion of mackinawite to greigite. *J. Inorg. Nucl. Chem.* **1979**, 41 (4), 595–596.
- (216) Widler, A. M.; Seward, T. M. The adsorption of gold(I) hydrosulphide complexes by iron sulphide surfaces. *Geochim. Cosmochim. Acta* **2002**, *66* (3), 383–402.
- (217) Rickard, D.; Luther, G. W. Kinetics of pyrite formation by the H_2S oxidation of iron (II) monosulfide in aqueous solutions between 25 and 125°C: The mechanism. *Geochim. Cosmochim. Acta* **1997**, *61* (1), 135–147.
- (218) Wolthers, M.; Van der Gaast, S. J.; Rickard, D. The structure of disordered mackinawite. *Am. Mineral.* **2003**, 88 (11–12), 2007–2015.
- (219) Guilbaud, R.; Butler, I. B.; Ellam, R. M.; Rickard, D. Fe isotope exchange between $Fe(II)_{aq}$ and nanoparticulate mackinawite (FeS_{m}) during nanoparticle growth. *Earth Planet. Sci. Lett.* **2010**, 300 (1–2), 174–183.
- (220) Huang, F.; Zhang, H. Z.; Banfield, J. F. Two-stage crystal-growth kinetics observed during hydrothermal coarsening of nanocrystalline ZnS. *Nano Lett.* **2003**, 3 (3), 373–378.
- (221) Li, D.; Chen, Q.; Chun, J.; Fichthorn, K.; De Yoreo, J.; Zheng, H. Nanoparticle assembly and oriented attachment: Correlating controlling factors to the resulting structures. *Chem. Rev.* **2023**, *123* (6), 3127–3159.
- (222) Joesten, R. Grain-boundary diffusion kinetics in silicate and oxide minerals. *Diffusion, Atomic Ordering, and Mass Transport: Selected Topics in Geochemistry*; Springer, 1991; pp 345–395.
- (223) Duverger, A.; Berg, J. S.; Busigny, V.; Guyot, F.; Bernard, S.; Miot, J. Mechanisms of pyrite formation promoted by sulfate-reducing bacteria in pure culture. *Front. Earth Sci.* **2020**, *8*, 588310.

- (224) Pósfai, M.; Dunin-Borkowski, R. E. Sulfides in biosystems. *Rev. Miner.*. *Geochem.* **2006**, *61*, 679.
- (225) Devey, A. J.; Grau-Crespo, R.; de Leeuw, N. H. Combined density functional theory and interatomic potential study of the bulk and surface structures and properties of the iron sulfide mackinawite (FeS). J. Phys. Chem. C 2008, 112 (29), 10960–10967.
- (226) Ritvo, G.; White, G. N.; Dixon, J. B. A new iron sulfide precipitated from saline solutions. *Soil Sci. Soc. Am. J.* **2003**, *67* (4), 1303–1308.
- (227) Murowchick, J. B.; Rickard, D. Structural changes during ripening of synthetic mackinawite formed by corrosion of alpha-iron. *Geol. Soc. Am. Abs..* **1997**, 29, 402.
- (228) Carr, S.; Massatt, D.; Fang, S.; Cazeaux, P.; Luskin, M.; Kaxiras, E. Twistronics: Manipulating the electronic properties of two-dimensional layered structures through their twist angle. *Phys. Rev. B.* **2017**, *95* (7), 075420.
- (229) Horiuchi, S. Zur Umwandlung von Mackinawit (FeS) in Greigit (Fe₃S₄) durch Elektronstrahen. *Z. Phys. Chem.* **1971**, 386 (2), 208–212. (230) Genchev, G.; Erbe, A. Raman spectroscopy of mackinawite FeS
- in anodic iron sulfide corrosion products. *J. Electrochem. Soc.* **2016**, 163 (6), C333—C338.
- (231) Bernal, J. D.; Dasgupta, D. R.; Mackay, A. L. Oriented transformations in iron oxides and hydroxides. *Nature* **1957**, *180* (4587), 645–647.
- (232) Cornell, R. M.; Schwertmann, U. The Iron Oxides: Structure, Properties, Reactions, Occurrences and Uses; Wiley, 2003.
- (233) Gallegos, T. J.; Han, Y. S.; Hayes, K. F. Model predictions of realgar precipitation by reaction of As(III) with synthetic mackinawite under anoxic conditions. *Environ. Sci. Technol.* **2008**, 42 (24), 9338–9343.
- (234) Uda, M. The structure of synthetic Fe_3S_4 and the nature of transition to FeS. Z. Phys. Chem. 1967, 350 (1–2), 105–109.
- (235) Yamaguch, S; Wada, H. Polymorphismus Zwischen Greigit und Smythit (Fe₃S₄). Z. Phys. Chem. **1972**, 392 (2), 191–192.
- (236) Rickard, D. Metastable sedimentary iron sulfides. Sulfidic Sediments and Sedimentary Rocks; Elsevier. 2012; pp 195–231.
- (237) Lennie, A. R. Aspects of relations between metastable and stable phases in the iron-sulphur system. PhD Thesis. Manchester University: Manchester UK, 1994.
- (238) Birkholz, M. Modeling the shape of ions in pyrite-type crystals. *Crystals* **2014**, 4 (3), 390–403.
- (239) Rickard, D. Sulfur chemistry in aqueous solutions. *Sulfidic Sediments and Sedimentary Rocks*; Elsevier, 2012; pp 31–83.
- (240) Kamyshny, A.; Goifman, A.; Gun, J.; Rizkov, D.; Lev, O. Equilibrium distribution of polysulfide ions in aqueous solutions at 25 °C: A new approach for the study of polysulfides equilibria. *Environ. Sci. Technol.* **2004**, *38* (24), *6633–6644*.
- (241) Butler, I.; Bottcher, M.; Rickard, D.; Oldroyd, A. Sulfur isotope partitioning during experimental formation of pyrite via the polysulfide and hydrogen sulfide pathways: implications for the interpretation of sedimentary and hydrothermal pyrite isotope records. *Earth Planet. Sci. Lett.* **2004**, 228 (3–4), 495–509.
- (242) Berner, R. A. Sedimentary pyrite formation. *Am. J. Sci.* **1970**, 268 (1), 1–23.
- (243) Rickard, D. T. Kinetics and mechanism of pyrite formation at low-temperatures. *Am. J. Sci.* **1975**, 275 (6), 636–652.
- (244) Graham, U. M.; Ohmoto, H. Experimental study of formation mechanisms of hydrothermal pyrite. *Geochim. Cosmochim. Acta* **1994**, 58 (10), 2187–2202.
- (245) Berzelius, J. J. *Traité de Chimie*; Chez Firmin Didot Frères, 1845. (246) Wikjord, A. G.; Rummery, T. E.; Doern, F. E. Crystallization of pyrite from deoxygenated aqueous sulfide solutions at elevated temperature and pressure. *Can. Mineral.* **1976**, *14*, 571–573.
- (247) Huber, C.; Wächtershauser, G. Activated acetic acid by carbon fixation on (Fe,Ni)S under primordial conditions. *Science* **1997**, 276 (5310), 245–247.
- (248) Rickard, D. Kinetics of pyrite formation by the H_2S oxidation of iron (II) monosulfide in aqueous solutions between 25 and 125°C: The rate equation. *Geochim. Cosmochim. Acta* 1997, 61 (1), 115–132.

- (249) Wei, S. K.; Zheng, S. Q.; Liang, J. X. New insights of the interaction of H₂S with mackinawite FeS in a wet environment: An ab initio molecular dynamics study. *Int.J. Hydrogen Energy.* **2024**, 72, 1216–1223.
- (250) Butler, I. B.; Böttcher, M. E.; Rickard, D.; Oldroyd, A. Sulfur isotope partitioning during experimental formation of pyrite via the polysulfide and hydrogen sulfide pathways: Implications for the interpretation of sedimentary and hydrothermal pyrite isotope records. *Earth Planet. Sci. Lett.* **2004**, 228 (3–4), 495–509.
- (251) Luther, G. Metal sulfides in the environment and in bioinorganic chemistry. *Inorganic Chemistry for Geochemistry and Environmental Sciences: Fundamentals and Applications*; Wiley, 2016; pp 390–405.
- (252) Wolthers, M.; Charlet, L.; Van der Linde, P. R.; Rickard, D.; Van der Weijden, C. H. Surface chemistry of disordered mackinawite (FeS). *Geochim. Cosmochim. Acta* **2005**, *69* (14), 3469–3481.
- (253) Rickard, D. Sedimentary sulfides. Sulfidic Sediments and Sedimentary Rocks; Elsevier, 2012; pp 543-604.
- (254) Fagnani, E.; Guimaraes, J. Ř.; Mozeto, A. A.; Fadini, P. S. Acid volatile sulfides and simultaneously extracted metals in the assessment of freshwater sediments. *Quim. Nova* **2011**, *34* (9), 1618–1628.
- (255) Rickard, D.; Morse, J. W. Acid volatile sulfide (AVS). *Mar. Chem.* **2005**, 97 (3-4), 141-197.
- (256) Costello, D. M.; Burton, G. A.; Hammerschmidt, C. R.; Rogevich, E. C.; Schlekat, C. E. Nickel phase partitioning and toxicity in field-deployed sediments. *Environ. Sci. Technol.* **2011**, 45 (13), 5798–5805
- (257) Phillips, H. O.; Kraus, K. A. Adsorption on inorganic materials. 6. Reaction of insoluble sulfides with metal ions in aqueous media. *J. Chromatogr.* **1965**, *17* (3), 549–557.
- (258) Huerta-Diaz, M. A.; Tessier, A.; Carignan, R. Geochemistry of trace metals associated with reduced sulfur in freshwater sediments. *Appl. Geochem.* **1998**, *13* (2), 213–233.
- (259) Boursiquot, S.; Mullet, M.; Ehrhardt, J. J. XPS study of the reaction of chromium (VI) with mackinawite (FeS). *Surf. Interface Anal.* **2002**, 34 (1), 293–297.
- (260) Patterson, R. R.; Fendorf, S.; Fendorf, M. Reduction of hexavalent chromium by amorphous iron sulfide. *Environ. Sci. Technol.* **1997**, *31* (7), 2039–2044.
- (261) Kim, C.; Zhou, Q.; Deng, B.; Thornton, E. C.; Xu, H. Chromium(VI) reduction by hydrogen sulfide in aqueous media: Stoichiometry and kinetics. *Environ. Sci. Technol.* **2001**, 35 (11), 2219–2225
- (262) Morse, J. W.; Arakaki, T. Adsorption and coprecipitation of divalent metals with mackinawite (FeS). *Geochim. Cosmochim. Acta* **1993**, *57* (15), 3635–3640.
- (263) Wilkin, R. T.; Beak, D. G. Uptake of nickel by synthetic mackinawite. Chem. Geol. 2017, 462, 15–29.
- (264) Cowper, M.; Rickard, D. Mechanism of chalcopyrite formation from iron monosulphides in aqueous solutions (< 100° C, pH 2–4.5). *Chem. Geol.* **1989**, 78 (3–4), 325–341.
- (265) Rickard, D.; Cowper, M. Kinetics and mechanism of chalcopyrite formation from Fe(II) disulphide in aqueous solution (< 200°C). *Geochim. Cosmochim. Acta* **1994**, *58* (18), 3795–3802.
- (266) Parkman, R. H.; Charnock, J. M.; Bryan, N. D.; Livens, F. R.; Vaughan, D. J. Reactions of copper and cadmium ions in aqueous solution with goethite, lepidocrocite, mackinawite, and pyrite. *Am. Mineral.* 1999, 84 (3), 407–419.
- (267) Cooper, D. C.; Morse, J. W. Selective extraction chemistry of toxic metal sulfides from sediments. *Aquat. Geochem.* **1999**, *5* (1), 87–97
- (268) Farquhar, M. L.; Charnock, J. M.; Livens, F. R.; Vaughan, D. J. Mechanisms of arsenic uptake from aqueous solution by interaction with goethite, lepidocrocite, mackinawite, and pyrite: An X-ray absorption spectroscopy study. *Environ. Sci. Technol.* **2002**, *36* (8), 1757–1762.
- (269) Bostick, B. C.; Fendorf, S. Arsenite sorption on troilite (FeS) and pyrite (FeS₂). *Geochim. Cosmochim. Acta* **2003**, *67* (5), 909–921.

- (270) Gallegos, T. J.; Hyun, S. P.; Hayes, K. F. Spectroscopic investigation of the uptake of arsenite from solution by synthetic mackinawite. *Environ. Sci. Technol.* **2007**, *41* (22), 7781–7786.
- (271) Renock, D.; Gallegos, T.; Utsunomiya, S.; Hayes, K.; Ewing, R. C.; Becker, U. Chemical and structural characterization of As immobilization by nanoparticles of mackinawite (FeS_m). *Chem. Geol.* **2009**, *268* (1–2), 116–125.
- (272) Wolthers, M.; Butler, I. B.; Rickard, D. Influence of arsenic on iron sulfide transformations. *Chem. Geol.* **2007**, 236 (3–4), 217–227. (273) Couture, R. M.; Rose, J.; Kumar, N.; Mitchell, K.; Wallschläger, D.; Van Cappellen, P. Sorption of arsenite, arsenate, and thioarsenates to iron oxides and iron sulfides: A kinetic and spectroscopic investigation. *Environ. Sci. Technol.* **2013**, 47 (11), 5652–5659.
- (274) Wolthers, M.; Charlet, L.; Van der Weijden, C. H.; Van der Linde, P. R.; Rickard, D. Arsenic mobility in the ambient sulfidic environment: Sorption of arsenic(V) and arsenic(III) onto disordered mackinawite. *Geochim. Cosmochim. Acta* 2005, 69 (14), 3483–3492.
- (275) Finck, N.; Dardenne, K.; Bosbach, D.; Geckeis, H. Selenide retention by mackinawite. *Environ. Sci. Technol.* **2012**, 46 (18), 10004–10011.
- (276) Han, D. S.; Batchelor, B.; Abdel-Wahab, A. Sorption of selenium(IV) and selenium(VI) to mackinawite (FeS): Effect of contact time, extent of removal, sorption envelopes. *J. Hazard. Mater.* **2011**, *186* (1), 451–457.
- (277) Scheinost, A. C.; Charlet, L. Selenite reduction by mackinawite, magnetite and siderite: XAS characterization of nanosized redox products. *Environ. Sci. Technol.* **2008**, 42 (6), 1984–1989.
- (278) Miller, N.; Dougherty, M.; Du, R. C.; Sauers, T.; Yan, C.; Pines, J. E.; Meyers, K. L.; Dang, Y. M.; Nagle, E.; Ni, Z. Q.; et al. Adsorption of tetrathiomolybdate to iron sulfides and its impact on iron sulfide transformations. *ACS Earth Space Chem.* **2020**, *4* (12), 2246–2260.
- (279) Livens, F. R.; Jones, M. J.; Hynes, A. J.; Charnock, J. M.; Mosselmans, J. F. W.; Hennig, C.; Steele, H.; Collison, D.; Vaughan, D. J.; Pattrick, R. A. D.; et al. X-ray absorption spectroscopy studies of reactions of technetium, uranium and neptunium with mackinawite. *J. Environ. Radioact.* **2004**, 74 (1–3), 211–219.
- (280) Coles, C. A.; Rao, S. R.; Yong, R. N. Lead and cadmium interactions with mackinawite: Retention mechanisms and the role of pH. *Environ. Sci. Technol.* **2000**, 34 (6), 996–1000.
- (281) Mustafa, S.; Misbahud, D.; Sammad, Y. H.; Zaman, M. I.; Sadullah, K. Sorption mechanism of cadmium from aqueous solution on iron sulphide. *Chin. J. Chem.* **2010**, 28 (7), 1153–1158.
- (282) Watson, J. H. P.; Ellwood, D. C.; Deng, Q. X.; Mikhalovsky, S.; Hayter, C. E.; Evans, J. Heavy-metal adsorption on bacterially produced FeS. *Miner. Eng.* **1995**, *8* (10), 1097–1108.
- (283) Cao, S. Y.; Zhang, L.; Ling, C. C.; Guo, F. R.; Li, M. Q.; Liang, C.; Cheng, J. D.; Shi, Y. B.; Sun, H. W.; Zhang, L. Z. Rational surface oxidation promoted long-term Cd(II) removal performance of mackinawite (FeS). ACS ES&T Eng. 2024, 4 (5), 1167–1176.
- (284) Han, Y. S.; Seong, H. J.; Chon, C. M.; Park, J. H.; Nam, I. H.; Yoo, K.; Ahn, J. S. Interaction of Sb(III) with iron sulfide under anoxic conditions: Similarities and differences compared to As(III) interactions. *Chemosphere* **2018**, *195*, 762–770.
- (285) Li, D. L.; Zhang, G. P.; Wang, Q. Y.; Liu, S. R.; Ma, C.; Chen, J. J.; Liu, F. J. Interaction of aqueous antimony(III) with synthetic ferrous sulfide. *Appl. Geochem.* **2021**, *128*, 104957.
- (286) Dulnee, S.; Scheinost, A. C. Interfacial reaction of Sn^{II} on mackinawite (FeS). *J. Contam. Hydrol.* **2015**, *177*, 183–193.
- (287) Park, C. K.; Park, T. J.; Lee, S. Y.; Lee, J. K. Sorption characteristics of iodide on chalcocite and mackinawite under pH variations in alkaline conditions. *Nucl. Eng. Technol.* **2019**, *51* (4), 1041–1046.
- (288) Jeong, H. Y.; Klaue, B.; Blum, J. D.; Hayes, K. F. Sorption of mercuric ion by synthetic manocrystalline mackinawite (FeS). *Environ. Sci. Technol.* **2007**, *41*, 7699–7705.
- (289) Liu, J. R.; Valsaraj, K. T.; Delaune, R. D. Inhibition of mercury methylation by iron sulfides in an anoxic sediment. *Environ. Eng. Sci* **2009**, *26* (4), 833–840.

- (290) Chaves, M. R. M.; Valsaraj, K. T.; Gambrell, R. P.; Delaune, R. D.; Buchler, P. M. Mercury uptake by modified mackinawite. *Soil Sediment Contam.* **2013**, 22 (1), 95–104.
- (291) Gong, Y.; Liu, Y.; Xiong, Z.; Kaback, D.; Zhao, D. Immobilization of mercury in field soil and sediment using carboxymethyl cellulose stabilized iron sulfide nanoparticles. *Nanotech.* **2012**, 23 (29), 294007.
- (292) Jeong, H. Y.; Sun, K.; Hayes, K. F. Microscopic and spectroscopic characterization of Hg(II) immobilization by mackinawite (FeS). *Environ. Sci. Technol.* **2010**, 44 (19), 7476–7483.
- (293) Skyllberg, U.; Drott, A. Competition between disordered iron sulfide and natural organic matter associated thiols for mercury(II)—An EXAFS study. *Environ. Sci. Technol.* **2010**, 44 (4), 1254–1259.
- (294) Moyes, L. N.; Parkman, R. H.; Charnock, J. M.; Vaughan, D. J.; Livens, F. R.; Hughes, C. R.; Braithwaite, A. Uranium uptake from aqueous solution by interaction with goethite, lepidocrocite, muscovite, and mackinawite: An X-ray absorption spectroscopy study. *Environ. Sci. Technol.* 2000, 34 (6), 1062–1068.
- (295) Ofili, N. E. R.; Thetford, A.; Kaltsoyannis, N. Adsorption of U(VI) on stoichiometric and oxidised mackinawite: a DFT study. *Environ. Sci. Technol.* **2020**, 54 (11), 6792–6799.
- (296) Gallegos, T. J.; Fuller, C. C.; Webb, S. M.; Betterton, W. Uranium(VI) Interactions with mackinawite in the presence and absence of bicarbonate and oxygen. *Environ. Sci. Technol.* **2013**, 47 (13), 7357–7364.
- (297) Moyes, L. N.; Jones, M. J.; Reed, W. A.; Livens, F. R.; Charnock, J. M.; Mosselmans, J. F. W.; Hennig, C.; Vaughan, D. J.; Pattrick, R. A. D. An X-ray absorption spectroscopy study of neptunium(V) reactions with mackinawite (FeS). *Environ. Sci. Technol.* **2002**, *36* (2), 179–183. (298) Kirsch, R.; Fellhauer, D.; Altmaier, M.; Neck, V.; Rossberg, A.; Fanghänel, T.; Charlet, L.; Scheinost, A. C. Oxidation state and local structure of plutonium reacted with magnetite, mackinawite, and chukanovite. *Environ. Sci. Technol.* **2011**, *45* (17), 7267–7274.
- (299) Park, J. H.; Kim, S. J.; Ahn, J. S.; Lim, D. H.; Han, Y. S. Mobility of multiple heavy metalloids in contaminated soil under various redox conditions: Effects of iron sulfide presence and phosphate competition. *Chemosphere* **2018**, 197, 344–352.
- (300) Sun, Y.; Lou, Z. M.; Yu, J. B.; Zhou, X. X.; Lv, D.; Zhou, J. S.; Baig, S. A.; Xu, X. H. Immobilization of mercury (II) from aqueous solution using Al_2O_3 -supported nanoscale FeS. *Chem. Eng. J.* **2017**, 323, 483–491.
- (301) Veeramani, H.; Scheinost, A. C.; Monsegue, N.; Qafoku, N. P.; Kukkadapu, R.; Newville, M.; Lanzirotti, A.; Pruden, A.; Murayama, M.; Hochella, M. F. Abiotic reductive immobilization of U(VI) by biogenic mackinawite. *Environ. Sci. Technol.* **2013**, 47 (5), 2361–2369.
- (302) Bi, Y. Q.; Hyun, S. P.; Kukkadapu, R. K.; Hayes, K. F. Oxidative dissolution of UO₂ in a simulated groundwater containing synthetic nanocrystalline mackinawite. *Geochim. Cosmochim. Acta* **2013**, *102*, 175–190.
- (303) Shao, D. D.; Ren, X. M.; Wen, J.; Hu, S.; Xiong, J.; Jiang, T.; Wang, X. L.; Wang, X. K. Immobilization of uranium by biomaterial stabilized FeS nanoparticles: Effects of stabilizer and enrichment mechanism. *J. Hazard. Mater.* **2016**, 302, 1–9.
- (304) Gong, Y. Y.; Liu, Y. Y.; Xiong, Z.; Zhao, D. Y. Immobilization of mercury by carboxymethyl cellulose stabilizedi iron sulfide nanoparticles: reaction mechanisms and effects of stabilizer and water chemistry. *Environ. Sci. Technol.* **2014**, 48 (7), 3986–3994.
- (305) Van Koetsem, F.; Van Havere, L.; Du Laing, G. Impact of carboxymethyl cellulose coating on iron sulphide nanoparticles stability, transport, and mobilization potential of trace metals present in soils and sediment. *J. Environ. Manage.* **2016**, *168*, 210–218.
- (306) Yang, H. P.; Hong, M.; Chen, S. Y. Removal of Cr(VI) with nano-FeS and CMC-FeS and transport properties in porous media. *Environ. Technol.* **2020**, *41* (22), 2935–2945.
- (307) Tian, S. T.; Zhao, D. Y.; Huo, L. J.; Ma, J.; Yang, R. Comparing three stabilizers for stabilizing FeS nanoparticles: Performance and effects on immobilization of cadmium in water and soil. *J. Cent. South Univ.* **2024**, *31* (4), 1064–1075.

- (308) He, S. Y.; Hu, W. R.; Liu, Y. L.; Xie, Y.; Zhou, H.; Wang, X. Q.; Chen, J.; Zhang, Y. K. Mechanism of efficient remediation of U(VI) using biogenic CMC-FeS complex produced by sulfate-reducing bacteria. *J. Hazard. Mater.* **2021**, *420*, 126645.
- (309) Lin, D. J.; Hu, G. Z.; Li, H. B.; Li, L.; Wu, F.; Yang, G. Q.; Zhuang, L.; Gong, Y. Y. Green remediation of mercury-contaminated soil using iron sulfide nanoparticles: Immobilization performance and mechanisms, effects on soil properties, and life cycle assessment. *Sci. Total Environ.* **2024**, 944, 173928.
- (310) Ji, H. D.; Zhu, Y. M.; Liu, W.; Bozack, M. J.; Qian, T. W.; Zhao, D. Y. Sequestration of pertechnetate using carboxymethyl cellulose stabilized FeS nanoparticles: Effectiveness and mechanisms. *Colloids Surf.*, A. 2019, 561, 373–380.
- (311) Huang, X. X.; Huang, Q. S.; Luo, D. G.; Wu, Q. H.; Arulmani, S. R. B.; Xiao, T. F.; Zhang, H. G.; Huang, L. Sodium carboxymethyl cellulose and Fe-modified nano-FeS for enhancing sorption of thallium from water. *Water Air and Soil Pollution* **2022**, 233 (8), 298.
- (312) Zhao, Y.; Tian, S. T.; Gong, Y. Y.; Zhao, D. Y. Efficient removal of lead from water using stabilized iron sulfide nanoparticles: Effectiveness and effects of stabilizer. *Water Air and Soil Pollution* **2019**, 230 (6), 115.
- (313) Liu, H. Y.; Lyu, H. G.; Zhang, W.; Jiang, J.; Li, X. H.; Xue, S. G. Surfactant-modified SiO₂/FeS nanocomposites for remediation of cadmium pollution. *J. Cent. South Univ.* **2024**, *31* (4), 1163–1177.
- (314) Qu, G. J.; Zhang, Y.; Duan, Z. K.; Li, K.; Xu, C. H. Regulating the FeS_x assembly pattern of sulfidated zero-valent iron: All-in-one interface modulation with activated carbon. *Water Res.* **2024**, 248, 120860
- (315) He, S. Y.; Chen, J.; Wang, X. Q.; Wang, X. L.; Li, P. Y.; Zhang, Y. K. Green preparation of regenerable biohybrids with xanthan gumstabilized biogenic mackinawite nanoparticles for efficient treatment from high-concentration uranium wastewater. *Bioresour. Technol.* **2024**, 408, 131104.
- (316) Gong, Y.; Tang, J.; Zhao, D. Application of iron sulfide particles for groundwater and soil remediation: A review. *Water Res.* **2016**, 89, 309–320.
- (317) Chen, C. G.; Qiu, M. Q. High efficiency removal of Pb(II) in aqueous solution by a biochar-supported nanoscale ferrous sulfide composite. RSC Adv. 2021, 11 (2), 953–959.
- (318) Mazarji, M.; Bayero, M. T.; Minkina, T.; Sushkova, S.; Mandzhieva, S.; Bauer, T. V.; Soldatov, A.; Sillanpää, M.; Wong, M. H. Nanomaterials in biochar: Review of their effectiveness in remediating heavy metal-contaminated soils. *Sci. Total Environ.* **2023**, *880*, 163330.
- (319) Liu, R. R.; Zhang, Y. H.; Hu, B. W.; Wang, H. Improved Pb(II) removal in aqueous solution by sulfide@biochar and polysaccharose-FeS@biochar composites: Efficiencies and mechanisms. *Chemosphere* **2022**, 287, 132087.
- (320) Liu, T. T.; Zhou, Y. L.; Zheng, W. X.; Chang, C. G.; Dong, J. M.; Wen, J.; Zheng, X. G. FeS/MgO-biochar composites for boosting the adsorption-photocatalytic degradation of RhB. *Mater. Sci. Semicond. Process.* **2024**, *174*, 108178.
- (321) Wang, H.; Liu, R. R.; Chen, Q.; Mo, Y. W.; Zhang, Y. H. Biochar-supported starch/chitosan-stabilized nano-iron sulfide composites for the removal of lead ions and nitrogen from aqueous solutions. *Bioresour. Technol.* **2022**, 347, 126700.
- (322) Chen, G. H.; Wang, H.; Han, L.; Yang, N. C.; Hu, B. W.; Qiu, M. Q.; Zhong, X. Highly efficient removal of U(VI) by a novel biochar supported with FeS nanoparticles and chitosan composites. *J. Mol. Liq.* **2021**, 327, 114807.
- (323) Lyu, H. H.; Tang, J. C.; Huang, Y.; Gai, L. S.; Zeng, E. Y.; Liber, K.; Gong, Y. Y. Removal of hexavalent chromium from aqueous solutions by a novel biochar supported nanoscale iron sulfide composite. *Chem. Eng. J.* **2017**, 322, 516–524.
- (324) Zhou, L.; Dong, F. Q.; Liu, J.; Hudson-Edwards, K. A. Coupling effect of Fe³⁺ (aq) and biological, nano-sized FeS-coated limestone on the removal of redox-sensitive contaminants (As, Sb and Cr): Implications for *in situ* passive treatment of acid mine drainage. Appl. Geochem. 2017, 80, 102–111.

- (325) Liu, J.; Zhou, L.; Dong, F. Q.; Hudson-Edwards, K. A. Enhancing As(V) adsorption and passivation using biologically formed nano-sized FeS coatings on limestone: Implications for acid mine drainage treatment and neutralization. *Chemosphere* **2017**, *168*, 529–538
- (326) Rochette, E. A.; Bostick, B. C.; Li, G. C.; Fendorf, S. Kinetics of arsenate reduction by dissolved sulfide. *Environ. Sci. Technol.* **2000**, 34 (22), 4714–4720.
- (327) Mullet, M.; Boursiquot, S.; Ehrhardt, J. J. Removal of hexavalent chromium from solutions by mackinawite, tetragonal FeS. *Colloids Surf., A.* **2004**, 244 (1–3), 77–85.
- (328) Vanysek, P. Electrochemical series. In CRC Handbook of Chemistry and Physics; CRC Press, 2016; Vol. 5, pp 78-84.
- (329) Shilov, V. P.; Gogolev, A. V.; Fedoseev, A. M. Speciation, stability, and reactions of Np(III-VII) in aqueous solutions. *Radiochemistry* **2012**, 54 (3), 212–227.
- (330) Avetisyan, K.; Kamyshny, A. Thermodynamic constants of formation of disulfide anion in aqueous solutions. *Geochim. Cosmochim. Acta* **2022**, 325, 205–213.
- (331) Géhin, A.; Grenèche, J. M.; Tournassat, C.; Brendlé, J.; Rancourt, D. G.; Charlet, L. Reversible surface-sorption-induced electron-transfer oxidation of Fe(II) at reactive sites on a synthetic clay mineral. *Geochim. Cosmochim. Acta* **2007**, *71* (4), 863–876.
- (332) Kim, C.; Zhou, Q. H.; Deng, B. L.; Thornton, E. C.; Xu, H. F. Chromium(VI) reduction by hydrogen sulfide in aqueous media: Stoichiometry and kinetics. *Environ. Sci. Technol.* **2001**, 35 (11), 2219–2225.
- (333) Rickard, D.; Butler, I. B.; Oldroyd, A. A novel iron sulphide mineral switch and its implications for earth and planetary science. *Earth Planet. Sci. Lett.* **2001**, *189* (1–2), 85–91.
- (334) Wang, W.; Song, Y.; Wang, X.; Yang, Y.; Liu, X. Alpha-oxo acids assisted transformation of FeS to Fe₃S₄ at low temperature: Implications for abiotic, biotic, and prebiotic mineralization. *Astrobiology* **2015**, *15* (12), 1043–1051.
- (335) Ma, W.-W.; Zhu, M.-X.; Yang, G.-P.; Li, T.; Li, Q.-Q.; Liu, S.-H.; Li, J.-L. Stability and molecular fractionation of ferrihydrite-bound organic carbon during iron reduction by dissolved sulfide. *Chem. Geol.* **2022**, *594*, 120774.
- (336) Balind, K.; Ezzati, M.; Picard, A.; Gélinas, Y. Exploring the affinity and selectivity of sedimentary mackinawite (FeS) towards natural organic matter. *Geochim. Cosmochim. Acta* **2025**, 405, 98.
- (337) Nabeh, N.; Brokaw, C.; Picard, A. Quantification of organic carbon sequestered by biogenic iron sulfide minerals in long-term anoxic laboratory incubations. *Front. Microbiol.* **2022**, *13*, 662219.
- (338) He, Y. T.; Wilson, J. T.; Su, C.; Wilkin, R. T. Review of abiotic degradation of chlorinated solvents by reactive iron minerals in aquifers. *Groundwater Monit. Rem.* **2015**, 35 (3), 57–75.
- (339) Butler, E. C.; Hayes, K. F. Factors influencing rates and products in the transformation of trichloroethylene by iron sulfide and iron metal. *Environ. Sci. Technol.* **2001**, 35 (19), 3884–3891.
- (340) Jeong, H. Y.; Hayes, K. F. Impact of transition metals on reductive dechlorination rate of hexachloroethane by mackinawite. *Environ. Sci. Technol.* **2003**, 37 (20), 4650–4655.
- (341) Jeong, H. Y.; Kim, H.; Hayes, K. F. Reductive dechlorination pathways of tetrachloroethylene and trichloroethylene and subsequent transformation of their dechlorination products by mackinawite (FeS) in the presence of metals. *Environ. Sci. Technol.* **2007**, *41* (22), 7736–7742
- (342) Li, X. X.; Yan, C.; Zeng, Y. X.; Li, W. B.; Peng, T. W.; Song, B.; Zhou, C. Y. Abiotic transformation of chlorinated organics at the active surface of iron-bearing minerals in soils and sediments. *Sci. China Technol. Sci.* **2024**, *67* (10), 2991–3008.
- (343) Huang, B. B.; Long, J. M.; Chen, W. Q.; Zhu, Y. Y.; Zeng, G. M.; Lei, C. Linear free energy relationships of electrochemical and thermodynamic parameters for the electrochemical reductive dechlorination of chlorinated volatile organic compounds (Cl-VOCs). *Electrochim. Acta* **2016**, 208, 195–201.
- (344) Eberson, L. Electron-transfer reactions in organic-chemistry. 2. An analysis of alkyl halide reduction by electron-transfer reagents on the

- basis of the Marcus theory. Acta Chem. Scand., Ser. B. 1982, 36 (8), 533-543.
- (345) Li, D.; Peng, P. A.; Yu, Z. Q.; Huang, W. L.; Zhong, Y. Reductive transformation of hexabromocyclododecane (HBCD) by FeS. *Water Res.* **2016**, *101*, 195–202.
- (346) Eberson, L.; Lehmann, M. W.; Burghart, A.; Little, R. D.; Silvestri, G.; Tallec, A.; Shono, T.; Toftlund, H. Problems and prospects of the concerted dissociative electron transfer mechanism. *Acta Chem. Scand.* **1999**, *53* (10), 751–764.
- (347) Wächtershäuser, G. Origin of life in an iron sulphur world. In *The Molecular Origins of Life: Assembling Pieces of the Puzzle*; Cambridge University Press, 1998.
- (348) Heinen, W.; Lauwers, A. M. Organic sulfur compounds resulting from the interaction of iron sulfide, hydrogen sulfide and carbon dioxide in an anaerobic aqueous environment. *Origins Life*. **1996**, *26* (2), 131–150.
- (349) Hudson, R.; de Graaf, R.; Strandoo Rodin, M.; Ohno, A.; Lane, N.; McGlynn, S. E.; Yamada, Y. M. A.; Nakamura, R.; Barge, L. M.; Braun, D.; et al. CO₂ reduction driven by a pH gradient. *Proc. Natl. Acad. Sci. U. S. A.* **2020**, *117* (37), 22873–22879.
- (350) Grosch, M.; Stiebritz, M. T.; Bolney, R.; Winkler, M.; Jückstock, E.; Busch, H.; Peters, S.; Siegle, A. F.; van Slageren, J.; Ribbe, M.; et al. Mackinawite-supported reduction of C1 substrates into prebiotically relevant precursors. *ChemSystemsChem.* **2022**, 4 (5), No. e202200010.
- (351) Russell, M. J.; Hall, A. J. The emergence of life from iron monosulphide bubbles at a submarine hydrothermal redox and pH front. *J Geol Soc London*. **1997**, *154* (3), 377–402.
- (352) Živković, A.; Somers, M.; Camprubi, E.; King, H. E.; Wolthers, M.; de Leeuw, N. H. Changes in CO₂ adsorption affinity related to Ni doping in FeS surfaces: A DFT-D3 study. *Catalysts* **2021**, *11*, 486.
- (353) Bello, T. O.; Bresciani, A. E.; Nascimento, C. A. O.; Alves, R. M. B. Thermodynamic analysis of carbon dioxide hydrogenation to formic acid and methanol. *Chem. Eng. Sci.* **2021**, *242*, 116731.
- (354) Schoonen, M. A. A.; Cohn, C. A.; Roemer, E.; Laffers, R.; Simon, S. R.; O'Riordan, T. Mineral-Induced formation of reactive oxygen species. *Rev. Mineral. Geochem.* **2006**, *64* (1), 179–221.
- (355) Cohn, C. A.; Mueller, S.; Wimmer, E.; Leifer, N.; Greenbaum, S.; Strongin, D. R.; Schoonen, M. A. A. Pyrite-induced hydroxyl radical formation and its effect on nucleic acids. *Geochem. Trans.* **2006**, *7* (1), 3.
- (356) Zhang, P.; Yuan, S. Production of hydroxyl radicals from abiotic oxidation of pyrite by oxygen under circumneutral conditions in the presence of low-molecular-weight organic acids. *Geochim. Cosmochim. Acta* 2017, 218, 153–166.
- (357) He, F.; Xu, L.; Wang, H.; Jiang, C. Recent progress in molecular oxygen activation by iron-based materials: Prospects for nano-enabled in situ remediation of organic-contaminated sites. *Toxics* **2024**, *12*, 773.
- (358) Cheng, D.; Neumann, A.; Yuan, S.; Liao, W.; Qian, A. Oxidative degradation of organic contaminants by FeS in the presence of O₂. *Environ. Sci. Technol.* **2020**, *54* (7), 4091–4101.
- (359) Chen, X.; Xian, Z.; Gao, S.; Bai, L.; Liang, S.; Tian, H.; Wang, C.; Gu, C. Mechanistic insights into surface catalytic oxidation of fluoroquinolone antibiotics on sediment mackinawite. *Water Res.* **2023**, 232, 119651.
- (360) He, J.; Miller, C. J.; Collins, R.; Wang, D. S.; Waite, T. D. Production of a surface-localized oxidant during oxygenation of mackinawite (FeS). *Environ. Sci. Technol.* **2020**, 54 (2), 1167–1176.
- (361) Chen, Y.; Miller, C. J.; Xie, J.; Waite, T. D. Challenges relating to the quantification of ferryl(IV) ion and hydroxyl radical generation rates using methyl phenyl sulfoxide (PMSO), phthalhydrazide, and benzoic acid as probe compounds in the homogeneous Fenton reaction. *Environ. Sci. Technol.* **2023**, *57* (47), 18617–18625.
- (362) Liang, C.; Yin, S. J.; Huang, P.; Yang, S. S.; Wang, Z. C.; Zheng, S. L.; Li, C. Q.; Sun, Z. M. The critical role of minerals in persulfate-based advanced oxidation process: Catalytic properties, mechanism, and prospects. *Chem. Eng. J.* **2024**, 482, 148969.
- (363) Cheng, D.; Yuan, S.; Liao, P.; Zhang, P. Oxidizing impact induced by mackinawite (FeS) nanoparticles at oxic conditions due to production of hydroxyl radicals. *Environ. Sci. Technol.* **2016**, *50* (21), 11646–11653.

- (364) Jeong, H. Y.; Han, Y.-S.; Park, S. W.; Hayes, K. F. Aerobic oxidation of mackinawite (FeS) and its environmental implication for arsenic mobilization. *Geochim. Cosmochim. Acta* **2010**, 74 (11), 3182–3198
- (365) Winnewisser, G.; Lewen, F.; Thorwirth, S.; Behnke, M.; Hahn, J.; Gauss, J.; Herbst, E. Gas-phase detection of HSOH:: Synthesis by flash vacuum pyrolysis of di-*tert*-butyl sulfoxide and rotational-torsional spectrum. *Chem. Eur. J.* **2003**, *9* (22), 5501–5510.
- (366) Rickard, D.; Hatton, B.; Murphy, D. M.; Butler, I. B.; Oldroyd, A.; Hann, A. FeS-induced radical formation and its effect on plasmid DNA. *Aquat. Geochem.* **2011**, *17* (4–5), 545–566.
- (367) Tapley, D. W.; Buettner, G. R.; Shick, J. M. Free radicals and chemiluminescence as products of the spontaneous oxidation of sulfide in seawater, and their biological implications. *Biol.Bull.* **1999**, *196* (1), 52–56.
- (368) Park, Y.; Faivre, D. Diversity of microbial metal sulfide biomineralization. *Chempluschem* **2022**, 87 (1), e202100457.
- (369) Dong, H. L. Mineral-microbe interactions: a review. *Front. Earth Sci.* **2010**, *4* (2), 127–147.
- (370) Faivre, D.; Schüler, D. Magnetotactic bacteria and magnetosomes. *Chem. Rev.* **2008**, *108* (11), 4875–4898.
- (371) Rickard, D. The microbiological formation of iron sulfides. *Stockholm Contr. Geology* **1968**, 20, 49–66.
- (372) Fortin, D.; Ferris, F. G.; Beveridge, T. J. Surface-mediated mineral development by bacteria. *Geomicrobiology: Interactions between Microbes and Minerals. Rev. Mineral.* 1997, 35, 161–180.
- (373) Gramp, J. P.; Bigham, J. M.; Jones, F. S.; Tuovinen, O. H. Formation of Fe-sulfides in cultures of sulfate-reducing bacteria. *J. Hazard. Mater.* **2010**, *175* (1), 1062–1067.
- (374) Hatton, B.; Rickard, D. Nucleic acids bind to nanoparticulate iron (II) monosulphide in aqueous solutions. *Origins Life Evol. Biospheres.* **2008**, 38 (3), 257–270.
- (375) Zheng, M.; Lu, J. G.; Zhao, D. Y. Toxicity and transcriptome sequencing (RNA-seq) analyses of adult zebrafish in response to exposure to carboxymethyl cellulose stabilized iron sulfide nanoparticles. *Sci. Rep.* 2018, *8*, 8083.
- (376) Rickard, D. Microbial sulfate reduction in sediments. Sulfidic Sediments and Sedimentary Rocks; Elsevier, 2012; pp 319–351.